

Winter 2006

Retinal tracking system design for smart flashblindness non lethal weapon

Gregory T. Wolff

University of New Hampshire, Durham

Follow this and additional works at: <https://scholars.unh.edu/thesis>

Recommended Citation

Wolff, Gregory T., "Retinal tracking system design for smart flashblindness non lethal weapon" (2006). *Master's Theses and Capstones*. 254.

<https://scholars.unh.edu/thesis/254>

This Thesis is brought to you for free and open access by the Student Scholarship at University of New Hampshire Scholars' Repository. It has been accepted for inclusion in Master's Theses and Capstones by an authorized administrator of University of New Hampshire Scholars' Repository. For more information, please contact nicole.hentz@unh.edu.

**RETINAL TRACKING SYSTEM DESIGN FOR
SMART FLASHBLINDNESS NON LETHAL WEAPON**

BY

Gregory T. Wolff

B.S., University of New Hampshire (2002)

THESIS

Submitted to the University of New Hampshire
in partial fulfillment
of the requirements for the degree of

Master of Science
in
Mechanical Engineering

December, 2006

UMI Number: 1439301

INFORMATION TO USERS

The quality of this reproduction is dependent upon the quality of the copy submitted. Broken or indistinct print, colored or poor quality illustrations and photographs, print bleed-through, substandard margins, and improper alignment can adversely affect reproduction.

In the unlikely event that the author did not send a complete manuscript and there are missing pages, these will be noted. Also, if unauthorized copyright material had to be removed, a note will indicate the deletion.

UMI[®]

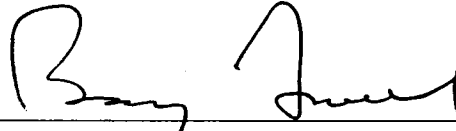
UMI Microform 1439301

Copyright 2007 by ProQuest Information and Learning Company.

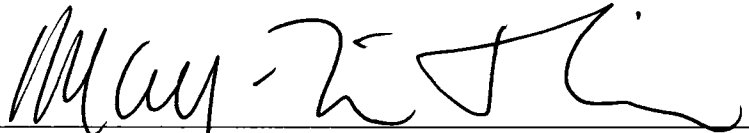
All rights reserved. This microform edition is protected against unauthorized copying under Title 17, United States Code.

ProQuest Information and Learning Company
300 North Zeeb Road
P.O. Box 1346
Ann Arbor, MI 48106-1346

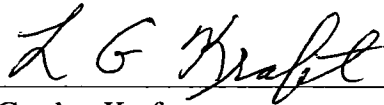
This thesis has been examined and approved.



Thesis director, Barry Fussell
Professor of Mechanical Engineering



May-Win Thein
Associate Professor of Mechanical Engineering



L. Gordon Kraft
Professor of Electrical Engineering

12/15/2006

Date

DEDICATION

To Mom and Dad.

ACKNOWLEDGMENTS

A number of people have made this paper possible. In particular I wish to thank Jeff Miller for his Saturdays and signal processing knowledge; Professor David Watt for advising and sponsoring my project; Timothy Upton for the use of his laboratory space; Professor Barry Fussell for taking on advising responsibilities at the last minute.

I would also like to acknowledge the following people for their assistance and support: Tracey Harvey, Sheldon Parent, Adam Perkins, Duane Hudgens, Eric Sampson, Katie Koval, Antonin Ancelle, Steff Kelsey, Meghan Pronovost, Jesse McGowan, Amy Shaw, and The MathWorks.

TABLE OF CONTENTS

	Page
DEDICATION	iii
ACKNOWLEDGMENTS	iv
LIST OF TABLES	vii
LIST OF FIGURES	viii
ABSTRACT	xii
CHAPTER 1: INTRODUCTION	1
CHAPTER 2: BACKGROUND	4
2.1 Anatomy of the Eye	4
2.2 Visual Cycle Reactions	7
2.3 Eye Safety	10
2.4 Ocular Fundus Spectral Reflectance	13
2.5 Flashblindness	15
CHAPTER 3: OCULAR RADIATION LIMITS	19
3.1 Ocular Hazard Assessment	19
3.2 Infrared Maximum Permissible Exposure	20
CHAPTER 4: TRACKING SYSTEM CRITERIA AND DESIGN CONCEPTS	24
4.1 Description	24
4.2 Optical System Design - Experimentation and Design Evaluation	26
4.3 Alvarez Lens Motion System	32
4.4 Glint Detection and Position Control	34
CHAPTER 5: SIGNAL DETECTION AND DISCRIMINATION	36
5.1 Detector	36
5.2 Signal Processing	38
CHAPTER 6: DSP IMPLEMENTATION	45
6.1 The Boxcar - A Filter with fewer multiplications	46
6.2 Simulation for Deployment	48

6.3 Adapting the algorithm	49
CHAPTER 7: PROTOTYPE - DESIGN AND SIMULATION	52
7.1 Tracking System	52
7.2 Model Development	54
7.3 Analog Circuitry	65
CHAPTER 8: SYSTEM RESPONSE EXPERIMENTATION	68
8.1 Experiment Design	68
8.2 Data Collection Inclusion	70
8.3 Calibration	70
8.4 Tuning the Controller	71
8.5 Controller Results	72
8.6 System Malfunction	74
CHAPTER 9: CONCLUSIONS AND RECOMMENDATIONS	75
9.1 Conclusions	75
9.2 Future Work	76
BIBLIOGRAPHY	78
APPENDICES	80
APPENDIX A: MATLAB RAY TRACE CODE	81
A.1 Lens Structure	81
A.2 Convert Lens Thickness	83
A.3 Optical Medium Interface Calculations	84
A.4 Ray Trace	86
APPENDIX B: C CODE FOR DSP	98
B.1 DSP Code	98
B.2 Lookup Table Formulation and Results	110
APPENDIX C: ANALOG CIRCUITRY	112
C.1 Signal Conditioning Schematic	112
C.2 H-Bridge Schematic	113
C.3 Eye Tracking Validation Experiment Schematic	114
APPENDIX D: ANALOG SIGNAL PROCESSING	115
D.1 Analog Signal Processing Schematic	115

LIST OF TABLES

Table Number		Page
3.1	MPE Formula Selection Criteria - Tabulates the data necessary to determine the appropriate MPE formula for each wavelength	21
3.2	MPE Calculation Results - Displays the calculation results from finding the maximum permitted exposure for each wavelength. A wavelength of 800 <i>nm</i> was chosen for the 800 to 900 <i>nm</i> wavelength range	22

LIST OF FIGURES

Figure Number	Page
2.1 Eye Anatomy - The basic anatomy of the human eye.	5
2.2 Phototransduction - The basic molecular pathways required for converting photon hits into neural signals.	8
2.3 Transmission and Absorption of Ocular Media (adapted from Sliney and Wolbarsht) - The ocular media has a high transmittance and low absorption in the visible light region. Note cornea and lens absorb a majority of the UV radiation. The cornea also absorbs most of the longer wavelength IR radiation.	13
2.4 Fundus reflectance dependence on wavelength (Adapted from Delori and Pflibsen[1])- A compilation of various data sets shown in Delori and Pflibsen of reflectance data from a variety of human subjects with different eye coloration, ethnic backgrounds, etc. In the longer wavelengths, there is roughly a 10% reflectance rate. The reflectance corridor represents the range of expected reflectance.	14
2.5 Unbleached Pigment as a Function of Flash Energy (Adapted from Rushton and Henry[2])- Two different flash lengths were used over a variety of flash energies. Note the longer 10 s flash was able to completely bleach photopigments in the energy range of 107 td s. However the 100 μs flash does not follow the same pattern. It appears to be limited to about a 60% bleach level, suggesting that the bleaching of pigment is rate limited.	16
2.6 Pigment Regeneration as a Function of Flash Duration (Adapted from Rushton and Henry[2])- A number of experiments were performed over a range of short and long bleaching exposures. Curve A is an exponential with a time constant of 120 s, while curve B illustrates a time constant of 60 s. This shows that pigment recovery for the long and short bleach durations have two distinct time constants.	18
2.7 Recovery of Vision as a Function of Flash Energy (Adapted from Miller[3])- The plot shows that the mean log recovery time increase linearly with the log flash energy. This is for a $4.0 \times 10^7 L$ flash. Recovery was tested with random letters subtending a 16.3° visual angle with a luminance of 0.07 mL.	18
3.1 Spectral Distribution of Xenon Flashlamp (adapted from Capobianco[4]) - plots the efficacy of a xenon flashlamp for a typical set of operating parameters. The efficacy is normalized relative to the peak occurring at 236 nm. Approximately 20% of the emitted energy falls in the wavelength region below 200 nm. In the infrared region, the flashlamp emits 5% to 10% of the total radiant energy (Capobianco, 2002). . .	20
4.1 Conceptual diagram of Alvarez lens pair. Linear motion of the primary lens results in deflection of a passing beam.	24

4.2	This figure illustrates the theoretical optical setup for the retina detection probe beam (1), and the blindness inducing flash (2). The return from the retina (3) is also displayed. Note the dichromatic mirror reflects the probe beam, yet allows the flash to pass with little attenuation.	25
4.3	Single optical path design. This setup was constructed in the lab for experimentation. The polarized filters are necessary to eliminate stray probe beam rays from falling onto the detector, giving a false position of the eye. Although somewhat effective, the scattering from the primary lens provides saturating levels of noise, and the polarizers reduce the beam power by approximately 50% on each pass. A modulator (beam interrupter) is used to increase the signal to noise ratio; however, the reflection from the various optical components in the system still overpowered the return from the synthetic retina.	28
4.4	The dual path system eliminates the leaking of optical noise from the outbound probe beam onto the detector. The second optical path only collects reflected light. Using signal processing to pick up the modulated beam, the SNR is greatly increased. Simulations and preliminary testing extracted signals from noise with orders of magnitude more power than the signal. The increased sensitivity produces a new challenge because even surfaces with relatively low reflectance produce a easily captured signal.	30
4.5	The hybrid path system - see figure 7.1 for more detailed equipment description.	32
4.6	Lens holder system design (isometric view)	33
5.1	Photocell arrangement on quadrant detector	36
5.2	Horizontal voltage output versus horizontal position - This figure demonstrates how the voltage changes as a laser spot is moved horizontally across the quadrant detector.	37
5.3	Vertical voltage output versus horizontal position - Note that the vertical voltage does not remain constant when the laser spot nears the center of the detector.	37
5.4	Simulink model for the simulation of glint signal extraction and detection. The component values for the lowpass filter are $R_1 = 1000 \Omega$ and $C_1 = 0.1 \mu F$	41
5.5	The Source Model consists of a 1000 Hz signal, random white noise, and 120 Hz noise.	42
5.6	Input Filter Response - shows the magnitude and phase response across the lower spectrum of the input lowpass filter used to prevent aliasing.	43
5.7	Digital Lowpass Filter Response - displays the magnitude and phase response of the digital low pass filter across the lower frequency spectrum.	43
5.8	Simulation results comparing return glint to absence of glint	44
6.1	The boxcar filter (moving average) has a narrow bandwidth. It is designed to have a null at the carrier frequency of 1000 Hz, The first null value is 125 Hz and this ultimately limits the bandwidth of this particular lowpass filter.	47
6.2	Simulation results of revised signal detection algorithm. The inputs have been normalized with respect to the first channel. The resulting normalized position is as expected, even with heavy input noise provided by the simulated inputs.	48

6.3	Actual deployment results. Channel 1 was provided an input signal with half the amplitude of channel 2. This resulted in a negative position rather than the positive experienced in the simulation results. The result was just shy of the expected -0.6, but there may have been some error in the actual amplitudes of the signals entering the channels. In this case a signal generator was used to simulate the pulsating laser beam.	49
6.4	Model used for DSP simulation and implementation.	51
6.5	Channel subsystem of model used for DSP simulation and implementation.	51
7.1	Physical Model on laser table	53
7.2	Synthetic Eye	54
7.3	Alvarez lens motion setup	54
7.4	Simulink ElectroMechanical Simulation Model - In this instance the first order polynomial estimation of return beam position is used.	55
7.5	Lens System Free Body Diagram	56
7.6	Electro-Mechanical model.	57
7.7	Optical Subsystem - primarily provides a link to the ray trace algorithm.	59
7.8	Ray Trace of System Model - Displays the results of an actual ray trace performed in the simulation model. Note that the return beam has little divergence. In this case the eye had been centered in the probe beam.	60
7.9	Ray Trace in the Eye - Displays the result of tracing the probe beam and reflection in and out of the eye. Note the return beam is slightly narrower than the input beam. This is a result of the limit calculations, which were designed to prevent beams with a divergence greater than the width of the iris from escaping.	61
7.10	Detector Subsystem - In this instance the first order polynomial estimation of return beam position is used.	62
7.11	Results of oscillating the eye within the probe beam at roughly $8 \frac{in}{s}$. Note that direction of lens movement is opposite the direction of the eye motion.	63
7.12	There is a small time lag, as expected, which means the beam tracks slightly behind the position of the eye.	63
7.13	Model Step Input Results - response time of the system is approximately 0.04 s for an angular displacement of the eye about 1°	64
7.14	Comparing Beam Displacements - the angular displacement of the probe beam as a function of the primary lens displacement was compared between measured values of the physical model and the computer simulation. The simulation approximation was determined to be acceptable.	65
8.1	Eye Tracking Experiment Basic Setup - shows the basic design used to simulate horizontal movement of the eye by changing the angular position of the output probe beam. The angular position is measured using a rotary potentiometer.	69
8.2	Angular displacement calibration	71

B.1	Inverse Lookup Table Plot - Displays the integer value and necessary bit shift for each index of the lookup table. To perform a division, a 16 bit number is multiplied by the integer inverse value, and then a right shift of the associated number of bits as described by the bit shift table is performed on the product.	111
C.1	Signal Conditioning Circuit Schematic	112
C.2	H-Bridge Schematic	113
C.3	Eye Tracking Validation Circuit Schematic	114
D.1	Analog Signal Processing Circuit Schematic	115

ABSTRACT

RETINAL TRACKING SYSTEM DESIGN FOR SMART FLASHBLINDNESS NON LETHAL WEAPON

by

Gregory T. Wolff

University of New Hampshire, December, 2006

Development of a non lethal method of providing incapacitation of human subjects is of primary importance in both law enforcement and military fields. The proposed Smart White Light Dazzler is such a device that induces flashblindness in the subject using a flash of white light. It is intended to automatically track the retina of a human subject, and then make adjustments to the power of the flash based on factors that affect the susceptibility of the eye. Temporary blindness is induced in the subject without risking permanent tissue damage.

The primary contribution of this research is the design of a single axis tracking mechanism that uses a dual Alvarez lens system to deflect an outgoing probe beam directly onto a subject's retina. The system design uses a 630nm laser, pulsed at 1000Hz, to locate and track a targeted synthetic retina. The position of the retro-reflection of the probe beam from a synthetic eye is measured with a photo-sensitive silicon quadrant detector. The detected signal is processed to produce an appropriate motion control signal using a TI C2000 microprocessor. The signal processing algorithm employs basic Fourier principles to measure amplitude of signals reflected from the eye and affords the appropriate response signals to the motors controlling the lens position.

Preliminary experimentation shows the ability of the tracking system to deflect the probe beam so that it is able to follow a synthetic eye.

CHAPTER 1

INTRODUCTION

In modern law enforcement and warfare there is a call for the use of incapacitating, non lethal force to neutralize threats without compromising personal safety. One approach for incapacitation is visual impairment of a threat without inducing permanent damage. This work explores the design of a device that uses flashblindness to provide temporary visual impairment to reduce the threat, if not neutralize it entirely.

The most common method of visual impairment used by both civilian and law enforcement is pepper spray. Commonly referred to as mace, it uses capsaicin extracted from peppers as a severe irritant. Pain, swelling, redness, and tearing are some of the more mild effects. It can also induce respiratory hinderance and vomiting. Often used, and very effective, it does have several drawbacks. Pepper spray has a short range of effective use, generally in the range of hand-to-hand combat. Depending on the type of spray (i.e. mist versus a stream) it can be indiscriminate about who is affected by the weapon.

Longer range incapacitation or deterrent generally requires firing a projectile at the threat. There are a variety of options already on the market including beanbags, ceramics, rubber bullets, and other "soft" projectiles. The primary disadvantage to this style of weapon is the dynamic effect target range has on the results. At too long a range, the weapon can be ineffective. Missing the target entirely is likely. At too short a range, the weapon can cause severe injury and perhaps be lethal. Location of the projectile impact provides for a large discrepancy in effectiveness of the weapon.

Temporary visual impairment through flashblindness provides a non-projectile solution at greater ranges than the traditional use of pepper spray. This device is designed to incapacitate subjects at ranges from approximately 10 *m* up to 100 *m*. The operator will point the device in the general direction of the subject. The weapon will then focus on the most susceptible target using a probe beam. Once the target has been located the weapon will flash directly into the subject's eye. This all happens within about 0.1 *s*.

The use of flashblindness for incapacitation or deterrence is not a new idea; however, it has

been difficult to implement. Preliminary efforts conducted by the United States Department of Justice have produced less than promising results. The primary technique involved the use of a green diode laser shown directly into the eyes of a variety of subjects at a range of distances and different ambient light settings. Green laser was chosen because the photoreceptors in the eye are most sensitive to this wavelength. The weapon was found to be effective over a limited range and ambient light settings. It required an almost direct hit to the eye, and in some cases, a duration longer than practical in most threat situations.[5]

In the design approach investigated in this study, an infrared probe beam is used to track the position of the subject's eye. A pulse of white light directed onto the retina provides the visual impairment. The energy of the pulse is variable, and based on measurements taken by the infrared probe beam including distance, energy attenuation, and ambient light. As will be discussed later in the paper, the use of a white light flash avoids many of the permanent ocular damage that lasers can induce.

The primary focus of this study is research into the requirements of such a weapon design, including eye safety requirements, hazard assessment, and flash dosage; as well as a preliminary design of the weapon's retina tracking system.

The tracking system allows precise targeting of the subject through the implementation of the Alvarez lens system. By emitting a probe beam, the retro-reflection phenomena can be used to locate the retina. Retro-reflection is illumination reflected by the retina, and focused to a less divergent beam by the lens of the eye. Retro-reflection has the highest intensity along the path back to the source of radiation. The most common occurrences include red-eye in flash photography, and seeing bright animal eyes in the headlights of your car at night.

The Alvarez lens system consists of a pair of lenses. One lens is stationary and the other motive. Physical displacement of the motive lens causes angular displacement of a beam passing through the lens system. In this case the focal points of the lenses almost coincide which results in an output beam with nearly the same divergence as the beam entering the Alvarez pair. This system is ideal for tracking retro-reflections as it takes advantage of the fact that the reflection follows the path back to the source.

The use of a laser for the pulsed infrared probe beam is a reasonable design choice. The infrared wavelengths present far less hazard to the ocular media, and have the advantage of being invisible

to the potential target of the weapon. The pulsing of the beam at a known frequency allows for distance measurements of the subject, as well as increases signal discrimination capabilities. The amplitude of most light in our environment is relatively constant (except for fluorescent lighting). Pulsing the probe beam at a known frequency, it is easier to discriminate between reflections of the probe beam and other radiation sources. For the purposes of this investigation, signal detection and discrimination are the primary focus of the signal processing development.

Chapter 2 discusses background information relevant to system design criteria. This includes eye anatomy, reactions that capture photons transforming them into neurological signals, eye safety in relation of lasers bright flashes, energy requirements for inducing temporary blindness, and reflectivity of the retina. Chapter 3 discusses the radiation limits of the human eye. Chapter 4 investigates various design constraints and considerations. The 5th chapter displays how the probe beam signal will be detected and measured. Chapter 6 develops the digital signal processing technique used to detect the signal of the reflected probe beam. Chapter 7 discusses the design of the system built for experimentation in the lab. Chapter 8 investigates the effectiveness of the system response, and the final chapter discusses the experimental results and conclusions.

CHAPTER 2

BACKGROUND

A foundation of basic information regarding the eye, its structure, and function, is necessary to understand how the non lethal weapon is designed, and how it might operate. This chapter contains information regarding the basic anatomy of the eye, and the reactions that take place within the eye that convert photons into nero signals interpreted by the brain. The anatomy section will also provide the reader with the basic anatomic vocabulary used throughout this thesis.

Lasers are a component of the design, so this chapter also discusses how lasers can affect the eye and any damage they might induce. The design depends on reflection of a probe beam from the retina, so this chapter also investigates what wavelengths of radiation provide the highest reflectance from ocular tissue.

Finally, an investigation in the available literature regarding the flashblindness phenomenon is included to formulate energy requirements and limits for the flash emitted from the non lethal device.

2.1 Anatomy of the Eye

The eye is a complex organ with the primary purpose to convert electromagnetic radiation into electrical signals that can be interpreted by the brain. Light is focused onto the retina, which has photoreceptors sensitive to a narrow frequency band of radiation (400 to 700 *nm* wavelength).

The eye is almost spherical with a diameter of approximately 25 *mm*. The *sclera* provides the support structure for the eye, where the extraocular muscles attach to move the eye about in its socket. The front of this structural layer is a transparent region called the cornea.

The *cornea* is the external surface of the eye. It acts as the first and most powerful lens, bending the incoming light towards the visual axis of the eye. It is protected by a lipid-saline layer spread across the outer surface by the eyelids.

The *iris* sits behind the cornea and acts as a diaphragm. It controls the amount of light entering the eye by dilating or constricting the pupil. The *pupil*, the aperture through which light enters the eye, can range from 2 *mm* in diameter to almost 8 *mm* in diameter. This becomes important when

determining the susceptibility of the eye to flashblindness.

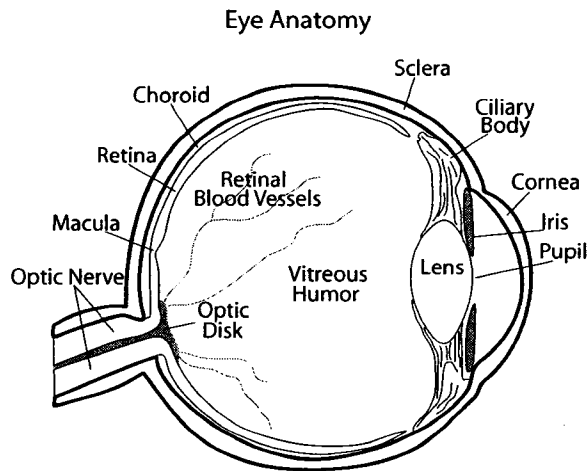


Figure 2.1: Eye Anatomy - The basic anatomy of the human eye.

The biconvex crystalline *lens* provides further focusing of the light to form an image on the retina. It is made of flexible, transparent fibers that are in a constant state of elastic tension. The shape of the crystalline lens is controlled by the ciliary body, a set of tiny muscles and ligaments attached to the lens structure. The eye automatically adjusts focus by contracting or relaxing these muscles, changing the curvature of the lens. This adjusts the focal point in a process called accommodation.

At close range the ciliary body must work much harder to keep the desired image in fo-

cus. Aging induces loss of near sight vision because the crystalline lens becomes stiffer and the ciliary muscles weaken.

The *retina* is the inner surface of the eye where the lens focuses incoming light to form an image. It contains the light sensitive cells that convert the incoming photons into neural signals, neurons connecting the photoreceptors to the optic nerve, and blood vessels carrying nutrients to the retinal cells.

Named for their shape, the photosensitive rod and cone cells contain pigments, molecules that absorb light. Four different photopigments exist in the retina, each sensitive to a different range of photon wavelengths. They are constructed from an opsin (protein) bound to the chromophore retinol. It is these photoreceptors that must be affected by the flash from the non lethal weapon to induce temporary blindness.

The *rod* cells are primarily responsible for low light or scotopic vision. They have high photon sensitivity but provide low visual acuity. Rods only contain one photopigment, so they cannot discriminate different wavelengths of light and do not allow for color vision. This is why one cannot distinguish color at low illumination levels. The rods require as few as one photon to detect incoming radiation, but their surface density in the retina is relatively low. This leads to reduced

detail of vision in scotopic conditions.

Cone cells are used in more luminous conditions, or photopic vision. They are responsible for color vision and detail. A cone contains one of three photopigments, allowing for color discrimination. Cones are less sensitive to the colliding photons, but in areas of the retina, have a very high density. Excitement of cones containing different photopigments in various combinations by different wavelengths of light allow us to distinguish a rich diversity of colors.

The *macula* is a region of the retina containing a majority of the rods and all of the cones. At the very center of the macula is the fovea, a tiny region containing only cone cells. This retinal region, centered on the visual axis, is responsible for detail vision. This is why we must scan a page with our eyes when we are reading, even though we can see the entire page.

The retinal blood vessels nourish the retinal cells, and the retinal nerve fibers converge at the optic disk, where the optic nerve bundle from the brain attaches to the eye. The optic disk contains no rods or cones and is a blind spot. The lack of visual signal from this region is compensated by the other eye, as it views the same objects with a slightly different angle.

The retinal pigment epithelium (*RPE*) is a layer of tissue that provides nourishment to the rod and cone cells in the photoreceptor layer. It also contains a range of pigments including melanin, a dark brown pigment, assumed to act as an antireflection coating on the inner surfaces of the eye. The absorption characteristics of the melanin affect the retro-reflection of the probe beam from the retina.

The *choroid* supplies nutrients to the outer layers of the retina. There is a thin membrane called Brooks membrane between the RPE and the choroid but its function is not fully understood.

The retinal cavity is filled with a gelatinous substance called the *vitreous humor*. This is a transparent fluid made primarily of water. It provides the eyes shape as well as a refracting medium. Two other humors exist on either side of the iris; the anterior and posterior aqueous humor. These contain a clear watery substance.

The *ocular fundus* refers to the collection of ocular layers illuminated inside the eye. Primarily it is used in reference to retinal, choroids, and sclera layers. It also includes the vitreous humor, but since this a transparent medium, it is only loosely included in most optical and spectral analysis of the eye.

Inter-ocular media refers to the layers of different ocular between the cornea and retina through

which light passes. [6] [7]

2.2 Visual Cycle Reactions

The photochemical processes that produce the electrical signals in both the rods and cones are very similar in nature. There are differences involving photon and wavelength sensitivity, adaptability of the photoreceptors, response time, and pigment regeneration time.

A complex series of reactions convert quantum catch by a photosensitive molecule to a biochemical electrical signal. The fundamentals of these reactions are discussed to help the reader understand how photoreceptors generate the electrical signal. It also discusses what steps are required to reform the active state of the photoreceptor so it may be capable of producing another electrical signal. Only the major steps of phototransduction, the reaction pathway in the human eye, are discussed. Further details are beyond the scope of this paper.

2.2.1 Rod Phototransduction

Photon capture leads to the hyperpolarization of the receptor cells by the closing of sodium ion channels, disrupting the flow of sodium ions across the cellular membrane.

The basic photosensitive chemical is rhodopsin (also known as visual purple). This refers to the category of photosensitive molecules that detect the presence of photons in both the rods and cones. It consists of retinol and a wavelength sensitive protein, opsin.

When rhodopsin intercepts photons, photoisomerization occurs. The rhodopsin changes shape due to energy changes in the covalent bonds of the molecular chain. The isomerized form of rhodopsin, called metarhodopsin (Rh*), is considered the active enzymatic form of the molecule, and it will maintain this unstable structure for a brief period before breaking down into its more elementary molecular components. During this period of activation, the metarhodopsin is no longer photosensitive, and additional photon hits appear to have no effect on the molecule. This is the bleached state of the photopigment.

The metarhodopsin acts as an enzyme. It binds with a G-protein called transducin causing a series of reactions that lead to an active enzymatic form of the G-protein. This cascade of reactions involves the deconstruction of the G-protein and the subsequent rejoining of a jettisoned subunit of the protein with another molecule prominent in the rod cells cytoplasm.

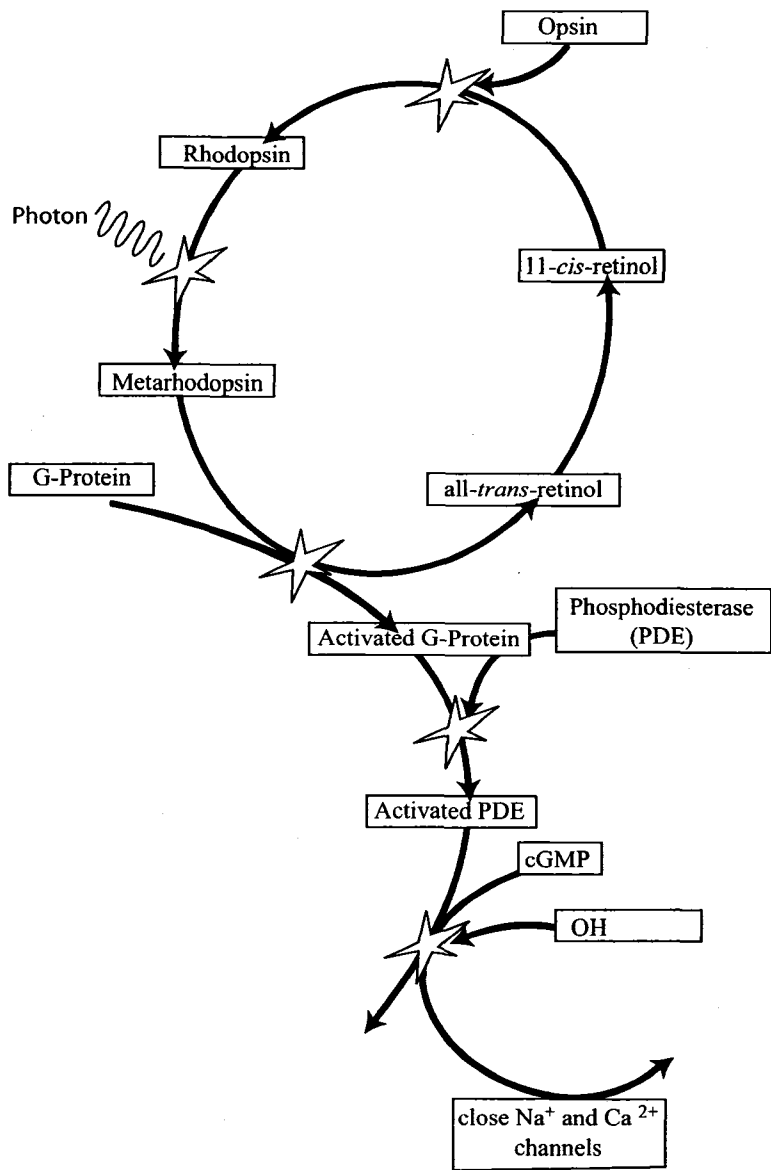


Figure 2.2: Phototransduction - The basic molecular pathways required for converting photon hits into neural signals.

The activated G-protein (G*) will bind with a third effector protein, phosphodiesterase (PDE). The activated form of PDE is a catalytic molecule that enhances the hydrolysis of a control molecule in the cytoplasm, cGMP (cG). The consequential reduction of cGMP in the cytoplasm closes sodium ion (Na⁺) and calcium ion (Ca²⁺) channels in the membranes of the photoreceptor cells. This alters the ion concentrations within the cells leading to a voltage potential and disruption of current, providing means for transmittance of an electrical signal.

Prior to quantum catch, the rhodopsin components are 11-*cis*-retinol and opsin. This is the state required for a photon capture to occur. There are four forms of opsin, each making the 11-*cis*-retinol sensitive to a different wavelengths allowing for chromatic distinction. The 11-*cis*-retinol, the ground state of the retinal, is a derivative of vitamin A. Deficiencies in vitamin A can lead to night blindness as 11-*cis*-retinol needs to be replenished periodically in the rods.

Metarhodopsin contains the isomerized form of retinal called all-*trans*-retinal. The breakdown of metarhodopsin is required to reform the ground state of rhodopsin. This involves a series of enzymatic reactions for preparation of bonding 11-*cis*-retinal to the opsin, as well as the reconstruction of 11-*cis*-retinal from all-*trans*-retinal [8]. The rate of these reactions may be controlled by the presence of Ca²⁺ in the cytoplasm of the photosensitive cell.

Once the opsin has been bonded to the 11-*cis*-retinal forming rhodopsin, the molecule is able to again convert a photon interception into an electrical signal.

2.2.2 Differences Between Rod and Cone Reactions

The basic mechanics of phototransduction are very similar between rods and cones; however, there are several differences to be addressed.

The time response for the detection of photons is approximately 4 times faster in the cones than in the rods. Rods require about 300 *ms* to process photon absorption [9]. The cone is less sensitive to incoming photons by orders of magnitude. A cone requires hundreds of photon hits per second to provide visual information while the rod only requires one photon every 100 to 200 *s* [10]. The cones also have a faster regeneration rate than the rods.

Cones are far more suitable to light adaptation. The initial method of adaptation to varying light levels is accomplished by changing the pupil diameter as much as 6 *mm*. This can be done in only a few seconds [10]. The change in the amount of retinal illumination due to pupil adjustment is lim-

ited to a factor of about 36. This will provide adaptability to illumination changes of approximately one order of magnitude. The eye however is capable of adapting to light changes of 3 to 5 orders of magnitude [11].

The highly sensitive rods provides adaptation to low light levels. Slow regeneration and high sensitivity of rod pigment lead to a constant state of bleach and inefficacy in more luminous environments. Cones possess the ability to change their apparent sensitivity to lighting conditions, while maintaining visual acuity and without attaining 100% bleach state.

Although the process for cone adaptation is not entirely understood, it is believed to lie in the cascade of enzymatic reactions that occur after the initial photochemical reaction. Experimental results indicate that probability of photon absorption is not altered by dim background illumination [11]. Control of the metarhodopsin lifetime may be a factor in adaptation.

Note that the process of chemical adaptation does occur in rods as well as cones, but to a much lesser extent.

2.3 Eye Safety

There is an inherent danger in lasers intercepting the eye. Lasers are collimated, monochromatic beams with little loss of intensity over distance. Nearly collimated beams focus to a point, creating enormous energy intensity at the focal point. The eye's inherent focus on the retina makes the retina cells highly susceptible to lasers.

The basic criterion for any radiation exposure is the Maximum Permissible Exposure (MPE). This essentially presents a safe margin in which the amount of laser light received by the eye is not damaging. There are several factors incorporated into the MPE: including wavelength, intensity, exposure duration, pulse frequency, etc.

In most cases the MPE has been normalized by the limiting aperture area. This is the maximum circular area over which irradiance and radiant exposure can be averaged.

A majority of lasers have a very low threshold of exposure due to the hazards discussed above. Each of these factors must be taken into account when evaluating the MPE for a specific case.

2.3.1 Exposure Hazards

There are three primary categories of electromagnetic radiation exposure hazards for biological tissue: photothermal damage, photomechanical damage, and photochemical damage. In this report each hazard will be discussed in relation to ocular tissue.

Photothermal Damage Photothermal damage occurs when the energy deposition rate from radiation exceeds the thermal relaxation rate of the ocular tissues. This energy buildup yields a temperature increase within the ocular tissue. The risk of temperature increase depends on a number of factors including the conduction properties of the exposed tissues, the convection properties of the local fluid circulation (blood flow, tears, etc), the size of the irradiated area (spot size), the intensity and wavelength of the radiation, and time of exposure [12].

Moderate increases in temperature (to approximately 45°C) may result in denatured proteins, loss of tertiary structure of macromolecules, and fluidization of membranes [13]. These damages may not be noticed immediately as they may be induced by residual temperature increases from short pulses of radiation or delayed cell apoptosis (cell death) due to radiation exposure.

High irradiance of ocular tissues (on the order of $1000\frac{\text{W}}{\text{cm}^2}$ for 1 s or more) can cause photoablation, the rapid vaporization of tissue that has been brought to its boiling point. This is used in surgical techniques to sever tissue while simultaneously cauterizing it [13].

Photothermal damage can occur over a wide range of wavelengths. Since water makes up to 83% of biological tissue and 90% of some ocular media, the absorption characteristics of most ocular tissue closely follow that of water [13].

Another possible hazard is thermal cataracts, also known as glass-blower's cataract. This is due to frequent exposure to high volumes of intense IRA and IRB radiation from sources such as furnaces, or perhaps some infrared lasers. However, the risk of heat induced cataracts due to lasers or similar sources is negligible compared to other risks including retinal burn [14].

Photomechanical Damage (Acoustic Effects) A brief pulse of intense radiation can produce a rapid temperature increase. The local temperature differential produces a thermal shockwave due to the rapid expansion and contraction from the heating and cooling of the tissue. These shockwaves dissipate at the speed of sound, but if the pulses are faster than the tissue can dissipate the shock-

waves, mechanical stress begins to build up. This can lead to damage through the actual tensile and compressive forces the radiated tissue may experience [13].

Currently, no non-laser source exists which can cause mechanical disruption of the tissue by ultrashort pulses [12].

Photochemical Damage Photochemical damage occurs when photons induce a reaction which changes the chemical nature of the molecules inside the ocular tissue. There are several different types of reactions, but they will not be detailed in this report. Photochemical damage happens more readily at shorter wavelengths of radiation. Blue light through ultraviolet has been found to induce ablative and oxidative processes to chemicals in the ocular media [13] [12].

One area of concern for this project is the possibility of photosensitized reactions. Some "exogenous" chemicals and pharmacological agents may act as photosensitizers, increasing the risk of ocular damage [13]. Some chemicals themselves may become toxic to the surrounding tissue from a photon induced reaction. This is of primary concern to topical agents such as eyedrops applied to the cornea. These reactions occur primarily in the ultraviolet and blue wavelengths, which have little penetration into the ocular media [12].

"Photochemical effects only dominate in wavelength regions below 600 - 700 *nm* for exposure times in excess of 10 *s*. At infrared wavelengths where photochemical effects have not been detected, thermal effects still dominate for exposure times longer than 10 *s*." [12]

Other Hazards Exposures to high power, short pulse lasers can cause rapid temperature increases. If this produces a phase change of tissue water the result is explosive vaporization [13]. Such violent reactions may cause significant damage to the ocular tissues.

2.3.2 Ocular Media Transmission Spectrum

The design of the non lethal weapon depends on the ability to reflect a probe beam from the retina, as well induce flashblindness by exposing the retina to broadband radiation. Understanding the transmittance characteristics of ocular media facilitates the selection of appropriate wavelengths for the probe beam and flash sources.

Different wavelengths have different transmittance characteristics through the ocular media. The highest percentage of transmission occurs in the visible and near infrared regions of the elec-

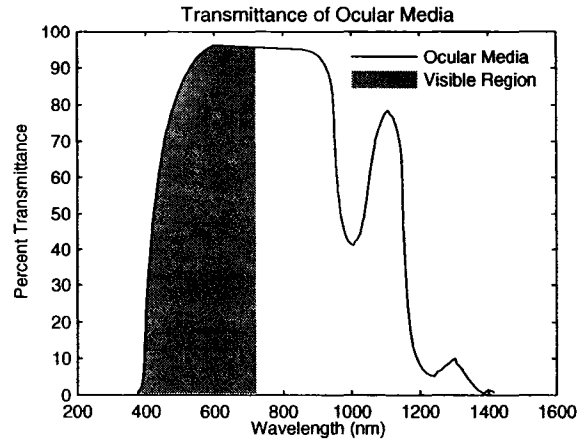


Figure 2.3: Transmission and Absorption of Ocular Media (adapted from Sliney and Wolbarsht) - The ocular media has a high transmittance and low absorption in the visible light region. Note cornea and lens absorb a majority of the UV radiation. The cornea also absorbs most of the longer wavelength IR radiation.

tromagnetic spectrum. The high absorption coefficients of water in the ultraviolet region prevent most UV radiation from penetrating more than a few millimeters into the eye [13].

The absorption spectrum of water also prevents wavelengths longer than 1400 nm from reaching the retina in any significant quantities. Thus, the retinal hazard region lies in the wavelength range of 400 to 1400 nm [15].

2.4 Ocular Fundus Spectral Reflectance

The design of the non lethal weapon depends on the ability to reflect an image of the probe beam formed on the retina back to the device. The spectral characteristics of the ocular fundus (the retina and surrounding tissues) are investigated to determine the most appropriate wavelength to use for a probe beam.

The spectral reflectance of the human eye depends on a variety of factors. The most evident include wavelength, pupil diameter, and iris color [1]. Other less obvious factors include the amount of melanin pigmentation, and probe beam image position on the retina [16].

Much of the spectral dependence results from the absorption characteristics of various ocular components. The rods and cones in the retina have an absorption spectrum that peaks in the visible

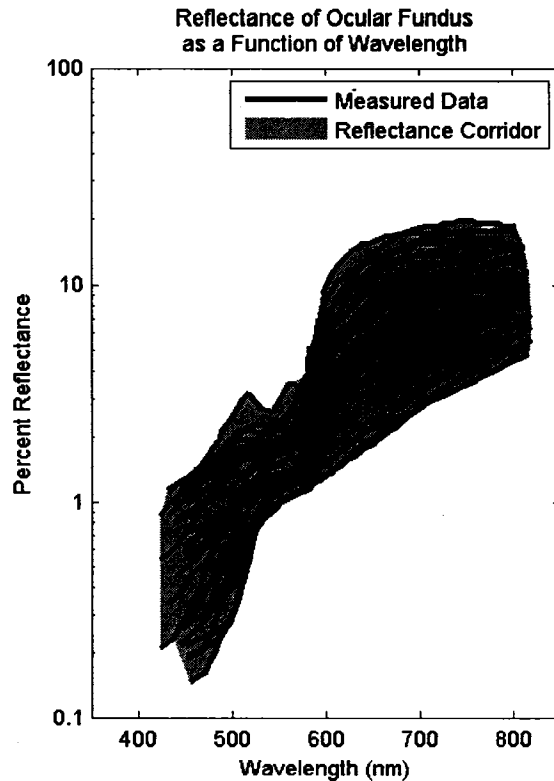


Figure 2.4: Fundus reflectance dependence on wavelength (Adapted from Delori and Pflibsen[1])- A compilation of various data sets shown in Delori and Pflibsen of reflectance data from a variety of human subjects with different eye coloration, ethnic backgrounds, etc. In the longer wavelengths, there is roughly a 10% reflectance rate. The reflectance corridor represents the range of expected reflectance.

light region. Melanin pigmentation acts as an antireflection coating on the inner surface of the eye, much as the dark coating on the inside of a camera. This pigment is highly effective in reducing the amount of light reflected from the inner ocular surfaces. Increases in the amount of melanin pigment correspond to increases in the wavelength of maximum fundus reflection [1]. The absorption characteristics of water, the primary substance in biological tissue, overwhelmingly affect the transmittance of radiation in the eye. Attenuation of reflected radiation must be minimal to ensure the maximum effectiveness of the probe beam. Therefore the selected probe beam wavelength must have high transmittance through water.

Noting above in figure 2.4 the maximum reflectance of the ocular fundus occurs in the infrared

region (wavelengths greater than 700 *nm*), with a return of radiant energy on the order of 10%. This is consistent with other studies performed on the reflectance of the ocular fundus including Van Norren and Tiemeijer's Spectral Reflectance of the Human Eye [16] and several studies compiled by Sliney and Wolbarsht [17].

Primarily, these studies have involved visible light and the very near infrared, with little data about wavelengths greater than 900 *nm*. Delori and Pflibsen however suggested a maximum reflectance at a wavelength of 1070 *nm*, and no reflectance above 1200 *nm*. This is consistent with the transmittance and absorption characteristics of the ocular media as shown in figure 2.3.

The transmittance of a 1070 *nm* wavelength through the ocular media is approximately 70%. Shorter wavelengths have lower attenuation. Wavelengths in the 800 to 900 *nm* range have transmittance through anterior ocular media on the order of 90% [17]. These also fall into the infrared region, but require more stringent threshold limitations regarding ocular exposure compared to the longer 1070 *nm* wavelength. Analysis will be performed on both sets of wavelengths to determine the appropriate probe beam wavelength.

2.5 Flashblindness

Flashblindness is a temporary condition in which a person's visual capacity is severely impaired by ocular exposure to intense visible radiation. This condition results from the bleaching of visual pigments in the photoreceptor cells of the retina. The amount of energy required to induce this condition varies greatly due to a number of factors including background luminance, photoreceptor sensitivity, and pupil diameter.

Background luminance is the primary controlling factor, for this determines receptor sensitivity and the pupil diameter. In most cases for the use of a flashblindness device the eye will be adapted to the background luminance. This means the pupil will already be adjusted to an appropriate area, controlling the amount of incoming radiation, and the chemical processes in the photoreceptors will have adapted to ambient lighting conditions.

Much of the available research on flashblindness, photopigment regeneration, and afterimages addresses the dark-adapted eye. This means the eye has been subject to low light conditions long enough to have fully dilated pupils and photoreceptor sensitivity is at its highest. People are generally not subject to this situation in daily life, and this does not represent many imagined situations

where a flashblindness device might be used. Instead people are generally exposed to high ambient light levels, where flashblindness research is much weaker.

2.5.1 Bleaching Estimation

Unfortunately, much of the results from flashblindness research and models and are controlled by the United States Department of Defense. Although the information may not be considered classified, it is considered priority information and is not public. Models do exist, but these are contained in government studies that are currently unavailable.

Further research found the energy requirements for flashblindness as a result of a nuclear detonation. An estimate of $0.1 \frac{\text{cal}}{\text{cm}^2}$ was obtained from several internet sources, but this is not considered a sound number as it cannot be verified by scientific publication. Such publications were listed, but remained unavailable to the public.

Rushton and Henry performed extensive photopigment bleaching and recovery work during the late 1960s, and are cited in many later works on the subject. Rushton and Henry developed two basic models, one for a long duration (greater than 10 s) flash where pigment regeneration becomes a factor in the current amount of bleached pigment, and a shorter duration (less than 10 s) flash model.

Interestingly enough, the same amount of light energy hitting the retina does not produce the portion of bleaching of photopigments. This can be shown in figure 2.5 from Rushton and Henry. At a 100 μs pulse the fraction of bleached photopigment begins to level out approaching a limit of almost 60%, but a longer duration flash of 10 s reaches almost 100% bleach. This illustrates the fact that flashblindness may not be controlled solely by an energy threshold, but may also be rate

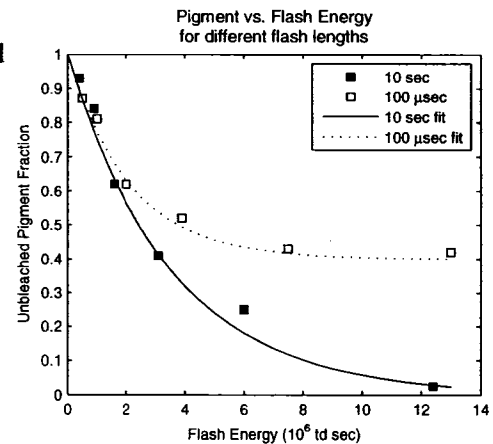


Figure 2.5: Unbleached Pigment as a Function of Flash Energy (Adapted from Rushton and Henry[2])- Two different flash lengths were used over a variety of flash energies. Note the longer 10 s flash was able to completely bleach photopigments in the energy range of 107 td s . However the 100 μs flash does not follow the same pattern. It appears to be limited to about a 60% bleach level, suggesting that the bleaching of pigment is rate limited.

limited, requiring more energy for shorter flash pulses.

This suggests that ultra-short pulses may not be able to produce 100% bleach state. However Rushton and Henry claim to use an 83 *ms* pulse to produce a 95% bleach in experimental subjects.

Another noteworthy phenomenon is the rapid pigment regeneration after a short bleach pulse when compared to that of more prolonged bleach pulses. Rushton and Henry demonstrated this fact when they determined that long bleaches (much greater than 10 *s*) require a longer pigment regeneration time to reestablish dark adapted levels (see figure 2.6). The shorter flashes had a recovery time constant of roughly half their longer counterparts.

The A and B curves of figure 2.6 are estimated curve fits, and are used more for illustrative purposes rather than bleached pigment recovery calculations. Curve A has a time constant of 120 *s* while curve B has a time constant of 60 *s*. The difference is believed to stem from the amount of free opsin available for rhodopsin regeneration within the photoreceptor cells. Longer bleaches drain the free opsin supply because pigment begins the regeneration process during these long bleaches. During the short bleach there is not enough time for pigment regeneration to become a factor, so there is plenty of free opsin available to reestablish dark adapted levels of unbleached pigments. This phenomenon was corroborated by Hollins and Alpern[18] as they investigated the dark adaptation in human cones.

Miller[3] is another often cited work that involves visual recovery after high luminance flashes. Again his experiments also involved the dark adapted eye. Miller showed the duration of visual acuity loss increased with flash energy (see figure 2.7). It is worth noting that the threshold for visual acuity was determined through viewing random letters with a viewing angle of 16.3° and luminance of 0.07 *mL*. This would suggest recovery of relatively high detail vision in low light conditions. The same flash of 4.0×10^7 *L* was used for a range of exposure durations.

Miller's findings align well with the pigment recovery data obtained by Rushton and Henry. Miller shows that after a high luminance exposure of 3×10^7 *td s*, it takes an average of 109 *s* for visual acuity to return. Rushton and Henry show that for brief flashes of similar energies about 85% of visual pigment has been regenerated.

It can be concluded that in dark-adapted conditions, a period of flashblindness can exist for about 90 to 100 *s*. This is evident by the return of visual acuity after approximately 100 *s* aligns with the about an 80 to 85% recovery of visual pigment.

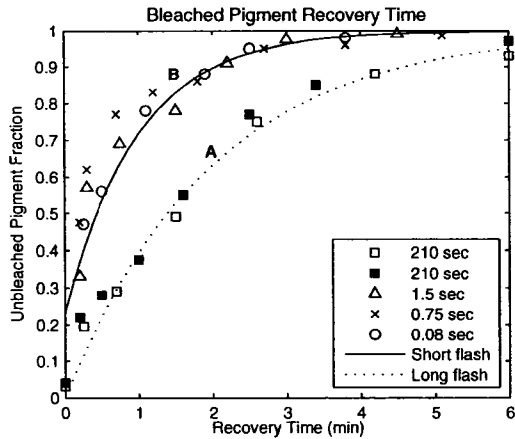


Figure 2.6: Pigment Regeneration as a Function of Flash Duration (Adapted from Rushton and Henry[2])- A number of experiments were performed over a range of short and long bleaching exposures. Curve A is an exponential with a time constant of 120 s, while curve B illustrates a time constant of 60 s. This shows that pigment recovery for the long and short bleach durations have two distinct time constants.

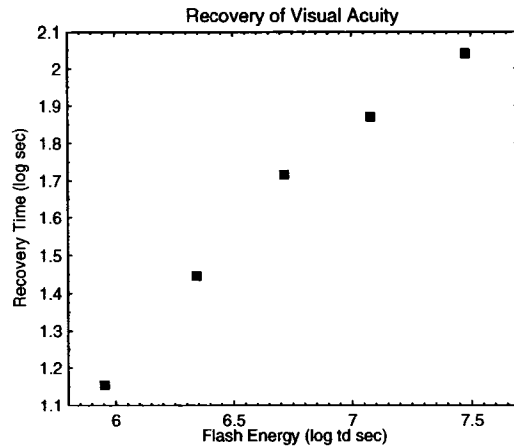


Figure 2.7: Recovery of Vision as a Function of Flash Energy (Adapted from Miller[3])- The plot shows that the mean log recovery time increase linearly with the log flash energy. This is for a $4.0 \times 10^7 L$ flash. Recovery was tested with random letters subtending a 16.3° visual angle with a luminance of $0.07 mL$.

These numbers cannot be directly applied to light-adapted conditions. As discussed previously, the chemical processes that convert photon capture into biochemical signals has the ability to adapt to higher luminance levels. This may not necessarily change the amount of energy required to induce flashblindness as the quantum catch of rods and cones does not appear to change with luminance levels. The recovery time will change with different levels of background luminance because the chemical processes adapt to decrease the visual process sensitivity and decrease pigment regeneration time.

CHAPTER 3

OCULAR RADIATION LIMITS

Bright flashes and lasers both present hazards to the eye. Based on the background research, this chapter focuses on assessment of the potential hazards of ocular radiation. Subsequent calculations are performed to determine radiation limits and steer design criteria for the flashblindness device.

3.1 Ocular Hazard Assessment

The primary concern for an infrared beam is thermal damage to the retina. The transmittance spectrum of the ocular media allow near infrared wavelengths to reach the retina with little attenuation. There is little threat of photochemical damage in the infrared spectrum because of its relatively low energy. Since the infrared source is pulsed, analysis into the appropriate pulse rates is necessary to prevent photomechanical damage. It is anticipated the required pulse rate will be significantly below the damage threshold.

The infrared probe beam is modeled as a small source. The maximum angle subtended by a dark adapted pupil is 2.7 mrad . However, if the target is only 2 m from the dazzler output, the angle subtended by the pupil drops below the small source threshold of 1.5 mrad [15]. It can be safely assumed that targeting is performed in the small source region.

The flash source has similar thermal damage concerns. Since it is a broadband source with a relatively high divergence rate, it requires much more power to be effective at longer distances. It is necessary to accurately determine the appropriate power thresholds for flashblindness to prevent any thermal damage to the retina.

Photochemical damage from the flash is also a concern. A typical xenon flashlamp emits most of its radiant energy at wavelengths in the blue through ultraviolet spectrum. This falls into the photochemical hazard region for the retina and the anterior ocular media.

The most likely flash source will be a xenon flashbulb. The spectrum from a typical bulb is shown in figure 3.1. It shows the efficacy of a xenon flashbulb as a function of wavelength for a typical set of operating parameters. The efficacy is normalized relative to the peak energy emitted at a wavelength of 236 nm . Most of the energy emitted by the flashbulb falls in ultraviolet spectrum

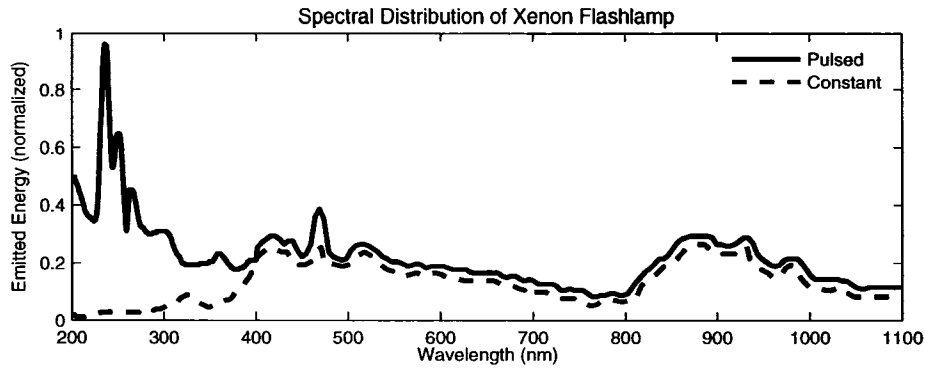


Figure 3.1: Spectral Distribution of Xenon Flashlamp (adapted from Capobianco[4]) - plots the efficacy of a xenon flashlamp for a typical set of operating parameters. The efficacy is normalized relative to the peak occurring at 236 nm. Approximately 20% of the emitted energy falls in the wavelength region below 200 nm. In the infrared region, the flashlamp emits 5% to 10% of the total radiant energy (Capobianco, 2002).

where the wavelength is less than 300 nm.

It will be necessary to ensure that emission of shorter wavelength radiation from the flash source is filtered out prior to intercepting the subject, reducing the risk of photochemical damage.

3.2 Infrared Maximum Permissible Exposure

Calculations for eye-safe levels of infrared radiation are based on the American National Standard for Safe Use of Lasers (ANSI Z136.1 - 2000 and ANSI Z136.6-2000)[15][19]. This is the most current standard for laser-human interaction.

The appropriate formulas for maximum permitted exposure (MPE) are selected from ANSI Z136.1 - 2000 based on wavelength, subtended angle, duration of exposure, and number of expected pulses. Table 3.1 below displays the necessary information for calculation of the MPE of the selected wavelengths.

The pulse rate of the laser is on the order of 1 kHz with a duty cycle of approximately 50%. If the pulse rate falls below the critical pulse frequency as put forth by the ANSI guidelines (ANSI Z136.1 - 2000, Section 8.2.3.2), then the MPE must be calculated for repetitive pulse lasers.

The infrared limitations follow the guidelines in section 8.2.3 of ANSI Z.136.1. Two wavelength

Wavelength	800 – 900 nm	1070 nm
Expected Pulse Frequency	1000 Hz	1000 Hz
Pulse Duty Cycle	50%	50%
Minimum Time between Pulses	$t_{min} = 18 \mu s$	$t_{min} = 50 \mu s$
Estimated Maximum Exposure Duration	$t_{exposure} = 10 s$	$t_{exposure} = 10 s$
MPE Equation ($\frac{J}{cm^2}$)	$MPE = 1.8 C_A t^{0.75} \times 10^{-3}$	$MPE = 9.0 C_C t^{0.75} \times 10^{-3}$
MPE ANSI Source	Table 5a	Table 5a
Standard Correction Factor	$C_A = 10^{2(\lambda - 0.700)}$ $\lambda = \text{wavelength in } \mu m$	$C_C = 1.0$
Pulse Correction Factor	$C_p = n^{-0.25}$ $n = \text{number of pulses}$	$C_p = n^{-0.25}$ $n = \text{number of pulses}$
Correction Factor ANSI Source	Table 6	Table 6

Table 3.1: MPE Formula Selection Criteria - Tabulates the data necessary to determine the appropriate MPE formula for each wavelength

categories are explored to determine which has a higher MPE.

The time between pulses exceeds the minimum time between pulses for both wavelength categories. Therefore, no pulse chains will have to be combined or averaged in order to determine the MPE for each wavelength.

Repetitive pulse lasers require the comparison of exposure rules. The first rule prevents any pulse in a pulse chain from exceeding the maximum exposure limit. The second determines if the average power incident on the eye exceeds any thermal or photochemical limitations. The third rule provides a measure to reduce the risk of photomechanical damage. The lowest result of the three rules is considered the MPE limit. The results of the calculations performed on the two chosen wavelengths are compared in table 3.2.

The 1070 nm wavelength has a much greater MPE resulting in higher maximum output wattage. In fact, even if the longer wavelength experiences greater attenuation it will still produce a more powerful retro-reflection.

Finally, an analysis of an unmodulated probe beam is performed to incorporate the possible use of a non-pulsed beam in the design. Examination of table 5a in ANSI Z136.1 shows the MPE fitting

Wavelength	800 nm	1070 nm
Time Pulse is ON	$t = 5 \times 10^{-4} s$	$t = 5 \times 10^{-4} s$
Standard Correction Factor	$C_A = 1.585$	$C_C = 1.0$
MPE/Pulse Rule 1	$0.095 \frac{J}{m^2}$	$0.301 \frac{J}{m^2}$
Number of Pulses	10000	10000
MPE/Pulse Rule 2	$0.016 \frac{J}{m^2}$	$0.051 \frac{J}{m^2}$
Pulse Correction Factor	$C_p = 0.1$	$C_p = 0.1$
MPE/Pulse Rule 3	$9.539 \times 10^{-3} \frac{J}{m^2}$	$0.030 \frac{J}{m^2}$
MPE	$9.539 \times 10^{-3} \frac{J}{m^2}$	$0.030 \frac{J}{m^2}$
Maximum Output Wattage	87 mW	275 mW

Table 3.2: MPE Calculation Results - Displays the calculation results from finding the maximum permitted exposure for each wavelength. A wavelength of 800 nm was chosen for the 800 to 900 nm wavelength range

the design criteria with an unmodulated probe beam as follows:

$$MPE = 9.0 C_c t^{0.75} \times 10^{-3} \frac{J}{cm^2} \quad (3.1)$$

$$C_c = 1.0 \quad (3.2)$$

where the correction factor is from table 6 in ANSI Z136.1. Assume that the maximum exposure time is 10 s. This produces a MPE of:

$$MPE = 50.6 \times 10^{-3} \frac{J}{cm^2} \quad (3.3)$$

In keeping with this maximum exposure time this limits the MPE to:

$$MPE = 5.0 \frac{mW}{cm^2} \quad (3.4)$$

This is the maximum wattage per area that can leave the device. The estimated output aperture effective diameter is 3 in (7.62 cm), producing a total area of 45.6 cm². This will allow for a

maximum power output of:

$$MPE = 228 \text{ mW} \quad (3.5)$$

This assumes there is zero distance between the eye and the output of the device. In most instances there will be some distance between the eye and the output of the device which, with the divergence rate of the probe beam, will cause attenuation of the probe beam and provide an additional margin of safety.

The actual power of the probe beam laser may be slightly higher as it will be attenuated by the optics of the device. The amount of attenuation is subject to the number and quality of the optics used, with the primary consideration being the transmission of infrared radiation. Note that a large laser power output would require a large power supply.

CHAPTER 4

TRACKING SYSTEM CRITERIA AND DESIGN CONCEPTS

The weapon is designed to induce flashblindness in a specific subject. In order to perform correctly, the weapon must discern the probe beam reflected from the subject's retina so it can determine the retina position. It must then track the retina by deflecting the probe beam through displacement of an Alvarez lens system.

4.1 Description

The basis for the tracking system design is the Alvarez Lens. A pair of opposing lenses in series can produce angular displacement in a passing beam through the relative movement of one of the lenses. The motive lens (Primary Lens as shown in figure 4.1) requires small translations relative to the stationary lens (Secondary Lens) to produce significant angular displacements of a beam.

Two dimensional motion of the primary lens allows for a beam to sweep through space. Changing the distances between the primary and secondary lenses provides beam focussing capability, but this is not pursued in this project.

Preliminary experiments were performed with a 1 *in* diameter primary lens with concave and plano surfaces and a 2 *in* diameter secondary lens with plano and convex surfaces. Each lens had a focal length to diameter ratio of approximately 1. A 0.25 *in* displacement of the primary lens produced an angular beam displacement of approximately 10° .

The retina of the eye is assumed to act as a scattering source. The size of the image produced on the retina is based on the distance of the eye from the source and limited by the divergence angle of the incoming beam. The scattering reflection of the beam occurs at the focal point of the crystalline lens of the eye providing a nearly collimated return. The divergence angle of the return is based on

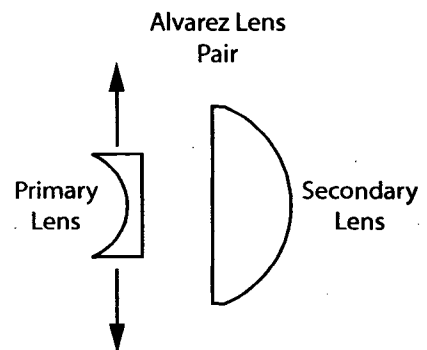


Figure 4.1: Conceptual diagram of Alvarez lens pair. Linear motion of the primary lens results in deflection of a passing beam.

the image size on the retina, the scattering of the crystalline lens, and any intermediary reflections of the probe beam from the crystalline lens, interocular media, etc.

These preliminary experiments are the basis around which the proof-of-concept design is designed and constructed.

4.1.1 Theoretical Design: The Single Optical Path System

Simplicity was the primary motivation for a system with one optical path. It requires one Alvarez lens pair to provide angular displacement of the probe beam and flash, and provides easy alignment of the optical components. The design concept is illustrated in figure 4.2.

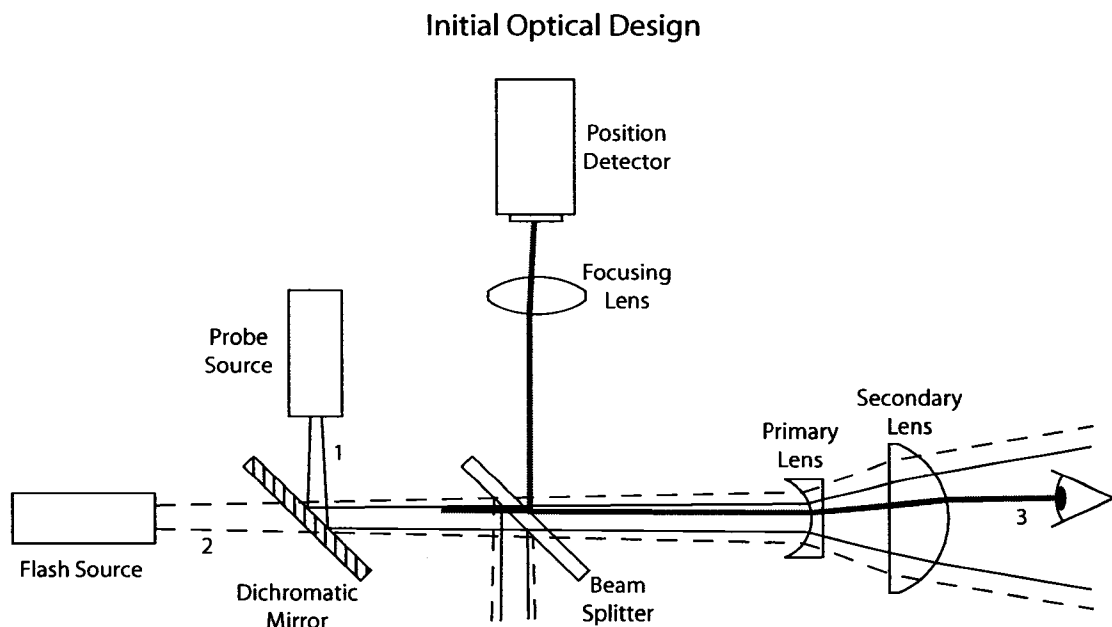


Figure 4.2: This figure illustrates the theoretical optical setup for the retina detection probe beam (1), and the blindness inducing flash (2). The return from the retina (3) is also displayed. Note the dichromatic mirror reflects the probe beam, yet allows the flash to pass with little attenuation.

The infrared probe beam reflects on the dichromatic mirror to align the beam with the system optical path. The dichromatic mirrors reflect the infrared probe beam while allowing the flash to pass through it without significant attenuation.

The probe beam then passes through the beam-splitter, through the Alvarez lens system and

then strikes a target. If the probe beam intercepts an ocular system, the beam will be focused onto the subject's retina. The retina acts as a scattering point source, reflecting the collected probe beam in all directions from the focal point of the crystalline lens. The light reflected from the retina will leave the eye mostly collimated by the eye's crystalline lens.

The collimated light re-enters the Alvarez lens system to be reflected by the beam splitter. The signal is focused by the imaging lens onto a detector. The detector is a position sensitive device that measures the position of the return glint. The Alvarez lens system is adjusted based on the target position data to center the ocular system in the probe beam. When the eye is aligned with the optical path of the system, the flash occurs. This sends a bright flash of white light along the optical path into the subject's eye.

4.2 Optical System Design - Experimentation and Design Evaluation

The theoretical design provides a basis for developing experimental models in the lab. To design the tracking system, the flash is ignored, except when considering system power losses.

A series of designs are developed to meet the real world demands of a working system model. These designs included various optical configurations such as the basic theoretical mono-optical path system, a dual optical path system, and a hybrid optical path system.

4.2.1 Experimental Eye

The experimental eye is modeled by a lens, a white paper card, and an adjustable aperture. The white card is placed at the focal point of the lens, and the aperture just before the lens. The white card acts as the retina, and the aperture as the iris. Further description can be found in figure 7.2.

4.2.2 The Mono Optical Path System

Prior to constructing a more rigorous prototype, simple experiments were performed using optical configurations similar to those found in figure 4.2 to prove the theory behind the system concept had practical application.

An experimental mock-up was built on a laser table. The initial setup mirrored the theoretical design described above, without the flash. A visible red laser is used for experimentation.

During initial simple concept experimentation, the system was successful in measuring a reflective beam. The imaging lens produces a clear image on a CCD camera of the retro-reflection from a synthetic eye when it is immersed in the probe beam. And the Alvarez lens system is able to center the eye in the probe beam by adjusting the position of the primary lens.

A more substantive model was constructed as shown in figure 4.3. Once the photocell detection of the retro-reflection signal is introduced with the quadrant detector, it becomes apparent there was significant optical noise due to laser light reflected from internal system components. These reflections have numerous sources including the lens interfaces, internal reflections of the beam splitter, ambient light, etc. The effect of the optical noise can saturate the photo-sensitive detector, preventing signal discrimination.

A set of orthogonal polarizers is included to correct this problem. The probe beam source is polarized. A return signal entering the focusing lens is polarized 90° opposed to the probe beam. The return signal is largely depolarized because it reflects on a scattering surface (the retina). This method decreases the noise enough to discern a signal on the detector. However, it also reduces the power of the retro-reflected beam.

A significant amount of optical noise still reaches the detector. Each optical interface provides for some reflection, and each reflection is slightly depolarized. It is not possible to eliminate the optical noise from the single optical path system.

There are many energy losses in this system. The beam-splitter reduces the return signal by about 50%. Each polarizer also reduces beam power by 50%. These reductions also apply to the return signal, so even a small percentage of internally reflected light from the probe beam is still orders of magnitude greater than the strength of the return from the eye.

This method of using orthogonal polarizers does provide enough noise reduction to produce a working model using a strictly bias probe beam signal. It was able to track the synthetic eye at a distance of 5 meters.

When signal modulation is introduced in the probe beam to increase the sensitivity of the detection process, the noise does not saturate the photo-sensitive cells, but did saturate the signal discrimination circuitry. The ability to detect minute signals at a specific frequency could extend the distance at which the system can track the eye. It also means that the system picks up minute traces of noise at the same signal frequency. The internal reflections of the probe beam have more

Single Optical Axis Design

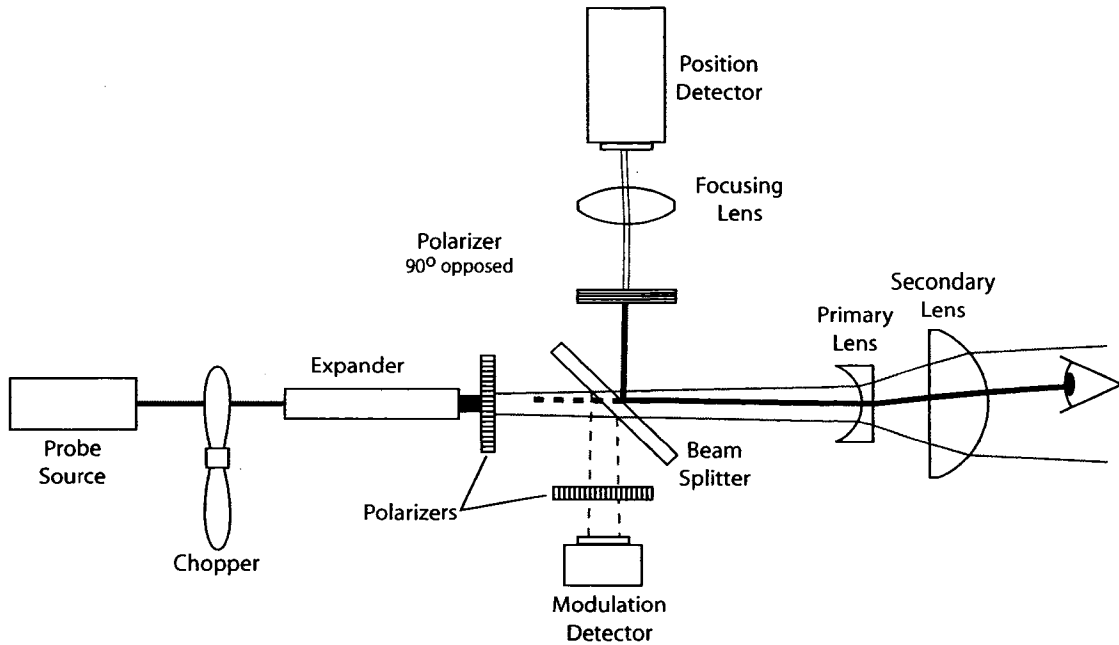


Figure 4.3: Single optical path design. This setup was constructed in the lab for experimentation. The polarized filters are necessary to eliminate stray probe beam rays from falling onto the detector, giving a false position of the eye. Although somewhat effective, the scattering from the primary lens provides saturating levels of noise, and the polarizers reduce the beam power by approximately 50% on each pass. A modulator (beam interrupter) is used to increase the signal to noise ratio; however, the reflection from the various optical components in the system still overpowered the return from the synthetic retina.

power than the return glint signal. This had not been a significant problem using a bias probe because the gains and offsets of the detector can be adjusted to detect small increases in power hitting the detector from the return glint.

The modulated signal does not allow for the same corrections. The large swing in voltage output from the detector at the frequency of the signal modulation. Now instead of looking for changes in DC voltage levels, it is necessary to find changes in amplitude of an oscillating signal. In most instances the circuitry could not discriminate between the incoming signal and the optical noise. This can not be corrected by adjusting gains and bias as done previously. The high gain required to discern the signal often saturates the operational amplifiers used in the circuitry.

The sharp curvature of the primary lens in the Alvarez lens system provided for the most probe beam reflection. Also the position of the primary lens in the Alvarez lens system relative to the probe beam affected the amount of optical noise reaching the detector. Different amounts of the beam are reflected back onto the optical path based on what fraction of the lens curvature intercepted the beam. This provides for a dynamic amount of optical noise reaching the detector. Even positioning the primary lens at greater distances from the imaging lens still provides enough optical noise to be significant. Although it did reduce the changes in optical noise reaching the detector due to changes in position of the primary lens.

No attempt is made to use optics with anti-reflection coatings. This may help increase the signal-to-noise ratio (SNR), but it is not seen as the best solution. Even if the noise is reduced by a factor of 10, it would still be orders of magnitude greater than the signal.

Enough signal was scattered about the lab to make the operator location very important. If he stands where a stray scatter of the probe beam can be reflected from his body and imaged on the detector, it can saturate the detection circuit.

4.2.3 The Dual Optical Path System

A dual optical path system isolates the transmitting and receiving paths of the system as shown in figure 4.4. This method is commonly employed in range finders, radar guns, etc. This provides for better signal isolation. The probe beam can only intercept the detector after striking an external medium. An opaque barrier between the transmitting and receiving optical path prevents internal reflection from reaching the detector. In the optical tracking system, signal strength will be greater

without the beam splitter and polarizers. The immediate disadvantage is the increase in system complexity. It is more difficult to align the optical system, and the Alvarez lens system will be increased in mass and intricacy.

The same lens pairings are used to keep the motion of the lens systems as simple as possible. The primary lenses must use synchronized motion systems to ensure that both Alvarez lens pairs are imaging the same target.

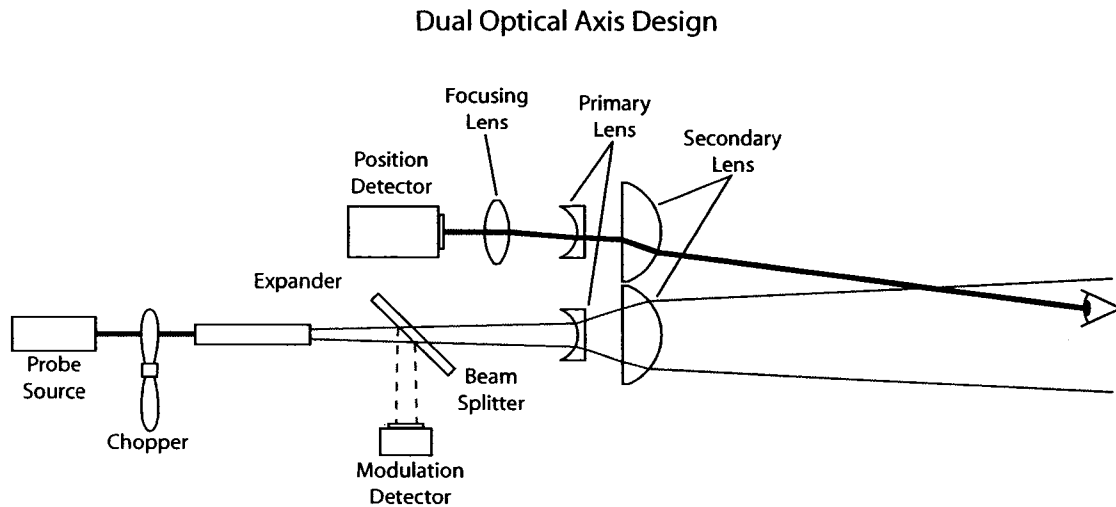


Figure 4.4: The dual path system eliminates the leaking of optical noise from the outbound probe beam onto the detector. The second optical path only collects reflected light. Using signal processing to pick up the modulated beam, the SNR is greatly increased. Simulations and preliminary testing extracted signals from noise with orders of magnitude more power than the signal. The increased sensitivity produces a new challenge because even surfaces with relatively low reflectance produce a easily captured signal.

Experiments showed a dramatic improvement in signal detection and immeasurable probe beam leakage onto the detector. A discernable signal results from the probe beam reflecting off opaque barriers within the lab (i.e. the walls of the building). All of the detected signal can be removed by blocking the secondary lens of the detector optical path. No signal leakage occurs between the probe beam optical path and the detector without first reflecting from a target.

The drastic reduction in noise and increase in signal strength greatly enhances the system sensitivity. Even weak reflectors such as black lab tables provide enough return to register as a mea-

surable signal. The synthetic eye also produces reflections that are discernable on the detector. But with the gain in sensitivity, there was no gain in target detection distance.

It was expected that the retro-reflection would produce a relatively strong signal. After all the same concept produces red-eye in photographs. The retro-reflection from the synthetic eye is visibly more powerful than from the surrounding surfaces, and is in a concentrated beam.

The divergence rate of the retro-reflection is not enough for the receiving path to capture the signal. Essentially, retro-reflection does not enter the receiving path. A majority of the reflected power remains collinear with the transmitted source beam.

The divergence rate of the return beam is proportional to the image size of the probe beam created on the retina. From the thin lens geometry, the divergence rate can be modeled as

$$\Gamma = \frac{h_i}{f} \quad (4.1)$$

where Γ is the divergence rate, h_i is the image diameter, and f is the focal length of the lens. Even with a generous image size of 1 mm and a focal length of 17 mm the divergence rate is less than 6%. So at a distance of 3 m the radius of the return beam has increased to 3 cm . Barely large enough to be captured by the parallel path lens system.

Also, a majority of the energy falls in the center of the returning beam which follows the path of the transmitting beam. This makes it difficult to register the retro-reflection on the detector compared to background reflections of the probe beam which are more divergent. This also prevents detection improvement by moving the eye farther from the source of the transmitting probe beam.

4.2.4 The Hybrid Path System

The working model design combines the best aspects of the two systems discussed previously. Its optical configuration is represented in figure 4.5. The beam splitter from the mono-path system is placed outside the Alvarez lens system so it is the first surface the retro-reflection encounters. It is also the last surface the outgoing probe beam encounters, reducing the amount of internally reflected noise reaching the detector.

The parallel second optical path is used to capture the retro-reflection from the beam-splitter. The parallel Alvarez lens system used in the detection path is necessary to correct for changes in angular displacement of the probe beam center induced by the transmittance path Alvarez lens pair.

Hybrid Optical Axis Design

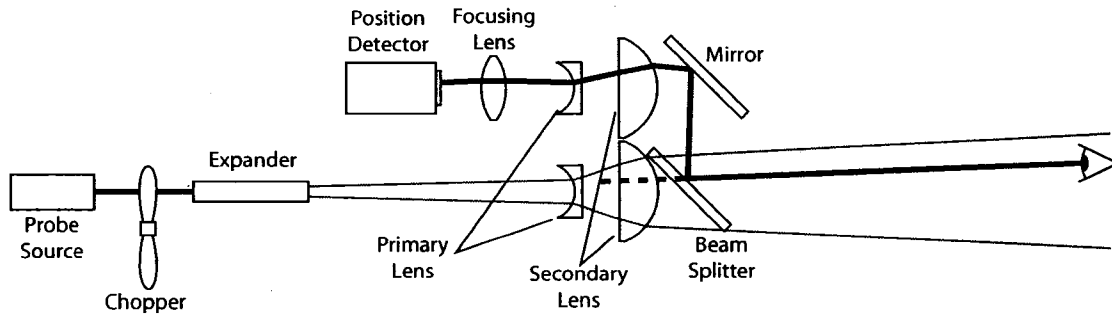


Figure 4.5: The hybrid path system - see figure 7.1 for more detailed equipment description.

Without correcting for the displacement of the probe beam center, it is impossible to determine the displacement of the retro-reflection from the eye relative to the probe beam center, using the quadrant detector.

The use of the two path system does essentially double the mass required to displace the probe beam and retro-reflections. For the purposes of design concept, however, the increase in mass is considered acceptable.

4.3 Alvarez Lens Motion System

The system to control the position of the primary lenses in the Alvarez lens pairs must be able to displace the two lenses the same amount simultaneously. It must also provide for planer motion of the lenses.

In order to maintain a rapid speed of response, the lens holding system must have minimal mass, reducing the power requirements of the drive motors.

The design represented in figure 4.6 was developed to allow the parallel motion of two lenses in the same plane.

In essence a carriage holds the two primary lenses a fixed distance apart. The carriage rides on a set of orthogonal rails that permit two degrees of freedom (DOF). The rails are moved by a friction rack and pinion system that turns the rotary motion of the motor into linear motion of the rails.

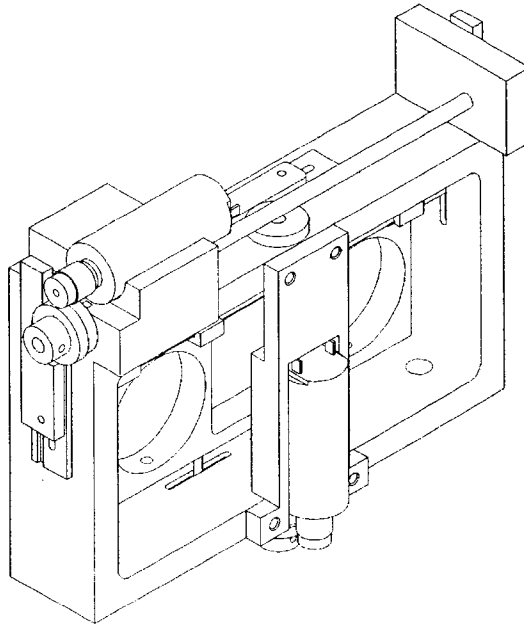


Figure 4.6: Lens holder system design (isometric view)

This concept design was not fully implemented due to time and cost constraints. Instead a similar design using a single degree of freedom (DOF) is employed as shown in figure 7.3.

4.3.1 Motor Selection

The DC motors were originally selected to provide a 0.1 *sec* system settling time for the mono-optical path design using an analog PID controller. These parameters changed over the course of the project.

The selection was based on the necessary power requirements including applied torque, inertia, available current, and voltage. The monitoring of the requirements was performed using a simulation of the expected system design.

In the mono-optical path design, the motors were expected to move far less mass. Also considerations for control of motors by pulse width modulation (PWM) were not taken into account

during motor selection as this was not yet part of the system design.

4.4 Glint Detection and Position Control

Glint detection with a modulated probe beam requires signal processing. This can be performed using either analog or digital processing techniques.

4.4.1 Analog Processing

Analog processing was the first consideration. The primary advantages are cost (as most of the necessary components are inexpensive), speed (as analog circuitry is not limited by sample rates), and simplicity.

The primary disadvantages include difficulty in producing a clean signal and the time consuming nature of debugging and constructing circuitry. Small changes in the processing algorithm can result in formidable changes to the circuitry. Finally, developing more complex control algorithms would be difficult if the PID controller was found to be insufficient.

Extensive research and experimentation was performed on this system using analog circuitry. A schematic of an example circuit can be found in appendix D1. It was found that producing a clean, consistent, and reproducible control signal is difficult. Controlling the input voltages to such components as analog multipliers so as not to saturate the outputs while still producing results with enough sensitivity to provide a useful error signal proved to be difficult. The lack of quality in some of the components may have played some role. There was also a significant noise factor, both optical and electrical, making it exceedingly difficult to produce consistent results. Optical noise can interfere with the reference signal that provides the period and duty cycle of the probe beam. Electrical noise generated by the transformers mounted in the breadboards, and other extraneous noise can be picked up through some of the longer wires, and the metal plating in the breadboard.

4.4.2 Digital Processing

Digital signal processing requires more expensive equipment. However it is easier to implement algorithm changes in both signal extraction and control. Gain correction can also be implemented for filters with far greater ease if the probe signal pulse rate is not exactly the expected frequency.

Digital signal processing may provide for a slower system response time due to the limit of sampling rate and the delay associated with digital filters.

Although the signal from the detector will be analyzed with a digital algorithm, it must first be conditioned to meet the requirements of the analog to digital converter (ADC). First, an analog lowpass filter is used to prevent aliasing of higher frequencies by the ADC. Next, gain is applied to the input voltage signal to ensure the peak to peak voltage of the input signal extends the useful input voltage range of the ADC to provide the most sensitivity. Finally, a bias is added to ensure the signal remains in only positive voltages. For more information regarding the circuit configuration, refer to appendix C1.

The output of a DSP can be a pulse width modulated (PWM) signal. This is often used in DC motor control. By changing the duty cycle of a high frequency signal to a DC motor, the average DC voltage driving the motor is adjusted.

Since the output of the PWM is generally a low power logic signal, it requires power amplification before it can be applied to the motor. A series of transistors is used to amplify voltage and current so the motor has enough power to perform.

CHAPTER 5

SIGNAL DETECTION AND DISCRIMINATION

Detecting and discriminating the retro-reflection return glint signal provides the information of the target including position and susceptibility. The extraction process is discussed, as well as the implementation of the digital signal processing.

5.1 Detector

A quadrant detector is employed to discern displacement of the spot generated by the return glint. The position of the spot on the detector is determined by the differences of voltages returned by each independent photocell. The response characteristics of the detector must be understood to properly apply the measurements to control the position of the primary lens.

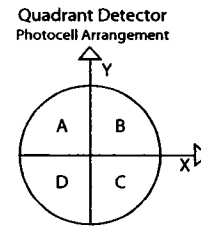


Figure 5.1: Photocell arrangement on quadrant detector

5.1.1 Description

The detector consists of four photocells in close proximity, sharing a common ground. The arrangement of the photocells is found in figure 5.1. This quadrant detector returns a voltage proportional to the intensity of light hitting each photocell.

The difference in voltage across a major axis of the quadrant detector yields the relative position of a laser spot on the active surface. This relative position is normalized by the total surface power to produce the absolute position of the spot on the detector. This prevents the apparent position of the return from dependence on target distance.

$$X = \frac{(V_A + V_D) - (V_B + V_C)}{V_A + V_B + V_C + V_D} \quad (5.1)$$

$$Y = \frac{(V_A + V_B) - (V_C + V_D)}{V_A + V_B + V_C + V_D} \quad (5.2)$$

where X is the horizontal position of the spot on the detector, and Y is the vertical position of the spot. The coordinate $(0,0)$ occurs in the center of the detector and the coordinate $(1,1)$ occurs in the center of photocell B .

Each photocell is separated by 20×10^{-3} in; enough to provide voltage independence, while maintaining close enough proximity for a laser spot to span the gap between the photocells.

5.1.2 Characterization

The detector was tested to determine the output character of voltage versus laser spot position.

Voltage output was measured with a laser spot shone on the detector. Voltage data for both horizontal and vertical position was recorded as the detector was moved horizontally a few millimeters. The experiment was repeated for two fixed vertical positions. The first, the laser intercepted the detector horizontal axis, and the second with the spot 4 mm above the horizontal axis.

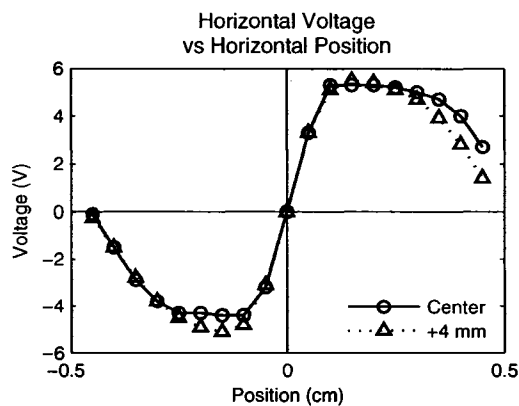


Figure 5.2: Horizontal voltage output versus horizontal position - This figure demonstrates how the voltage changes as a laser spot is moved horizontally across the quadrant detector.

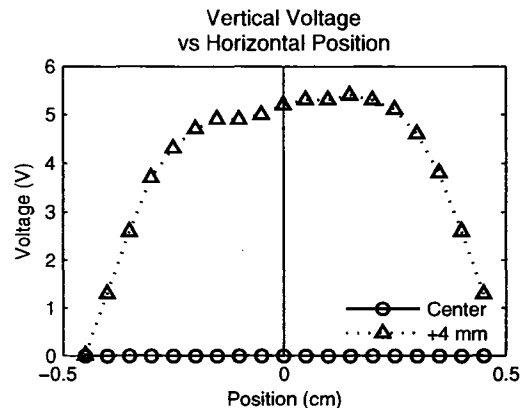


Figure 5.3: Vertical voltage output versus horizontal position - Note that the vertical voltage does not remain constant when the laser spot nears the center of the detector.

The results for the horizontal voltage as a function of horizontal position of a spot on the detector are shown in figure 5.2, are as expected. The sign of the voltage changes as the laser spot moves from one half of the detector to the other. Magnitudes of the x-position voltage remains consistent on both halves of the detector. The voltage tends toward zero at the outer edges of the detector because less of the laser spot is hitting the active surface. Also, each half of the detector

displays a maximum position voltage. The photocells are independent and discrete, so they produce a saturation position where the voltage does not change even though the position of the laser spot changes.

The results for the vertical voltage as a function of horizontal position of a spot on the detector appear in figure 5.3, and differ from expected. The voltage is expected to climb to some constant value as the laser is moved onto the detector and then remain at that constant value until the laser spot reaches the opposite edge of the detector. The vertical position voltage is then expected to tend towards zero. Instead, the vertical voltage continues to climb until the laser spot reaches the opposite edge. This is attributed to a slight rotation of the photocell detector with respect to the detector housing which occurred during manufacturing. Even though the detector has remained horizontally level, the relative position of the laser spot on the active surface changes. This could pose a problem in detecting the vertical position of a image on the detector. Further research is required to understand how significantly this error affects the position measurements made by the detector, and if those measurement errors have an impact on the overall system performance. Since the research only involves the horizontal axis, no further investigation was required for this particular project.

It was also noted during experimentation that voltage changes can be induced by changes in background illumination. Intense illumination saturates the detector output, preventing signal detection.

5.2 Signal Processing

The signals returned from the target are estimated on the order of $1 \mu W$. The original design was based on a DC signal, but this is difficult to discern from surrounding background illumination. The most common sources of radiation occur as a bias rather than a modulated signal. Modulating the probe beam and applying signal processing techniques to detect signals at the modulation frequency increases the likelihood that the detected signal is a reflection of the transmitted probe beam and not from background radiation. This allows minute return signals from the retina to be detected. The signal processing extracts the amplitude of the signal intercepting the detector. This value, in turn, is used to determine the position of the spot on the detector.

5.2.1 Processing Theory

There are two primary methods employed in the signal processing of the input signals from each quadrant on the detector: mixing (frequency shifting) and filtering.

Multiplying the input signal with a sinusoid of the desired modulation frequency (also known as mixing) base-bands the input signal resulting in a DC component proportional to the signal amplitude.

Application of a lowpass filter preserves the DC while attenuating high frequency noise. Squaring the result yields the signal power at the particular modulation frequency.

A signal from a quadrant detector channel $x(t)$ is represented by the sum of sinusoids with varying amplitudes and frequencies. Since it is a sum of frequencies, mixing is distributed among each signal component. Let the input signal be:

$$x(\omega, t) = A \cos(\omega t + \phi) \quad (5.3)$$

where A is the signal amplitude, ω is any frequency in the signal domain, t is time, and ϕ is some phase shift.

Applying trigonometric identities, this can be rewritten as:

$$x(\omega, t) = A \cos(\phi) \cos(\omega t) - A \sin(\phi) \sin(\omega t) \quad (5.4)$$

Assuming that the magnitude and phase of the signal change slowly relative to the frequency signal oscillation, we can assume they are constant. Collapsing the magnitude and phase portion of the signal into new coefficient variables I and Q , reforms the equation as:

$$x(\omega, t) = I \cos(\omega t) + Q \sin(\omega t) \quad (5.5)$$

To get the maximum information about the signal, it is mixed with the complex signal with the desired carrier frequency.

$$Mixed = e^{i \omega_c t} \times x(\omega, t) \quad (5.6)$$

where ω_c is the desired carrier frequency. Euler's formula is used to break the mixing reference signal into real and complex components.

$$e^{i \omega_c t} = \cos(\omega_c t) + i \sin(\omega_c t) \quad (5.7)$$

The real and imaginary portions are calculated separately.

To calculate the contribution of the real part, the signal is multiplied by the cosine of the desired carrier frequency.

$$\begin{aligned} Mixed_{Real} &= \cos(\omega_c t) (I \cos(\omega t) + Q \sin(\omega t)) \\ &= \frac{I}{2} (\cos(\omega_\Delta t) + \cos(\omega_\Sigma t)) + \frac{Q}{2} (\sin(\omega_\Delta t) + \sin(\omega_\Sigma t)) \end{aligned} \quad (5.8)$$

where:

$$\omega_\Delta = \omega - \omega_c \text{ and } \omega_\Sigma = \omega + \omega_c \quad (5.9)$$

Assume the result of $Mixed_{Real}$ is passed through an ideal lowpass filter such that the signal amplitude at ω_Σ is 0.

$$Filtered_{Real} = \frac{I}{2} \cos(\omega_\Delta t) + \frac{Q}{2} \sin(\omega_\Delta t) \quad (5.10)$$

The same method is applied to imaginary portion of the carrier frequency. This time the signal is multiplied by $\sin(\omega_c t)$, and eventually results in:

$$Filtered_{Imag} = -\frac{I}{2} \sin(\omega_\Delta t) + \frac{Q}{2} \cos(\omega_\Delta t) \quad (5.11)$$

To obtain the magnitude squared of the signal at the given carrier frequency, sum the squares of the real and imaginary parts of the mixed signals:

$$Mag^2 = Filtered_{Real}^2 + Filtered_{Imag}^2 \quad (5.12)$$

exploiting trigonometric identities results in:

$$Mag^2 = \frac{I^2 + Q^2}{4} = \left(\frac{A}{2}\right)^2 \quad (5.13)$$

Knowing the amplitude squared from each channel of the quadrant detector will provide ample position information of the return signal on the detector.

5.2.2 Simulation

A model of the signal processor is constructed in Simulink [®], and is tested for both reflected glint signal returns, and the absence of the return glint.

Digital Signal Extraction

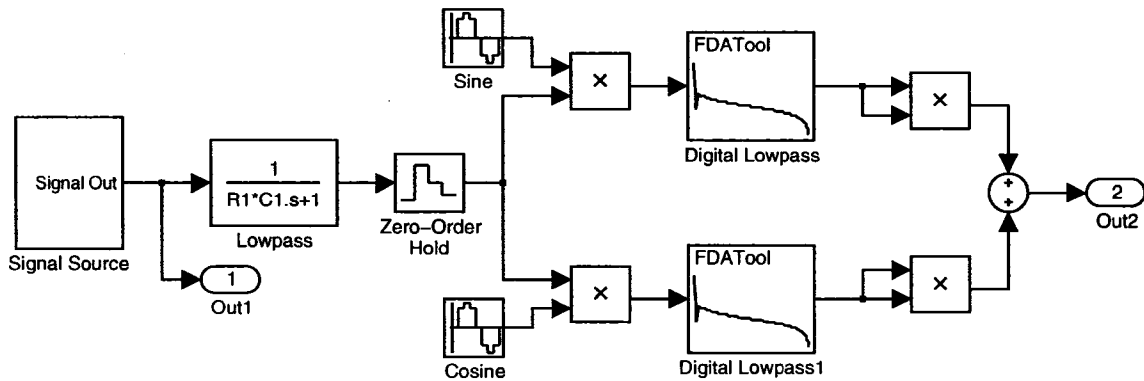


Figure 5.4: Simulink model for the simulation of glint signal extraction and detection. The component values for the lowpass filter are $R_1 = 1000 \Omega$ and $C_1 = 0.1 \mu F$.

Model Description The model in figure 5.4 consists of several major components. The first is the signal generator, which is modeled as a 1000 Hz sinusoid with added noise. The noise components include 120 Hz modeling florescent lighting, and random white noise (see figure 5.5). A sinusoid is used even though the laser is chopped into discrete pulses because the capacitance of the detector rounds the edges of the square pulses. The amplitudes of the signal and noise are close to the same order, keeping a low signal to noise ratio. The 120 Hz noise exceeds the signal amplitude, and the random noise magnitude maximizes at 120% of the signal amplitude.

The first order transfer function represents a lowpass filter necessary to prevent signal aliasing prior to the signal processing. The cutoff frequency is 1600 Hz, just above the carrier frequency (see figure 5.6). The values of R_1 and C_1 represent the resistor and capacitor values used in an active lowpass filter.

$$R_1 = 1000 \Omega$$

$$C_1 = 0.1 \mu F$$
(5.14)

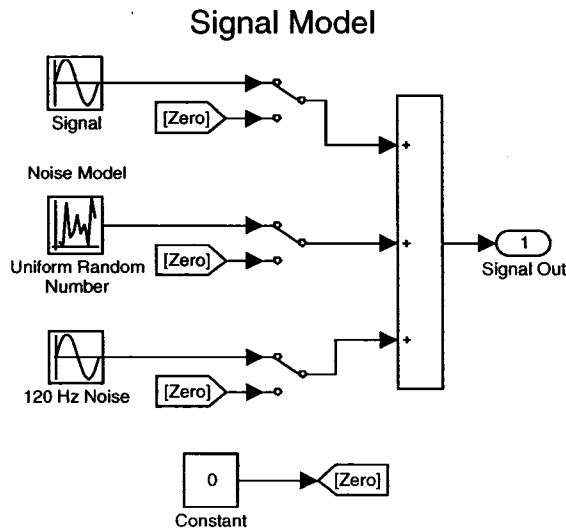


Figure 5.5: The Source Model consists of a 1000 Hz signal, random white noise, and 120 Hz noise.

The sinusoid waves are generated with two simulated sinusoid signal generators, 90 deg out of phase. Each reference sinusoid is mixed with the signal using a multiplication block. The two independent branches are then filtered to extract the carrier frequency attributes.

The zero order hold models the analog to digital conversion (ADC) of the signal with a sample rate of 10 kHz. This is 5 times the Nyquist frequency for the 1000 Hz modulated signal.

The digital lowpass filter extracts the DC component of the recentered signal.

It is a 7th order Chebyshev with a passband of 0 to 30 Hz, a 50 dB attenuation of the stopband of 35 Hz and greater. The filter was designed using MATLAB® FDA Tool for a sampling frequency of 10 kHz. The filter was designed to most closely match the passband.

Note from the filter frequency response in figure 5.7, that it fits the desired attributes well. There is an associated phase shift, but since phase is not measured, this element is not considered. The output from the filter has a ripple, but limited to $\frac{1}{2}$ dB in amplitude. This causes an overshoot of the output amplitude before settling.

Several data ports were included to collect signal data at various stages of the process. Results comparing the raw signal to the extracted signal strength are found in figure 5.8.

Testing and Results The model was tested for various noise and signal strengths. The primary test series compared the results of a returned signal with that of an omitted signal. The frequency spectrum of test results for both the raw and processed signals were compared to determine effectiveness of signal extraction (see figure 5.8).

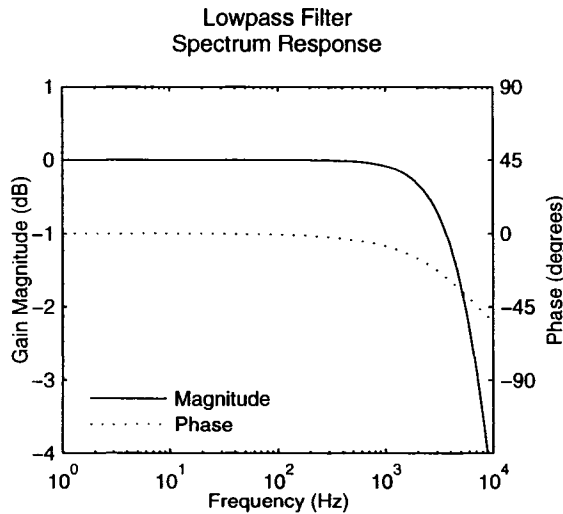


Figure 5.6: Input Filter Response - shows the magnitude and phase response across the lower spectrum of the input lowpass filter used to prevent aliasing.

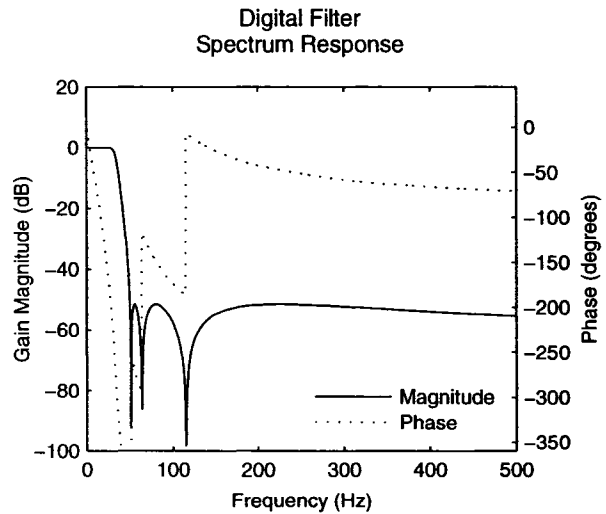


Figure 5.7: Digital Lowpass Filter Response - displays the magnitude and phase response of the digital low pass filter across the lower frequency spectrum.

A fixed step solver with a $10 \mu\text{s}$ time step, and a 5^{th} order integration scheme, or solver, is used to approximate the system response. Simulation results depend heavily on the order of the solver used during simulation. Solvers with order 3 or lower induce significant errors in the simulation output.

With the absence of the return glint, the signal processing produces the expected result of a value very close to 0. In the result with the return glint, the final value of the signal process algorithm is slightly under the expected amplitude of 0.25. This is because the anti-aliasing filter is providing some attenuation, even though the filter frequency response suggests there is zero gain at this frequency.

The ripples in the settled value of the processed return glint are due to loose filter constraints. A filter that provides less ripple in the passband, and a sharper transition region will provide a smoother result. However, tighter constraints generally require more filter taps, leading to a filter that is slower to process, both due to sample delay, and multiplication time.

With a returning signal, the rise time and overshoot are results of the digital lowpass filter. There is a sharp trade off between system speed of response and signal noise. Decreasing the response time results in higher spectrum noise polluting the output. The cutoff frequency must be

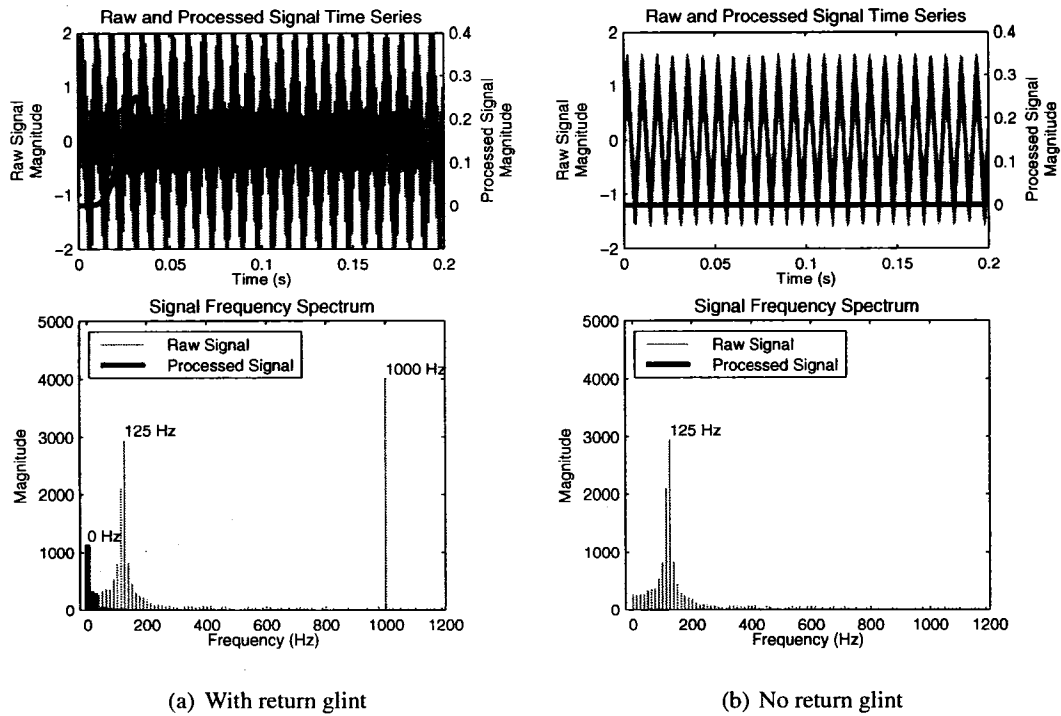


Figure 5.8: Simulation results comparing return glint to absence of glint

less than half the carrier frequency to ensure low frequency noise elimination. This is because every frequency in the signal domain was shifted by the carrier frequency in the mixer.

From the frequency spectrum the most dominant components of the raw signal are the 1000 Hz carrier and 120 Hz noise. After processing the signal, the primary spectral component is the DC. The remaining noise is virtually eliminated from the output. Also, without the return glint, there is no significant DC component in the signal processing output spectrum.

In figure 5.8, the 120 Hz noise appears in the 125 Hz frequency bin. This is due to the limitations of discrete Fourier transforms and computer approximations of discrete signals.

CHAPTER 6

DSP IMPLEMENTATION

Digital signal processing (DSP) is performed on a eZdsp™TMS320F2812 developer board with a TI C2000 processor. This board was chosen because:

1. It is designed for DC motor control. It has 12-bit analog to digital converter (ADC) input which can be connected to a conditioned output of the detector. The output is a 16-bit pulse width modulator (PWM) which changes the duty cycle of a square pulse signal to control the average voltage applied to a DC motor.

2. This board is supported by Simulink®Code Generation, which provides a means for model based design. A block diagram model of the algorithm can be constructed and simulated in Simulink®. From this model, code is generated, compiled, and ported directly onto the DSP.

The Simulink®Code Generation was employed to convert the traditional tone detection method described above in chapter 5 into C code, which is compiled by Code Composer Studio into assembly code for the TI C2000 microcontroller.

The algorithm described above overflows the processor during calculation. It requires multiplication of 20 coefficients for each digital filter. Each coefficient required 4 multiplies and a couple of adds to maintain 32-bit precision and provide the desired filter shape. So each filter required 80 multiplies. A total of 4 of these digital filters were necessary to meet the needs of two input channels.

Although the chip was able to sustain one channel, it was unable to maintain computational integrity with data input at 10 *kHz* for multiple channels.

Filters with fewer coefficients would reduce the number of multiplications, but may provide poor performance in both the pass and stop bands. Careful filter selection and possible amplitude correction may provide a means to use filters that require much less processor power. For this project, rudimentary yet very effective boxcar filters were applied. By adjusting the sampling frequency to 8000 *Hz* and using these square window filters with number of filter taps equal to an integer power of 2, all equally weighted, the processing algorithm is able to efficiently extract the signal amplitude for 4 channels efficiently without chip saturation.

6.1 The Boxcar - A Filter with fewer multiplications

The boxcar filter (or moving average) requires one multiplication; the current sample by the inverse of the number of filter taps. The difference between this product and the last sample in the filter buffer is added to a running sum.

Exploiting a power of two, the multiplication can be eliminated entirely and replaced with a right bit shift. For a 32 tap filter, instead of multiplying the current sample by 1/32 (0.03125), it can just be shifted right by 5 bits.

When filtering signals with a non-zero DC value, it is important to maintain precision prior to performing the right shift. Rounding to the nearest integer prevents accumulation of bit errors.

Rounding is accomplished by looking at the most significant bit dropped by the right bit shift. This is the last bit removed. If this bit is one, then add one to the result of the bit shift, otherwise, just perform the truncation. Without this rounding a bit error can accumulate in the filter running sum.

To get the most significant truncated bit, test the last bit truncated by performing a bit masking to determine if that bit is a 1 or a 0. For example, truncating the last 5 bits, check the 5th bit by performing:

```
(value_to_truncate & 16)
```

where 16 is 2^4 , or ...0001000. This performs a bitwise *and* operation for each bit of the original value to be truncated, and the 5th bit. If the result is non-zero, then add 1 to the truncated value. This can be seen in the calculation the *CurrentAverage* in the example that follows.

A circular buffer is needed to store the values passing through a digital filter. The power of two and bit masking can also be employed to create an efficient circular buffer. If the buffer length is 2^N , and the counter is bit masked with $2^N - 1$ when the buffer position counter reaches the end of the buffer, it is set back to 0.

Boxcar Algorithm for 32 tap filter:

```
OldValue = BufferArray[index];  
Value_Difference = CurrentValue - OldValue;  
CurrentAverage = CurrentAverage + (Value_Difference) +
```

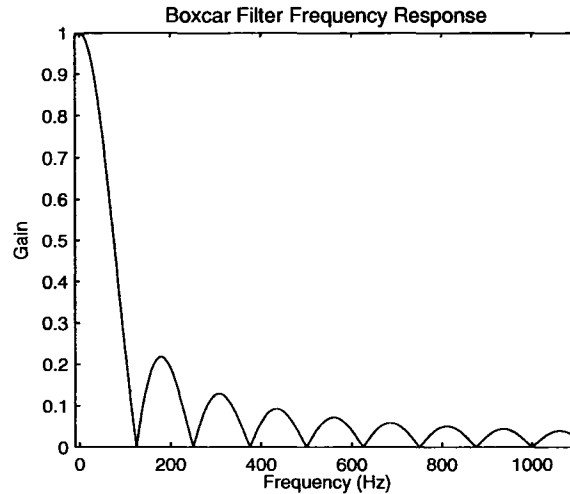


Figure 6.1: The boxcar filter (moving average) has a narrow bandwidth. It is designed to have a null at the carrier frequency of 1000 Hz. The first null value is 125 Hz and this ultimately limits the bandwidth of this particular lowpass filter.

```

((Value_Difference & 16) != 0);
BufferArray[index] = NewValue;
index++;
index = index & 31;

```

The number of cycle counts required for this filter per data sample is only 6, as opposed to the 80 multiplies per filter, with each multiply requiring several cycle counts.

6.1.1 Boxcar Frequency Response

The boxcar filter has a narrow bandwidth and loose frequency response when compared to the Equiripple filters designed originally. For an 8 kHz sample rate, the 64 tap boxcar filter response can be found in figure 6.1.

The filter has a bandwidth of 125 Hz. It also has the elegant feature of a null occurring at 1000 Hz where the signal DC will fall once it is mixed with the carrier frequency.

Other high frequency noise that may pass through this filter with little attenuation will be subject to another lowpass filter with a narrower bandwidth later in the algorithm.

6.2 Simulation for Deployment

This modified version of the signal extraction was modeled and simulated and then directly deployed onto the TI C2000 DSP.

6.2.1 Revised Model

The entire algorithm has been modeled in Simulink. Figure 6.4 displays the algorithm deployed to the TI C2000 chip. The magnitude extraction is contained in the subsystem found in figure 6.5. A slightly different version of this model was used for deployment to utilize the operation libraries for the TI C2000 chip for multiplication.

6.2.2 Simulation Results

The revised model to be deployed was first simulated to test its effectiveness. The results can be found in figure 6.2. The input signals were normalized in relation to channel 1 to illustrate that the result of the normalized position was as expected.

This model was converted to C-code using the Real Time Workshop®(the Simulink®compiler) and deployed on the TI C2000 using TI Code Composer Studio.

Modifications to the code were made manually to improve code efficiency on deployment target.

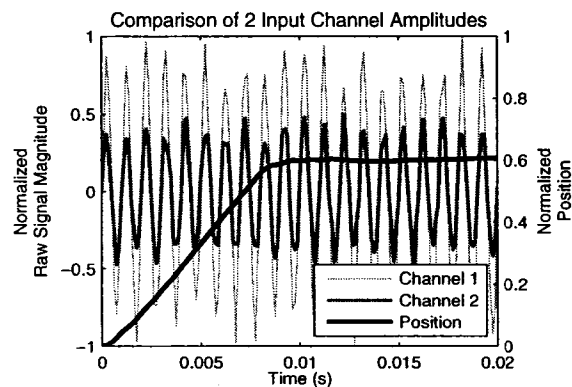


Figure 6.2: Simulation results of revised signal detection algorithm. The inputs have been normalized with respect to the first channel. The resulting normalized position is as expected, even with heavy input noise provided by the simulated inputs.

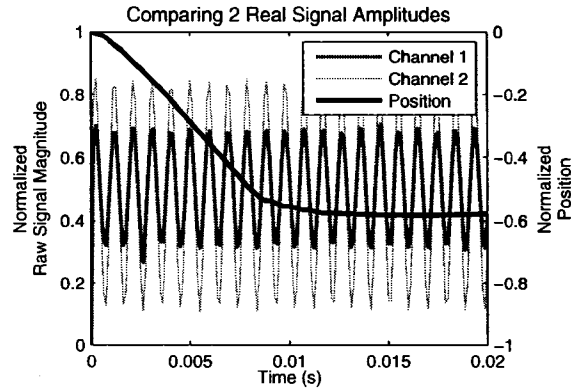


Figure 6.3: Actual deployment results. Channel 1 was provided an input signal with half the amplitude of channel 2. This resulted in a negative position rather than the positive experienced in the simulation results. The result was just shy of the expected -0.6, but there may have been some error in the actual amplitudes of the signals entering the channels. In this case a signal generator was used to simulate the pulsating laser beam.

6.3 Adapting the algorithm

The division to normalize the position was performed using a pair of lookup tables. Division on this particular chip set could take 54 clock cycles or more. While lookup tables took only two to perform the look-ups and a few clock cycles for the multiplication of the numerator and the inverse of the denominator.

The lookup tables have a 12-bit input and a 16-bit precision output. The 12-bit input is used to save memory space on the DSP board. The 16-bit output helps maintain precision, and simplifies the results of multiplying two 16-bit numbers rather than 12-bit numbers.

To help maintain the precision of division, the entire range of positive 16-bit numbers were used for each possible set of significant bits in the input value. The output of this lookup table is multiplied by the numerator of the division, and then corrected by the necessary bit shift. The number of bits shifted is stored in the second lookup table.

The 12-bit lookup table only has about 1% error over the inverse of the numbers between 0 and 32767, even though the 4 least significant bits are dropped prior to indexing into the lookup table.

Extensive testing was performed to ensure robustness of the algorithm. Each operation and algorithm step was logged to a data file and analyzed to ensure the accuracy of the results.

There may be some frequency fluctuation of the probe signal, as the actual beam chopper may not pulse the beam at exactly 1000 Hz. This may provide for some attenuation of the input signal due to the boxcar filter frequency response. Gain correction was considered and tested for actual amplitude measurement. However, since a ratio of amplitudes is taken at the exact same frequency, the gain correction was omitted in this particular implementation.

Actual test results are displayed in figure 6.3 which displays the calculated normalized position of a spot on the detector. In this instance the spot was simulated by a sinusoidal signal generator with different gain values applied to two input channels of the DSP. The resulting position value approached the expected value of -0.6, suggesting the algorithm is working correctly.

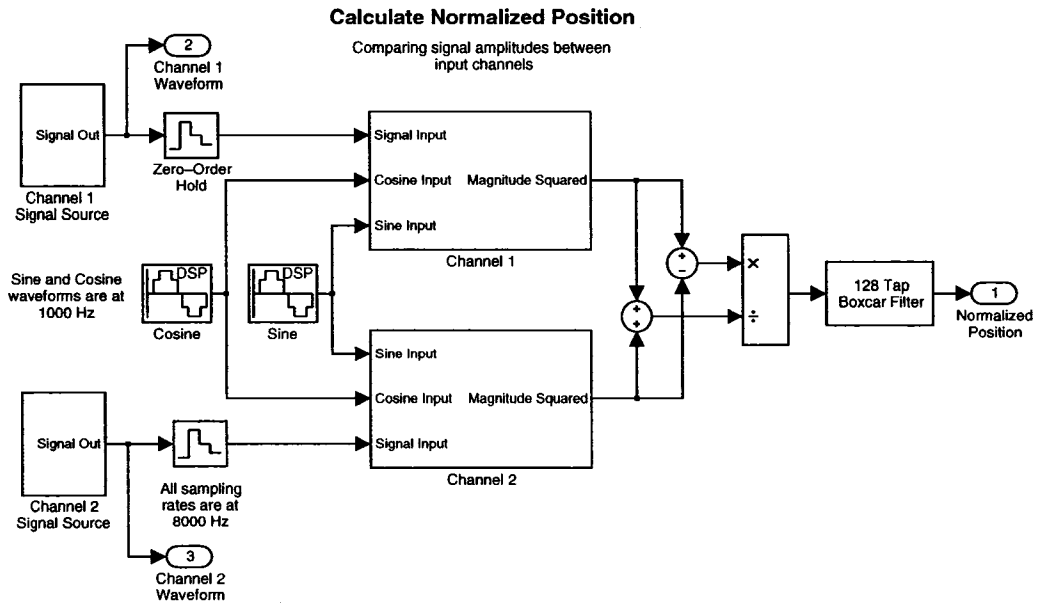


Figure 6.4: Model used for DSP simulation and implementation.

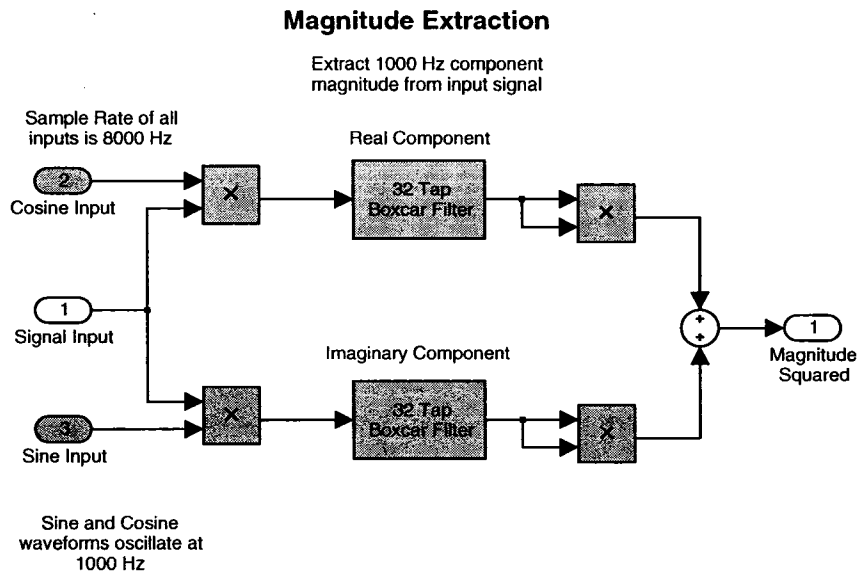


Figure 6.5: Channel subsystem of model used for DSP simulation and implementation.

CHAPTER 7

PROTOTYPE - DESIGN AND SIMULATION

The final design of the retina tracking system employs the hybrid optical path method described in chapter 4 to determine the position of the eye in the probe beam. A motion system must be designed to translate both of the primary lenses quickly in a plane. The system must also be modeled to help with controller design and implementation, as well as provide a basis for future research.

7.1 Tracking System

The tracking system was constructed and tested on a 4×10 ft auto-leveling table. A diagram of the setup can be found in figure 7.1. The infrared source was simulated using a 40 mW 630 nm wavelength Helium-Neon laser. The beam was cleaned and expanded using a beam expander. Prior to the beam expander, the beam was chopped into discrete pulses using a 12 V DC fan, that provided a pulse rate of 996Hz.

The primary lenses are 25 mm, 1.1 F, concave-plano lenses made of SF11 with a refractive index of 1.785. Each primary lens has a mass of roughly 21 gm.

The secondary lenses are 48 mm, 1.1 F, plano-convex lenses also made of SF11, with the same refractive index. None of these lenses have any added anti-reflection coatings. They are highly transparent to light in the visible region.

The beam splitter is a 50.8 mm diameter, 2 mm thick element with an estimated transmittance of 46% at 630 nm wavelength.

The mirror for the second axis reflection is a 75×38 mm rear silvered mirror.

The focusing lens is a 38 mm diameter, 3 F, biconvex lens made of SK11, with refractive index of 1.5748.

A polarizer was applied to the non-optical axis path to prevent scattered reflections from the stray beam from interfering with the signal detection on the detector. The detector used is described in chapter 5.

The synthetic eye consists of an iris with an adjustable diameter of 7 to 0.5 mm. Just behind the iris is a 12.5 mm, 2 F, biconvex lens. In the focal plane of the lens is a white styrofoam, paper-

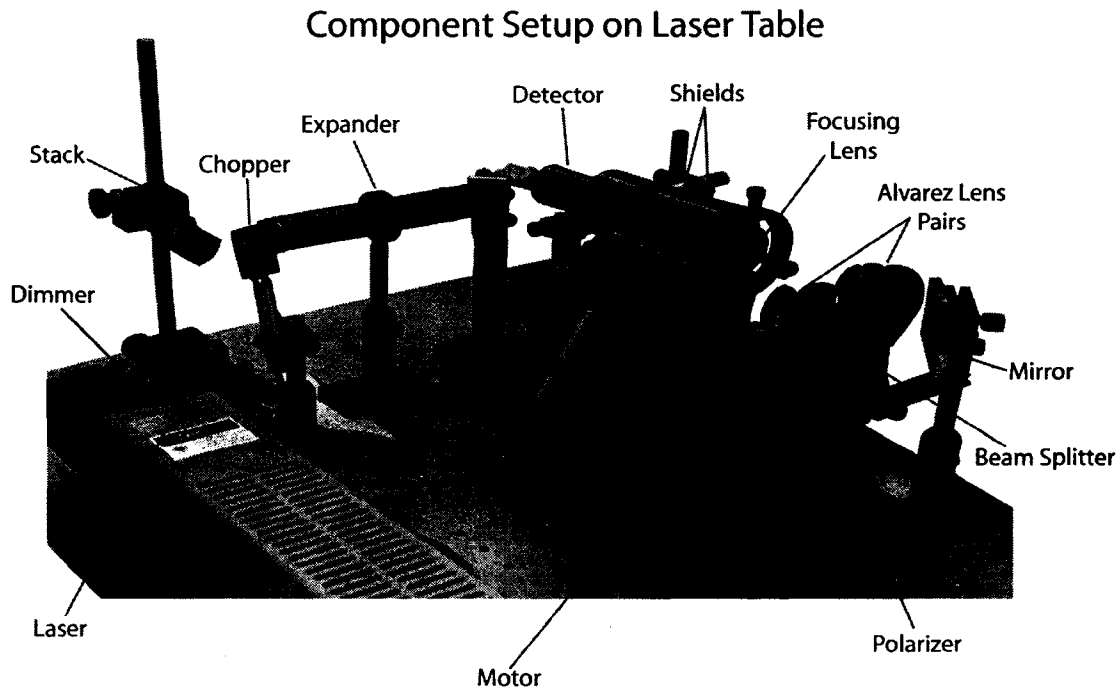


Figure 7.1: Physical Model on laser table

coated board with a flat finish. The excess white board was darkened with a black marker to prevent significant extraneous reflections of the probe beam without passing through the optical system of the synthetic eye. A labeled picture of this configuration is found in figure 7.2.

7.1.1 Primary Lens Motion System

The motion system implemented in the actual model is significantly less complex than the one described in the tracking system design considerations. Due to a combination of time constraints and malfunction of one of the quadrant detector elements, the motion system was restricted to one axis of motion, in the horizontal direction. Preliminary experimentation performed during the proof-of-concept phase showed that one axis of motion translates well to two axes of motion. A picture of the motion system is in figure 7.3.

The motion system consists of two primary lenses fastened to a 0.125 *in* wide, stainless steel sliding bar. The bar is guided by a 0.625 × 0.325 *in*, ball bearing block. One of the original motion

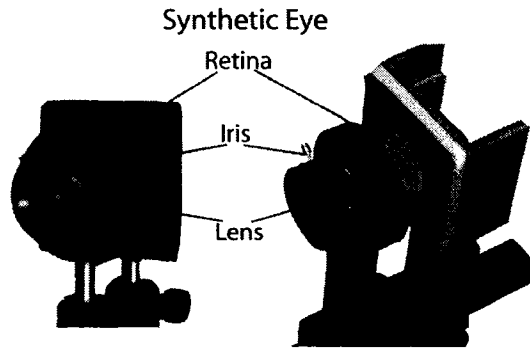


Figure 7.2: Synthetic Eye

system support frames was adapted to hold the primary lens system.

A gear ratio of 2 : 1 was applied with a 42 toothed, 0.25 in diameter steel gear on the motor shaft, meshed with a 84 tooth 0.5 in gear. This drives a 0.5 in diameter, nylon pulley with 0.0625 in wide rounded groove.

Two identical pulleys are connected with a 4.3 in circumference nylon band with a circular cross section of a 0.0625 in diameter.

The drive band connecting the pulleys has a small rigid bar fixing it to the slide bar that holds the lenses.

All of the rotating shafts in the motion system are supported with a light, stainless steel, sealed ball bearing, with an external diameter of 0.25 in and an internal diameter of 0.125 in.

7.2 Model Development

The model consists of four major elements: an optical ray tracer, detector, mechanical motion, and controller. The optical ray tracer is used to determine if the probe beam intercepts an ocular

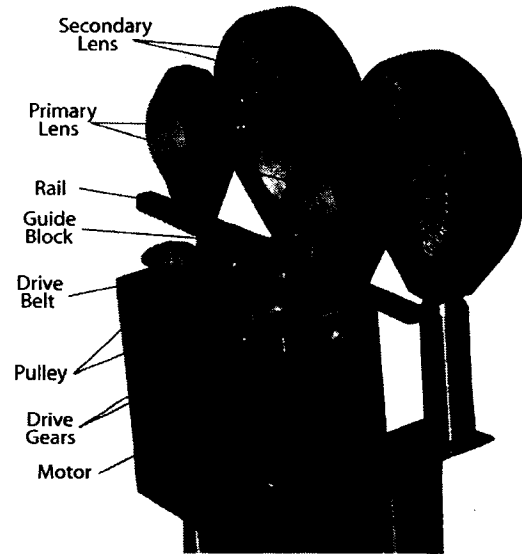


Figure 7.3: Alvarez lens motion setup

system and, if so, where the target is located within the beam. The detector system produces a simulated voltage signal based on the location of the return beam of the optical ray tracer. Signal processing provides an error voltage to the controller. The controller is a linear PID controller. The gains are based on producing an appropriate response time of roughly 0.1 sec. Finally the electro-mechanical model simulates the motion of the primary lens and its actuators. The overall simulation design block diagram is located in figure 7.4.

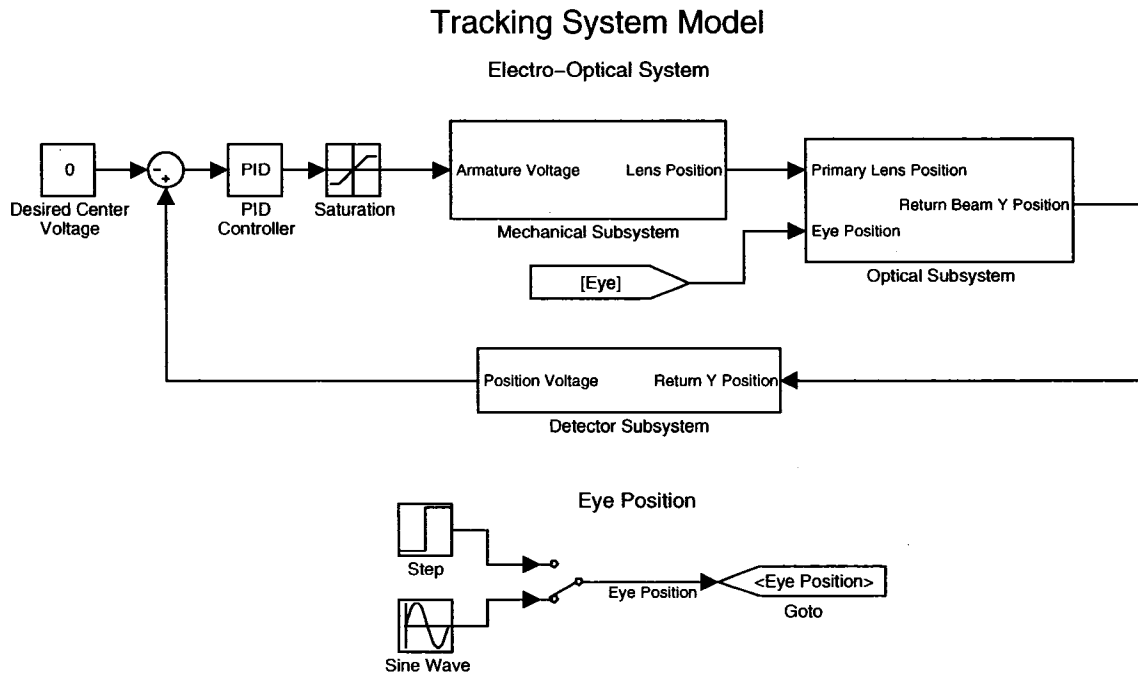


Figure 7.4: Simulink ElectroMechanical Simulation Model - In this instance the first order polynomial estimation of return beam position is used.

7.2.1 Mechanical Model

The various components in the electromechanical model are shown in a free body diagram illustrated in 7.5. This is a simplified model. The rotary system inertias are summed to form one equivalent moment of inertia, and any translating mass was included in the mass of the lens system.

From Newton's Law, the sum of the torques is equivalent to the total moment of inertia times

Lens Motion System Free Body Diagram

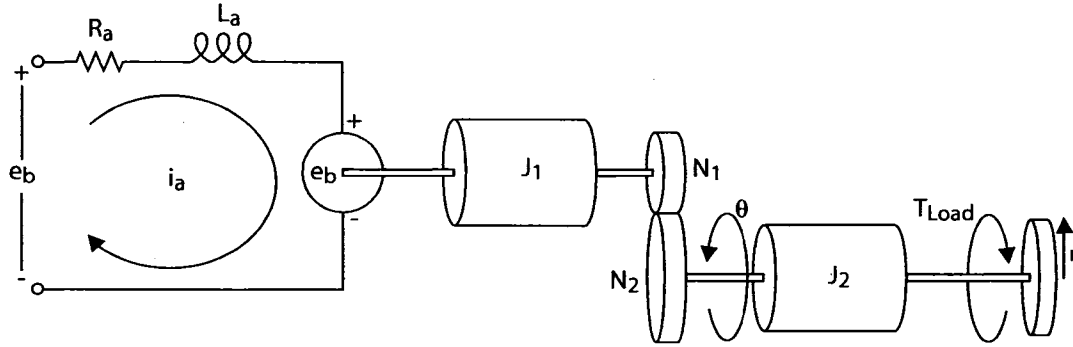


Figure 7.5: Lens System Free Body Diagram

the angular acceleration of the body.

$$\sum T = J\ddot{\theta} = T_{Input} - T_{Friction} - T_{Load} \quad (7.1)$$

where J is the equivalent moment of inertia, θ is the angular displacement of the drive shaft, T_{Input} is the applied motor torque, $T_{Friction}$ is the torque due to rotational friction, and T_{Load} is the load torque necessary to move the massive lens holder assembly. The equivalent moment of inertia J is defined by:

$$J = J_1 N^2 + J_2 \quad (7.2)$$

The inertial subcomponents J_1 represents the moment of inertia of the motor, and drive gear, while J_2 is the moment of inertia for the driven gear, pulley and the shaft connecting them.

The input torque is derived from the electrical current and the motor torque constant:

$$T_{Input} = N k_t i \quad (7.3)$$

where N is the gear ratio between the motor and drive shaft, k_t is the motor torque constant, and i is the electrical current running through the motor coil.

The torque due to friction is based on the angular velocity and viscous damping of the various mechanical components including bearings. These values will be ignored in the preliminary

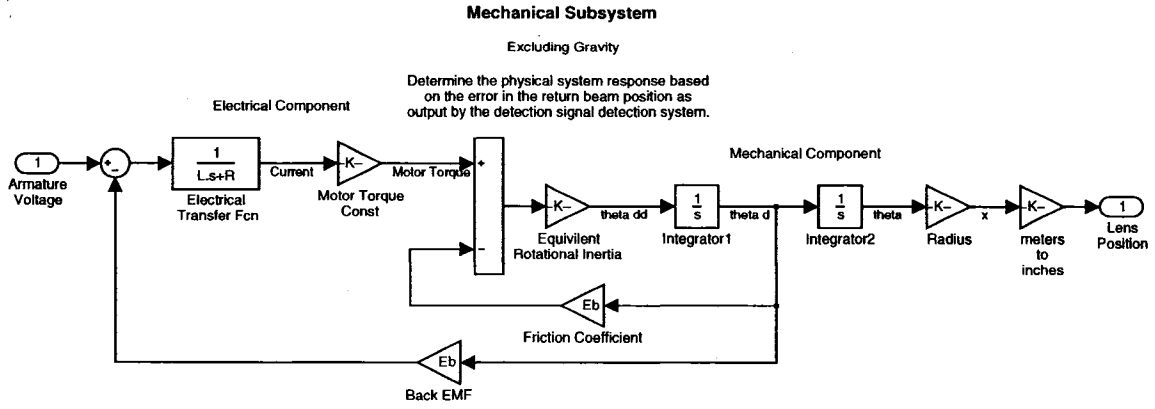


Figure 7.6: Electro-Mechanical model.

analysis as they are difficult to measure, and they are expected to be small.

$$T_{Friction} = B\dot{\theta} \quad (7.4)$$

where B is the equivalent damping factor as defined by

$$B = B_1 N^2 + B_2 \quad (7.5)$$

The load torque depends on the radius of power linkage pulleys, mass of the carriage assembly, and ordinate direction of motion (i.e. parallel or transverse to the direction of gravity).

$$T_{Load} = r \times F_{Load} \quad (7.6)$$

where F_{Load} is the load force from the carriage assembly and r is the radius of the drive pulley. The load force is found by applying Newton's Law to the sum of forces on the carriage assembly.

$$\sum F = m\ddot{x} = F_{Load} - F_{Friction} - m\psi g \quad (7.7)$$

where m is the total carriage system mass, ψ is the directional component of gravity, and g is the acceleration due to gravity. The load force is:

$$F_{Load} = m(\ddot{x} + \psi g) + F_{Friction} \quad (7.8)$$

The frictional force $F_{Friction}$ is assumed to be a viscous damping force and is expected to be small.

To transform the angular position to a linear position, the angular position found by dividing the linear position by the radius of the pulley driving the belt that positions the lens carriage.

$$\theta = \frac{x}{r} \quad (7.9)$$

Developing the differential equation in terms of x using equations 7.1 and 7.8 produces:

$$\left(\frac{J}{r} + rm\right)\ddot{x} + \left(\frac{B}{r} + B_m r\right)\dot{x} + rm\psi g = Nk_t i \quad (7.10)$$

The electrical subcomponent of the system is derived from Kirchoff's voltage loop law.

$$e_a - e_b = L_a \frac{di}{dt} + R_a i \quad (7.11)$$

where e_a is the applied armature voltage, L_a is the motor coil inductance, and R_a is the coil resistance. The back electromotive force (EMF) voltage e_b is dependent on the motor angular velocity.

$$e_b = \frac{k_b}{N} \dot{\theta} = \frac{k_b}{rN} \dot{x} \quad (7.12)$$

Performing the Laplace transform on both the electrical and mechanical subcomponents of the system yields

$$\left(\left(\frac{J}{r} + rm\right)s^2 + \left(\frac{B}{r} + B_m r\right)s\right)X(s) = (Nk_t + rm\psi g)I(s) \quad (7.13)$$

Assuming the gravity component (ψ) is small:

$$\frac{X}{I} = \frac{Nk_t}{\left(\frac{J}{r} + rm\right)s + \left(\frac{B}{r} + B_m r\right)s} \frac{1}{s} \quad (7.14)$$

The transfer function for the electrical component is:

$$\frac{I}{E_a - E_b} = \frac{1}{L_a s + R_a} \quad (7.15)$$

where

$$E_b = \frac{k_b}{rN} sX \quad (7.16)$$

It is possible to compose a single transfer function from the two subcomponents, but for ease of model construction will remain as is.

The mechanical models are applied to Simulink®[®], a simulation package developed by The MathWorks company. This provides an estimate of the system response to inputs and a means to monitor various system requirements including current draw, torque output, lens displacement, etc.

The resulting model can be found in figure 7.6. Note that the electronic portion and mechanical portions were kept separate to ease the implementation of the model for the simulation.

7.2.2 Optical Model

Optical model development is pursued to increase model flexibility. It allows for various lens configurations without recomputing the estimated lens focal lengths. The optical system model consists of a basic ray trace algorithm that traces a simulated laser beam through the desired lens systems. The basis for the ray-trace is Snell's Law

$$n_1 \sin \theta_1 = n_2 \sin \theta_2 \quad (7.17)$$

where n_m is the material index of refraction and θ_m is the incident angle of a ray compared to the normal of the medium interface.

The simulation subsystem was primarily a link to the ray trace algorithm. The Simulink ® model appears in figure 7.7.

The algorithm itself is fairly extensive, and can be found in appendix A .

The ray trace is dependent on the lens geometry, the index of refraction of the lens material, and the lens position relative to the rays. The lens geometry is built on the lens surface radii, the lens diameter, and the edge thickness.

The origin and vector angle of a ray is initialized and recalculated at each medium interface. If the ray misses the optic, it maintains the same heading.

A set of two rays representing the boundaries of a divergent laser beam is traced through the optical model. An example of a ray trace through the model is found in figure 7.8. A test of the eye position determines if the laser beam intercepts the eye. If so, a return beam is traced back

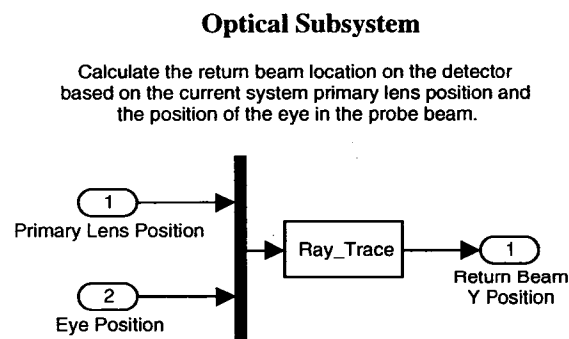


Figure 7.7: Optical Subsystem - primarily provides a link to the ray trace algorithm.

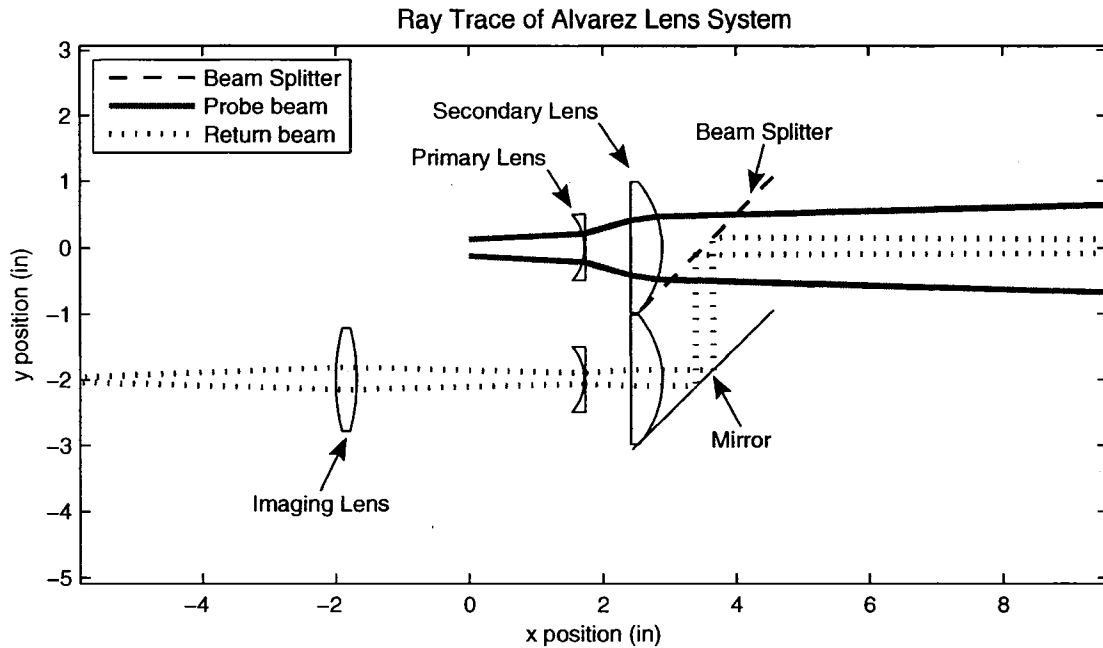


Figure 7.8: Ray Trace of System Model - Displays the results of an actual ray trace performed in the simulation model. Note that the return beam has little divergence. In this case the eye had been centered in the probe beam.

from the retina, through the eye (as shown in figure 7.9) and then through the optical system. If the retro-reflection is found to hit the detector, the detector returns the position of the beam on the detector. If not, the returned beam position is zero, which theoretically produces the same detector output as if the beam was centered on the detector, providing no error signal.

The return beam representing the retro-reflection is calculated using the eye as the beam origin, and following the normal of the outer surface of the secondary lens. This represents the path for the center of the retro-reflection image. The optic coordinates are translated for the return beam calculations so the beam is always oriented in a positive direction. Note that the order and sign of the surface radii must be changed to be consistent with the ray's view of the lens.

The return beam in the eye is narrower than the input probe beam. The divergence limit of the return beam is a function of the iris diameter. However, the extra calculation time required to recursively determine the initial angle limits of the probe beam are skipped in favor of estimating the necessary limiting angle based on the diameter of the iris. Although slightly underestimating

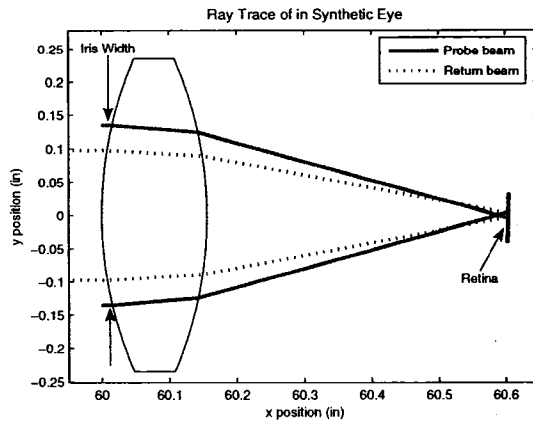


Figure 7.9: Ray Trace in the Eye - Displays the result of tracing the probe beam and reflection in and out of the eye. Note the return beam is slightly narrower than the input beam. This is a result of the limit calculations, which were designed to prevent beams with a divergence greater than the width of the iris from escaping.

the return beam divergence angle, it falls within only a few percent difference of the expected value.

The model was programmed and implemented in MATLAB® and Simulink®. The output of the primary lens position from the mechanical model is fed into the optical model to begin the ray trace. The optical model outputs the position of the return beam on the detector.

7.2.3 Detector Model

In this particular model the return signal detection is reduced to a DC error signal, rather than including the more complicated signal processing required to actually discriminate the signal. Since the output of the signal processing is expected to be a DC signal, the detector is modeled using two basic methods, both are based on measurements acquired from the actual detector used in the system.

There are two primary models used for the detector in system simulations, a first order normalized polynomial model, and a sixth order normalized polynomial.

The first order polynomial model captures the theoretical normalized position of a laser spot on the quadrant detector silicon. It provides a voltage signal proportional to the return glint spot estimated position. It does not account for detector sensitivity variation due to spot position. The amount of spot energy decreases as it nears the edge of the detector, providing for a lower detector

output voltage (see detector characterization).

$$V_{Error} = \frac{Glint\ Position - Detector\ Center}{Detector\ Radius} \quad (7.18)$$

where V_{Error} is the voltage due to the glint spot distance from the detector center. This provides a better model for a position sensitive detector (PSD) that has a voltage gradient based on the position of a laser spot on the detector surface.

The sixth order polynomial model is based on the results of the quadrant detector characterization. It approximates the change in detector sensitivity variation, allowing for voltage drop off with the spot at the edge of the detector. It also displays the almost binary nature of the detector, where each quadrant outputs the saturation voltage when it is intercepted by a large percentage of the glint image regardless of the glint position within the quadrant. This is represented by equation 7.19.

$$V_{Error} = 10992x^6 + 17443x^5 - 615.46x^4 - 1107.1x^3 + 16.684x^2 + 19.406x \quad (7.19)$$

where x is the horizontal position of the spot on the detector, and V_{Error} is the detector voltage output expected from the detection circuitry. This equation only applies to one DOF of the detector.

Simulations of the detector are used to evaluate both of these polynomials. The detector model shown in figure 7.10 exhibits use of the simpler first order polynomial.

7.2.4 Controller Model

The controller is a simple proportional, integral, derivative (PID) controller.

Little integral control is required because the motors act as mechanical integrators. Barring any significant friction, the motors provide zero steady-state error. The fast time response and overshoot is a function of the proportional and derivative gain. Proportional gain is the primary term used in tuning the system for a rapid response time. Small measurement errors and noise can produce significant error with heavy derivative contributions to the control signal.

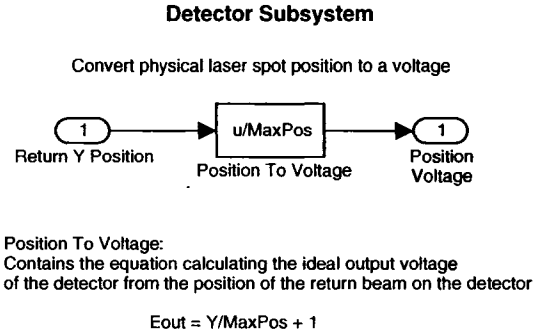


Figure 7.10: Detector Subsystem - In this instance the first order polynomial estimation of return beam position is used.

Gains for the controller components are determined mainly through experimentation. The system gain is adjusted until the speed of response was deemed to be less than 0.1 s. Derivative gain was then included to prevent heavy system oscillation, reducing the settling time of the system. It turns out the gains for the derivative component for this model were very small, and the desired system response could be simulated with using just a proportional gain value.

For a majority of the tests, a simple proportional gain of 4 was applied to the error voltage. Since the model has little friction, this value will need to be modified and increased on the physical system.

7.2.5 Simulation Results

The simulation produced some promising results. The simulated system was able to track the eye at a rate of roughly $8 \frac{in}{s}$ with a phase lag of less than 0.02 s.

The plot in figure 7.11 shows the position of the primary lens of the Alvarez lens system along with the position of the eye. Note that only a small displacement of the primary lens is necessary to track the much larger displacements of the eye. The positions are also polar opposites which is expected as the lens should move in the direction opposite the eye is moving.

Figure 7.12 shows the time lag between the eye position and the primary lens position. Both have been normalized and the lens position negated to ease comparison. The primary lens does lag slightly behind the eye, which is expected, but only by 0.02s.

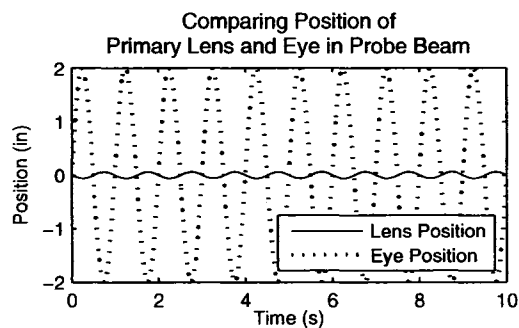


Figure 7.11: Results of oscillating the eye within the probe beam at roughly $8 \frac{in}{s}$. Note that direction of lens movement is opposite the direction of the eye motion.

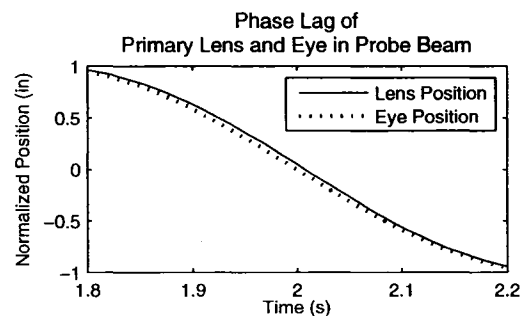


Figure 7.12: There is a small time lag, as expected, which means the beam tracks slightly behind the position of the eye.

For the step input response, the eye was placed 60 *in* from the output lens, and displaced -1 *in*. The results can be found in figure 7.13. Note the rapid response time of the results; the lens reaches steady state in well under a tenth of a second.

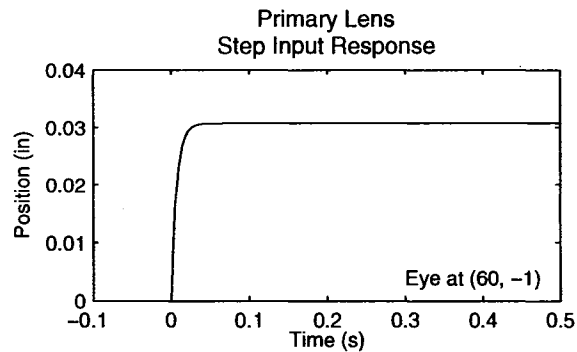


Figure 7.13: Model Step Input Results - response time of the system is approximately 0.04 *s* for an angular displacement of the eye about 1° .

7.2.6 Model Assessment

Model verification produces promising results. The beam displacements produced by the Alvarez lens pair in the optical model are not significantly different from those measured in the lab. Lab measurements were conducted by moving the primary lens a known amount with a micrometer, and measuring the beam displacement with a tape measure. Both the optical model and the lab measurements produce a beam displacement range of approximately $\pm 10^\circ$.

The angle displacement of the output probe beam is compared to the measured displacement of the output probe beam of the physical model. The measurements of the primary lens displacement and the output probe beam were taken with a set of dial calipers. The measurements of the probe beam were taken at 76 *in* from the output of the secondary lens. The angle of the beam is then calculated. A comparison of the output angle of the Alvarez lens pair of the physical model and the simulation can be found in figure 7.14. Note that the simulation results closely follow the linear fit of the measured results. It can be expected that there is a significant amount of error in the measurements made of the beam displacement. Also, the exact distances between lenses of the physical model are subject to error. The results of the simulation provided a surprisingly close

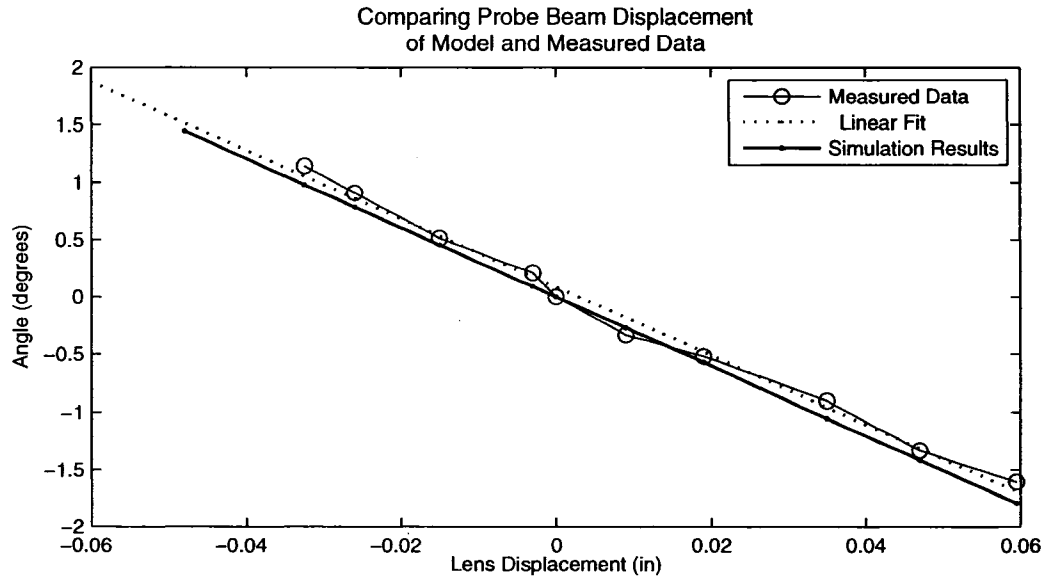


Figure 7.14: Comparing Beam Displacements - the angular displacement of the probe beam as a function of the primary lens displacement was compared between measured values of the physical model and the computer simulation. The simulation approximation was determined to be acceptable.

approximation of the actual beam angular displacement of the physical model.

The mechanical model is much more difficult to validate. Friction is ignored in the mechanical model which makes it inherently inaccurate. Other considerations, including bearing inertia and belt weights are also ignored as they were orders of magnitude below the mass of the primary lens. No limitations are set on the mechanical model attributes such as position, input voltage, current draw, and output torque. During simulation of the model, these parameters are monitored closely to ensure that they do not exceed system specifications of 1Ampere current draw, 12V input voltage, and 0.551oz in of torque output from the motor. These system specifications are derived from the physical limitations of the motors, and the power supplies used to drive the motors.

7.3 Analog Circuitry

Analog circuitry is required to interface the quadrant detector measurement device with the DSP. Also, the PWM output of the DSP must be translated into voltages and currents that can be used by the lens drive motors.

7.3.1 Signal Conditioning

The input from the detector needs to be conditioned prior to entering the digital signal processor. The signal must be in the proper voltage range, and an anti-aliasing filter must be applied to prevent high frequency harmonics of the sampling frequency from being aliased at a lower frequency within the digitally sampled data. A schematic of the conditioning circuitry is found in appendix C1.

The input from the quadrant detector is buffered to prevent a current drain and subsequent voltage drop of the input voltage. Although this may be accounted for in the actual quadrant detector hardware, it was not mentioned in the documentation of the quadrant detector.

The buffered signal is passed through a bandpass filter. It acts as an anti-aliasing filter, preventing high frequency components from being sampled, and removes the DC component from the detector signal. All that remains is the oscillating signal from the pulsing probe beam with zero mean.

The amplitude of this signal is adjusted with an inverse gain operational amplifier configuration. The amplitude was made adjustable with the use of potentiometers. The effective sensitivity of the quadrant detector measurements can also be adjusted.

A constant DC value of 1.4 V is added to translate the mean of the oscillating signal to half the voltage range of the DSP. The DSP has an operating input voltage range of 0 to 3 V. However, the conversion remains more linear between 0 and 2.8 V. The added DC value is also adjustable by potentiometer.

The output voltage of the signal conditioning circuitry is regulated with a series of diodes to ensure that the input voltage to the DSP does not exceed 3 V and does not fall below 0 V. Three standard diodes are placed in parallel between the output voltage and ground to regulate the maximum output voltage. One diode is placed in series with the output voltage to prevent current reversal to the DSP.

7.3.2 H-Bridge

A standard H-bridge configuration is used to translate the PWM output into drive voltages for the motor. In this case a standard H-Bridge chip, ST Microelectronics L293, is used.

The H-bridge amplifies the output of the PWM and turns on different current directions with the positive and negative cycles of the PWM. The average flow of current is determined by the duty cycle of the PWM output.

The schematic for the H-bridge circuitry can be located in appendix C2.

CHAPTER 8

SYSTEM RESPONSE EXPERIMENTATION

In order to test the effectiveness of the tracking system, an experiment was designed to measure the response time in centering the eye in the probe beam based on angular deflection of the eye in the probe beam.

8.1 Experiment Design

To simulate the angular deflection of the eye, the eye remained stationary while the beam is reflected off a rotating mirror. Changing the angle of the mirror deflects the probe beam from the eye and simulates motion of the eye through the probe beam. The basic design can be found in figure 8.1. Note that the plane of the mirror surface must pass through the axis of the mirror rotation to form accurate angular measurements.

A rotatory potentiometer is used to monitor the angular deflection of the mirror. The potentiometer is attached to the mirror with a set of gears. The gear ratio of 1:2 increases the sensitivity of the potentiometer in relation to the angular position of the mirror. A fixed voltage (5 V) is applied across the potentiometer. The voltage between the tap lead and ground will change according to the angular position of the mirror.

Storing and analyzing both the angular position of the mirror, and the normalized position of the retro-reflection on the detector on the DSP, an estimate of the system response time can be formulated.

The angle of the mirror is manually adjusted.

5 Volts are applied across the 5 k Ω potentiometer. The output voltage is conditioned with a summing amplifier and an inverting amplifier prior to collection by the ADC on the DSP chip. A schematic of the design can be found in appendix D1.

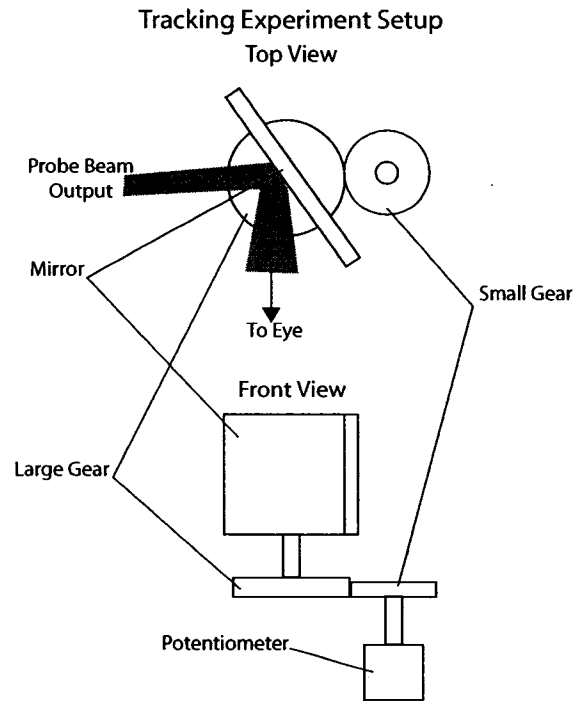


Figure 8.1: Eye Tracking Experiment Basic Setup - shows the basic design used to simulate horizontal movement of the eye by changing the angular position of the output probe beam. The angular position is measured using a rotary potentiometer.

8.2 Data Collection Inclusion

The DSP algorithm is modified to include collection of the angular position of the mirror as well as the normalized position of the retro-reflection. To include enough information, data collection occurs for a minimum of 5 seconds. The data is collected in circular buffers to prevent memory overflow, and to leave the execution and halting of the program to the digression of the experimenter.

With a DSP sample rate of 8000 *Hz*, the data collection is downsampled to 500 *Hz* to preserve memory usage. This means a datum for the normalized position and the beam deflection is taken every 16 cycles. The power of two (i.e $2^4 = 16$) is again used to make for efficient circular counters within the DSP code.

The data collection code, which is included in the DSP code, can be found in appendix B1. It has been commented out for normal DSP operation.

8.3 Calibration

In order to accurately measure the angular position of the mirror used to simulate the displacement of the synthetic eye, the data collection system must be calibrated.

Three angular positions of the mirror are measured: $+8^\circ$, 0° , -8° . The probe beam is centered at these angles using the displacement mirror. The voltage data from the rotary potentiometer connected to the displacement mirror is collected using the DSP.

The collected voltage data is averaged to form the voltage for the given angular position. This voltage is converted by the ADC into a 12 bit integer, so it must be converted back to voltage value by finding the quotient of the integer value and $2^{12} - 1$. A plot of the angular displacement versus the calculated voltage values is located in figure 8.3.

The linear fit to the data appearing in figure 8.3 is used to convert voltage values measured during experimentation into angular positions of the displacement mirror. In this instance the linear fit was found to be:

$$\theta = 13.52381v - 16.92846 \quad (8.1)$$

where θ is the angular displacement of the mirror, and v is the voltage corresponding to that angular displacement.

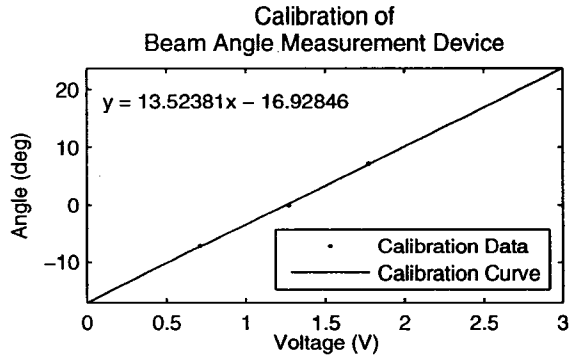


Figure 8.2: Angular displacement calibration

8.4 Tuning the Controller

The simulations generated by the model discussed in chapter 7 are used to estimate gains for the controller. The simulation proved that a proportional-derivative (PD) control algorithm can be used to provide an adequate system response time. For ease of experimentation, and adjustment, gains are initially adjusted through bitshifts. This proved effective during the initial experimentation and deployment of the control algorithm.

The calculated position of the return glint on the detector has a bias. That is, when the beam reflected from the eye is centered on the detector, the calculated position of the reflection is not zero. This is a result of slight variations in sensitivity of the detector active surfaces, and gain variation from the analog circuitry used to condition the input signals. The analog discrepancies are primarily due to gain adjustments made on the signal using operational amplifiers. Tuning of the analog circuitry is done using a digital oscilloscope. Gain adjustments to the circuitry are performed by centering the return signal from the eye on the detector. Then potentiometers are adjusted until there is visual overlap on the oscilloscope of conditioned voltages from the two channels used on the detector.

The position bias is removed by subtracting a constant value from the calculated position of the reflection on the detector before it is passed to the controller. This value was roughly 18000, or about 0.55 on a normalized scale. Although this is a large percentage of the total scale, this fact was not considered during the course of experimentation.

The controller is tuned primarily through trial and error. The values obtained for a PD controller from simulations are used as starting points for gain values in the digital controller. These gain values had to be converted because the voltages from the detector are measured with 12-bit values while the output from the PWM is 16-bit values. The gain value of 4 estimated from system simulation must be multiplied by 2^4 to obtain an appropriate proportional gain value of 2^6 .

8.5 Controller Results

The controller algorithm is included in the software of the DSP. It adjusts the duty cycle of the PWM output from the chip to control the motors.

The pulse frequency of the PWM is set at a fixed number of clock cycles between pulses. The duty cycle of the pulse is controlled by an integer value representing the number of clock cycles the pulse is hi. This must be a positive integer value less than or equal to the number of clock cycles per pulse.

To obtain a 50% duty cycle, and prevent the motor from turning, the output value of the controller must half of the number of clock cycles per pulse of the PWM. In this instance the PWM outputs 6000 Hz, which for a 150 MHz processor is 12500. (Note that the PWM operates every other clock cycle, so its maximum output is 75 MHz).

The output of the controller is biased by 6250, which is half the number of clock cycles the PWM output is hi. This means that the duty cycle of the PWM will be 50% when there is no error in calculated position of the return glint on the detector. Then the motor will not turn.

```
PositionTimeDerivative= CurrentPosition - LastPosition
BiasedPosition = CurrentPosition + 18000; if ((BiasedPosition > 8000)
| (BiasedPosition < -8000)){

    ControllerOutput = (6250 + (BiasedPosition >> 5) +
        (PositionTimeDerivative));

if(ControllerOutput < 0){
    ControllerOutput = 10;
```

```

}

if(ControllerOutput > 12500){
    ControllerOutput = 12490;
}

}else{
    ControllerOutput = 6250;
}

LastPosition = CurrentPosition;

```

The derivative is essentially the difference between the normalized retro-reflection spot position on the detector at the current time step and the previous time step because the ADC samples the input at a constant rate. The division by the time step is included in the gain of the derivative component of the controller.

Note that the controller output is limited so that it cannot output values outside the range the PWM can accept. This means no values less than 0, or values greater than 12500, which is the number of clock cycles per pulse of the PWM.

The gains are adjusted by bit shifts. Although this is not entirely necessary, it is the simplest, and fastest method to perform gain operations on values. All of the bit shifts are to the right to ensure that the output value falls between the 0 and the number of clock cycles per PWM output pulse.

The gain values had been estimated through simulation with the computer models of the system. Adjustments are made on the physical model through trial and error. The proportional gain is increased until the system goes unstable. The proportional gain is then reduced until the probe beam oscillates about the synthetic eye. Then the derivative gain is increased to dampen the oscillations, so the probe beam would center on the synthetic eye.

This particular controller provides sufficient tracking capability for the synthetic eye manually translated through the range of motion of the tracking probe beam for a relatively close range.

8.6 System Malfunction

System experimentation is unable to continue beyond preliminary stages. The DSP component of the system is malfunctioning, both due to human error, and unforeseen circumstance. Unfortunately there is not enough time or resources to replace the DSP.

Each component of the entire system has been proven to work individually, including the DSP. However, the entire system has not been fully functional except for one brief period. The system has tracked the synthetic eye. The only evidence of this is observation by the author.

This is not to imply the system is tragically flawed. Only that further experimentation and development is required to improve the device operation.

CHAPTER 9

CONCLUSIONS AND RECOMMENDATIONS

Although the entire system was unable to consistently track the synthetic eye, experimentation with the current design has produced some promising results.

When functional, the system using the Alvarez lens system is able to track the synthetic eye at a range up to 3 *m*. Optical noise generated within the device can be drastically reduced by using an optical configuration that separates the transmitting and receiving paths of the probe beam as much as possible. Motors can be used to adjust the Alvarez lens system to track a synthetic eye. Signals from a quadrant detector can be used to track the synthetic eye through retro-reflection of a probe beam. Finally, a simple digital PD controller can be used as the tracking algorithm.

9.1 Conclusions

This technology shows promise for tracking retinal retro-reflection of an infrared probe beam in order to provide a target dependent white light flashblinding pulse.

Background research shows that inducing flashblindness is possible through the use of white light. Further research must be performed to find appropriate dosages of white light, especially in daylight conditions.

It has been shown that retro-reflection of a probe beam can be used to track a subject's eye. Research indicates that an infrared laser beam with a wavelength of 1070 *nm* is the most effective for obtaining a retro-reflection from the human retina. This is also a relatively safe wavelength of radiation to the eye, making it appropriate for large dosages of probe beam to intercept the eye.

The mechanical system design used to position the Alvarez lens has proven effective. The mass of a parallel optical path system may be of concern, especially as the planer motion of the Alvarez lens is introduced. The construction of the current system is relatively massive and not very precise. However, it is still able to perform correctly.

The signal processing algorithm has proven highly effective. It can produce a consistent output for simulated signals from two channels of the position detector. It also produces a relatively consistent position of a synthetic eye within the probe beam using the actual quadrant detector.

The controller has been used to track the synthetic eye at relatively close ranges. Further work is needed to improve the controller design, but at the moment proves sufficient to demonstrate the overall design can work.

Friction is a primary adversary to the current control design. Although the controller has proven sufficient, in future application, friction reduction will be necessary to improve accuracy and primary lens position sensitivity.

9.2 Future Work

There are a number of aspects of this design that must be improved and implemented.

9.2.1 Mechanical Design

The introduction of planar translation of the primary lenses of the Alvarez pairs is imperative. This will allow the system to track the retro-reflection in space rather than along the horizontal plane that intercepts the optical axis.

It could also prove useful to include a third axis of motion to include the option of changing the divergence rate of the output probe beam for providing more effective retro-reflective returns over a range of target distances.

It may be possible to eliminate the motion of the second Alvarez lens pair in the return optical axis. This will be discussed further in future work of target discrimination.

9.2.2 Target Discrimination

The quadrant detector provides little target resolution. In fact if multiple targets do appear within the probe beam, they will be averaged by the quadrant detector.

A better approach is to use a CCD or equivalent array with greater resolution of active surfaces to use for signal detection and localization.

The use of a CCD array in conjunction with the signal processing algorithm could provide a means to distinguish between multiple targets falling within the probe beam and determining the more susceptible target.

Target discrimination using such an array would also require some video-image processing to determine if separate distinct glint returns do actually fall on the detector.

With the advent of a CCD array, it may also be possible to eliminate the motive second axis Alvarez lens pair. Instead a series of collecting lenses can be used to project the return glint onto the CCD array. Instead the position of the glint could be compared to a measured position of the Alvarez lens pair used to adjust the angle of the probe beam output and ultimately the flash.

The position of the Alvarez lens provides for predictable deflection angles on both the output and return glint signals. An algorithm could be developed to provide a digital means of centering the return glint signal rather than a mechanical.

9.2.3 Signal Processing

An algorithm has been developed to measure the amplitude of the signals intercepting the detector. Since it was not needed for the purposes of this particular aspect of the project, it was eliminated from the design and discussion for the sake of simplicity.

Measuring the amplitude of the signal intercepting the detector provides for an estimate of the power of the return. The greater the amplitude the more powerful the return glint, the more susceptible the eye is to the flash.

The algorithm used in both signal recognition and amplitude measurement is highly scalable. It can be expanded to perform over many channels without an exponential increase in resources. In fact the greater number of channels increases the resource efficiency as a greater percentage of memory is then devoted to data collection and storage rather than calculation and manipulation.

Ideally this algorithm could be applied to much faster and more expansive DSP chips such as FPGAs.

Using this algorithm to discriminate the returning probe beam in conjunction with video-image processing would vastly improve the system target discrimination.

Signal processing must also be modified to include target distance. The amount of energy in the flash pulse delivered to the target is dependent on distance, as well as a number of other factors, including the pupil diameter and atmospheric attenuation. To separate these elements from energy loss from divergence of the probe beam due to distance traveled, the distance to the target must be measured. This may require a faster probe beam pulse rate, as well as phase change measurements of the probe beam.

BIBLIOGRAPHY

- [1] Francois C. Delori and Kent P. Pflibsen. Spectral reflectance of the human ocular fundus. *Applied Optics*, 28(6):1061–1077, 1989.
- [2] W.A.H Rushton and G.H. Henry. Bleaching and regeneration of cone pigments in man. *Vision Research*, 8:617–631, 1968.
- [3] Norma D. Miller. Visual recovery from brief exposures to high luminance. *J. Optical Society*, 55(12):1661–1669, 1965.
- [4] Robert A. Capobianco. Curing equipment for assembly applications. Application Note AN-103, Xenon Corporation, Woburn, MA, 2002.
- [5] Richard Dennis, James Harrison, Wallace Mitchell, Douglas Apsey, Steven Cora, and John Williams. Visual effects assessment of the green laser-baton illuminator (glbi). Report 189571, U.S. Department of Justice, Brooks AFB, Texas, 7 August 2001.
- [6] Ben Pansky. *Dynamic Anatomy and Physiology*. Macmillan Publishing Co, New York, 1975.
- [7] A.J. Vander, J.H. Sherman, and D.S. Luciano. *Human Physiology: the Mechanisms of Body Function*. Fourth edition.
- [8] Kevin D. Ridge, G. Najmoutin, Marcelo Sousa, and Krzysztof Palczewski. Phototransduction: crystal clear. *TRENDS in Biochemical Sciences*, 28(9):479–487, 2003.
- [9] Julie L. Schnapf and Denis A. Baylor. How photoreceptor cells respond to light. *Scientific American*, 256(4):40–47, 1987.
- [10] Marie E. Burns and Trevor D. Lamb. Visual transduction by rod and cone photoreceptors. *Retinal Mechanisms*, 49:267–268, 1975.
- [11] M.D. Bownds and V.Y. Arshavsky. What are the mechanisms of photoreceptor adaptation. *Behavioral and Brain Sciences*, 18(3):415–424, 1995.
- [12] ICNIRP. Guidelines on limits of exposure to broad-band incoherent optical radiation (0.38 to 3 m). Technical report, Health Physics Society, 1997.
- [13] Randolph D Glickman. Phototoxicity to the retina: Mechanisms of damage. *International Journal of Toxicology*, 21:473–490, 2002. American College of Toxicology.
- [14] Johannes J. Vos and Dirk van Norren. Thermal cataract, from furnaces to lasers. *Clinical and Experimental Optometry*, 87(6):372–376, 2004.

- [15] LIA. Ansi z136.1 - 2000. *American National Standard for Safe Use of Lasers*, June 2002.
- [16] D. van Norren and L.F. Tiemeijer. How photoreceptor cells respond to light. *Vision Research*, 26(2):313–320, 1986.
- [17] D. H. Sliney and M. L. Wolbarsht. *Safety with Lasers and Other Optical Sources*. Plenum Press, New York, 1980.
- [18] M. Hollins and M. Alpern. Dark adaptation and visual pigment regeneration in human cones. *J. General Physiology*, 62:430–447, 1973.
- [19] LIA. Ansi z136.6 - 2000. *American National Standard for Safe Use of Lasers*, August 2002.
- [20] Michael F. Modest. *Radiative Heat Transfer*. McGraw-Hill Inc, New York, 1993.
- [21] G.S. Brindley and E.N. Willmer. The reflexion of light from the macular and peripheral fundus oculi in man. *Journal of Physiology*, 158:350–366, 1952.
- [22] O.A.R. Mahroo and T.D. Lamb. Recovery of the human photopic electroretinogram after bleaching exposures: Estimation of pigment regeneration kinetics. *J Physiology*, 554(2):417–437, 2003.
- [23] J.K. McBee, K. Palczewski, W. Baehr, and D.R. Pepperberg. Confronting complexity: Photo-transduction and retinoid metabolism in the vertebrate retina. *Prog Retina Eye Res*, 20(4):469–529, 2001.
- [24] M.A. Sandberg, B.S. Pawlyk, and E.L. Berson. Acuity recovery and cone pigment regeneration after a bleach in patients with retinitis pigmentosa and rhodopsin mutations. *IOVS*, 40(10):2457–2461, 1999.
- [25] Timothy Upton, David Watt, and Jacques Ludman. Smart white dazzler. *Proceedings of the SPIE*, 5403(6):493–501, 2004.

APPENDICES

APPENDIX A
MATLAB RAY TRACE CODE

A.1 Lens Structure

```
% LENS_STRUCTURE - a script file the creates the data
% structure of the current optical system configuration.

global Beam % Contains starting location and initial
% divergence of the laser beam
global Eye % Structure containing position data
% of the eye
global Retina % Position and size of the diffuse reflective
% surface of the retina.
global Mirror % Structure containing position and angle data
% of beam splitter and mirror of optical
% system.
global Lens % Structure array with position, and lens
% characteristics including surface radii,
% thickness, diameter, index of refraction,
% and direction of normal.
global Detector % Position and detection characteristics of the
% photodetector.
global Second_Axes_Position % Relative position of the return axis.
global Beam_Out % Array containing beam information for drawing
% the beam traces on a plot
global Beam_In_Eye
global Beam_Return
global myHandles

Primary_Lens_Position = 0; % Y-locations of outgoing and return optical axii
Second_Axes_Position = -2;

%Default Beam Settings [x y alpha]
Beam = [ ... %0 0 0; ...
        0 -0.125 -0.0524; ...
        0 0.125 0.0524];
%      1.3 -0.125 0.023259; ...
%      1.3 0.125 -0.023259];

%Default Eye parameters
Eye.Position = [60 0 0];
Eye.Pupil_Diameter = 0.27;
```

```

Eye.Lens_Diameter = 0.47;
Eye.Thickness = 0.06;
Eye.Surface_Radii = [0.6 -0.6];
Eye.Refractive_Index = 1.6;
Eye.Normal = 0;

%Default Retina parameters
%Retina.Distance = 0.62675;
Retina.Distance = 0.6;
Retina.Position = [Eye.Position(1)+Retina.Distance Eye.Position(2:3)];
Retina.Width = 1;
Retina.Normal = 0;

%Default Mirror parameters
Mirror(1).Position = [3.5 0 0];
Mirror(1).Normal = pi/4;
Mirror(1).Width = 3;

Mirror(2).Position = [3.5 Second_Axes_Position 0];
Mirror(2).Normal = -pi/4;
Mirror(2).Width = 3;

%Default Detector settings
Detector.Position = [-4.915 Second_Axes_Position 0];
Detector.Sensor_Diameter = 0.309;
%Detector.Position(1) = Eye.Position(1) - Detector.Position(1);

%default lens structure
%Primary Lens Transmitting
k = 1;
Lens(k).Position = [1.725 Primary_Lens_Position 0];
Lens(k).Lens_Diameter = 1;
Lens(k).Thickness = 0.195;
Lens(k).Surface_Radii = [-0.7724 0];
Lens(k).Refractive_Index = 1.785;
Lens(k).Normal = 0;

%Secondary Lens Transmitting
k = 2;
Lens(k).Position = [2.415 0 0];
Lens(k).Lens_Diameter = 1.9685;
Lens(k).Thickness = 0.11811;
Lens(k).Surface_Radii = [0 -1.5449];

```



```

Lens(k).Refractive_Index = 1.785;
Lens(k).Normal = 0;

%Secondary Lens Receiving
k = 3;
Lens(k).Position = [2.415 Second_Axes_Position 0];
Lens(k).Lens_Diameter = 1.9685;
Lens(k).Thickness = 0.11811;
Lens(k).Surface_Radii = [0 -1.5449];
Lens(k).Refractive_Index = 1.785;
Lens(k).Normal = 0;

%Primary Lens Receiving
k = 4;
Lens(k).Position = [1.725 (Primary_Lens_Position+Second_Axes_Position) 0];
Lens(k).Lens_Diameter = 1;
Lens(k).Thickness = 0.195;
Lens(k).Surface_Radii = [-0.7724 0];
Lens(k).Refractive_Index = 1.785;
Lens(k).Normal = 0;

%Focusing Lens Receiving
k = 5;
Lens(k).Position = [-2 Second_Axes_Position 0];
Lens(k).Lens_Diameter = 1.5748;
Lens(k).Thickness = 0.120866;
Lens(k).Surface_Radii = [3.23976 -3.23976];
Lens(k).Refractive_Index = 1.5748;
Lens(k).Normal = 0;

```

A.2 Convert Lens Thickness

```

function NewThickness = ConvertThickness(Surface_Radius, ...
                                         Lens_Diameter, ...
                                         Lens_Thickness)

% CONVERTTHICKNESS converts the lens edge thickness to the
% centerthickness of a spherical lens using the surface radii,
% the lens diameter, and the lens edge thickness

% Determine if the first lens surface is plano
if Surface_Radius(1) ==0
    diffThickness1 = 0; %If the surface is plano, then the
    %point at the center of the lens
    %has the same x value as the point

```

```

%at the edge of the lens
else
    diffThickness1 = sign(Surface_Radius(1))* ...
                    (abs(Surface_Radius(1)) - ...
                    sqrt(Surface_Radius(1)^2 - ...
                    0.25*Lens_Diameter^2));
%Otherwise assume a spherical surface, and calculate the
%change in x position between the edge of the lens
%surface and the point in the center of the surface.
end

%Repeat the procedure for the second lens surface...
if Surface_Radius(2)==0
    diffThickness2 = 0;
else
    diffThickness2 = -sign(Surface_Radius(2))* ...
                    (abs(Surface_Radius(2)) - ...
                    sqrt(Surface_Radius(2)^2 - ...
                    0.25*Lens_Diameter^2));
end

% Calculate the center thickness of the lens by adding the changes
% in x value between the edge of the lens surface and the center of
% the surface to the edge thickness of the lens.

NewThickness = Lens_Thickness + diffThickness1 + diffThickness2;

```

A.3 Optical Medium Interface Calculations

```

function [Beam, Surface_Hit] = Lens_Surface(Lens_Position, ...
    Lens_Diameter, ...
    Lens_Thickness, ...
    Surface_Radius, ...
    Refractive_Index, ...
    Normal_Direction, ...
    Beam)

% LENS_SURFACE performs the refraction calculation at the interface
% of a spherical or plano lens surface and air. This function assumes
% air has an index of refraction of 1, and uses Snell's law to
% calculate the new relative angle of a ray to the normal of the surface.

```

```

LensX = Lens_Position(1);
LensY = Lens_Position(2);

BeamX = Beam(:,1);
BeamY = Beam(:,2);
Alpha = Beam(:,3);

%Check to see if ray can intercept lens geometry

TestY = (LensX - BeamX).*tan(Alpha) + BeamY;

p = (TestY > LensY + 0.5*Lens_Diameter) | (TestY < LensY - 0.5*Lens_Diameter);

% Determine if interface is a plano surface. A radius value of 0 indicates
% a plano surface.
if Surface_Radius == 0

    %Locate intersection of rays with plano surface
    x1 = LensX + Lens_Thickness;
    y1 = (x1 - BeamX).*tan(Alpha) + BeamY;
    % Calculate new ray angle in real world coordinates
    Alpha_New = asin(Refractive_Index * sin(Alpha));

else

    %If the surface is not a plano surface, it is assumed to be a part of a
    %spherical lens surface.

    %Locate center of sphere representing lens surface
    Cx = LensX + ...
        (Lens_Thickness + Surface_Radius).* ...
        cos(Normal_Direction);

    Cy = LensY + ...
        (Lens_Thickness + Surface_Radius).* ...
        sin(Normal_Direction);

    %Corresponding polar angle coordinate of ray interception point in
    %spherical lens surface
    Alpha_Intercept = -sign(Surface_Radius)*(Alpha + ...
        asin(cos(Alpha)/Surface_Radius .* ...
        (Cy - BeamY + (BeamX -Cx).*tan(Alpha))));

    %Calculate interception point of ray on spherical lens surface

```

```

    x1 = -(Surface_Radius)*cos(Alpha_Intercept) + Cx;
    y1 = abs(Surface_Radius)*sin(Alpha_Intercept) + Cy;
    %Calculate angle of incidence
    Thetal = Alpha_Intercept + sign(Surface_Radius)*Alpha;
    %Calculate angle of refraction
    Theta2 = asin(Refractive_Index * sin(Thetal));
    %Convert refraction angle into real world coordinates
    Alpha_New = sign(Surface_Radius)*(Theta2-Alpha_Intercept);

end

% Calculate the new values of ray positions. "p" is a logical array that
% has a value of 1 where the ray did not intercept the lens geometry. The
% inverse of "p" multiplies the new intersection points where rays do
% intercept the lens surface geometry.
x_out = x1 .* ~p + p.*LensX;
y_out = y1 .* ~p + p.*TestY;
%The real world angle vector is preserved for ray elements that miss the
%lens geometry. Otherwise it includes the new angle vector for the ray.
alpha_out = Alpha_New.* ~p + Alpha.*p;
%Surface intersections occur where "p" is false
Surface_Hit = ~p;
%New beam coordinates and angle vector is saved in the output vector.
Beam = [x_out y_out alpha_out];

```

A.4 Ray Trace

```

function [sys,x0,str,ts] = Ray_Trace(t,x,u,flag)
% RAY_TRACE - performs ray trace through the optical system. This is the
% function called by the Simulink model during the simulation.

% The MATLAB Function Block is called automatically with different flags
% depending on the stage of simulation.
switch flag,

    %%%%%%%%%%%
    % Initialization %
    %%%%%%%%%%%
    case 0,
        Num_Outputs = 1;
        [sys,x0,str,ts]=mdlInitializeSizes(Num_Outputs);

    %%%%%%%%%%%
    % Outputs %
    %%%%%%%%%%%

```

```

case 3,
    sys=mdlOutputs(t,x,u);

case {1,2,4,9}
    sys=[];

%%%%%%%%%%%%%%%%%%%%%%%%%%%%%%%%%%%%%%%%%%%%%%%%%%%%%%%%%%%%%%%%%%%%%%%%
% Unexpected flags %
%%%%%%%%%%%%%%%%%%%%%%%%%%%%%%%%%%%%%%%%%%%%%%%%%%%%%%%%%%%%%%%%%%%%%%%%
otherwise
    error(['Unhandled flag = ',num2str(flag)]);

end

%
%=====
% mdlInitializeSizes
% Return the sizes, initial conditions, and sample times for the S-function.
%=====
%
function [sys,x0,str,ts]=mdlInitializeSizes(Num_Outputs)

global Beam
global Eye
global Retina
global Mirror
global Lens
global Detector
global Second_Axes_Position
global Beam_Out
global Beam_In_Eye
global Beam_Return
global myHandles

sizes = simsizes;
sizes.NumContStates = 0;
sizes.NumDiscStates = 0;
sizes.NumOutputs = Num_Outputs; % dynamically sized
sizes.NumInputs = -1; % dynamically sized
sizes.DirFeedthrough = 1; % has direct feedthrough
sizes.NumSampleTimes = 1;

sys = simsizes(sizes);
str = [];
x0 = [];

```

```

ts = [-1 0]; % inherited sample time

% Initialize optical system parameters
% Forces Edge thickness measurements to be converted to center thickness
% measurements.
CONVERT_EDGE_THICKNESS = 1;
% Call script to initialize optical system parameters
Lens_Structure
% Array initialization used to preallocate the amount of memory necessary
% to store each optical interface hit of a ray.
Num_Hits_Out = 6;
Num_Hits_In_Eye = 4;
Num_Hits_Return = 12;

Num_Beams_Out = 2;
Num_Beams_In_Eye = 2;
Num_Beams_Return = 3;

Beam_Out = zeros(Num_Beams_Out, 3, Num_Hits_Out);
Beam_In_Eye = zeros(Num_Beams_In_Eye, 3, Num_Hits_In_Eye);
Beam_Return = zeros(Num_Beams_Return, 3, Num_Hits_Return);

% If the edge thickness must be converted to center thickness of a lens,
% then do it for each lens.
if CONVERT_EDGE_THICKNESS
    for iCount = 1:length(Lens)
        Lens(iCount).Thickness = ...
            ConvertThickness(Lens(iCount).Surface_Radii, ...
                Lens(iCount).Lens_Diameter, ...
                Lens(iCount).Thickness);
    end

    Eye.Thickness = ConvertThickness(Eye.Surface_Radii, ...
        Eye.Lens_Diameter, ...
        Eye.Thickness);

end
% Draws all the optical elements and initializes the line elements
% representing the rays.
Draw_All

% end mdlInitializeSizes

%=====
% mdlOutputs

```

```

% Return the block outputs.
%=====
%
function sys=mdlOutputs(t,x,u)

global Beam
global Eye
global Retina
global Mirror
global Lens
global Detector
global Second_Axes_Position
global Beam_Out
global Beam_In_Eye
global Beam_Return
global myHandles

Lens(1).Position(2) = u(1);
Lens(4).Position(2) = u(1) + Second_Axes_Position;

Eye.Position(2) = u(2);

Primary_Out = 1;
Secondary_Out = 2;
Secondary_In = 3;
Primary_In = 4;
Focusing = 5;

Beam_Out_Count = 1;

Beam_Out(:, :, Beam_Out_Count) = Beam;

% Perform Ray Trace for each optical element leaving the device to
% intercept the eye.
for iCount = Primary_Out:Secondary_Out

    % Calculate ray trace for intercepting surface of optical element.
    Beam_Out(:, :, Beam_Out_Count + 1) = Lens_Surface(...
        Lens(iCount).Position, ...
        Lens(iCount).Lens_Diameter, ...
        0, ...
        Lens(iCount).Surface_Radii(1),...
        1/Lens(iCount).Refractive_Index, ...
        Lens(iCount).Normal, ...

```

```

    Beam_Out(:, :, Beam_Out_Count));

Beam_Out_Count = Beam_Out_Count + 1;
% Calculate ray trace for exiting surface of optical element.
Beam_Out(:, :, Beam_Out_Count + 1) = Lens_Surface( ...
    Lens(iCount).Position, ...
    Lens(iCount).Lens_Diameter, ...
    Lens(iCount).Thickness, ...
    Lens(iCount).Surface_Radii(2), ...
    Lens(iCount).Refractive_Index, ...
    Lens(iCount).Normal, ...
    Beam_Out(:, :, Beam_Out_Count));

Beam_Out_Count = Beam_Out_Count + 1;

end

% Trace rays to the x location of the eye.
Beam_Out(:, 1, Beam_Out_Count + 1) = repmat(Eye.Position(1), ...
    size(Beam_Out, 1), 1);
Beam_Out(:, 2, Beam_Out_Count + 1) = (Eye.Position(1) - ...
    Beam_Out(:, 1, Beam_Out_Count)).* ...
    tan(Beam_Out(:, 3, Beam_Out_Count)) + ...
    Beam_Out(:, 2, Beam_Out_Count);

% Determine if the eye lies within the diameter of the beam at the location
% of the eye.
if (all(Beam_Out(:, 2, end) > Eye.Position(2) + 0.5*Eye.Pupil_Diameter) || ...
    (all(Beam_Out(:, 2, end) < Eye.Position(2) - 0.5*Eye.Pupil_Diameter)))
    % Eye is not within the beam
    Eye_Hit = 0;
    Detector_Hit = 0;
    % Return a value of zeros
    sys = 0;

else
    % Eye has been hit by the beam.
    Eye_Hit = 1;

    % Calculate the maximum and minimum angles of rays intercepting the eye
    [MaxAngle indexMaxAngle] = max(Beam_Out(:, 3, Beam_Out_Count));
    [MinAngle indexMinAngle] = min(Beam_Out(:, 3, Beam_Out_Count));

    % Calculate origin of beams that enter the eye.
    Ox = (Beam_Out(indexMaxAngle, 2, end) - Beam_Out(indexMinAngle, 2, end) + ...

```



```

    Beam_Out (indexMinAngle,1,end)*tan (MinAngle) - ...
    Beam_Out (indexMaxAngle,1,end)*tan (MaxAngle))/ ...
    (tan (MinAngle)-tan (MaxAngle));

Oy = tan (MaxAngle)*(Ox - Beam_Out (indexMaxAngle,1,end)) + ...
    Beam_Out (indexMaxAngle,2,end);

Oxy = [Ox Oy];

Beam_In_Eye_Count = 1;
% Calculate where beams intersect the eye.
Beam_In_Eye(:, 1, Beam_In_Eye_Count) = [Eye.Position(1); ...
    Eye.Position(1)];
Beam_In_Eye(:, 2, Beam_In_Eye_Count) = (Eye.Position(2) + ...
    0.5*Eye.Pupil_Diameter*[1; -1]);
Beam_In_Eye(:, 3, Beam_In_Eye_Count) = atan( ...
    (Beam_In_Eye(:, 2, Beam_In_Eye_Count) ...
    - Oxy(2))/ (Eye.Position(1) - Oxy(1)));

Eye.Lens_Position = Eye.Position;
% Perform ray trace through lens of the eye.
% Intercepting surface
Beam_In_Eye(:, :, Beam_In_Eye_Count+1) = Lens_Surface(...
    Eye.Lens_Position, ...
    Eye.Lens_Diameter, ...
    0, ...
    Eye.Surface_Radii(1), ...
    1/Eye.Refractive_Index, ...
    Eye.Normal, ...
    Beam_In_Eye(:, :, Beam_In_Eye_Count));

Beam_In_Eye_Count = Beam_In_Eye_Count + 1;

% Exiting surface...beam now heads towards the retina.
Beam_In_Eye(:, :, Beam_In_Eye_Count+1) = Lens_Surface(...
    Eye.Lens_Position, ...
    Eye.Lens_Diameter, ...
    Eye.Thickness, ...
    Eye.Surface_Radii(2), ...
    Eye.Refractive_Index, ...
    Eye.Normal, ...
    Beam_In_Eye(:, :, Beam_In_Eye_Count));

```

```

Beam_In_Eye_Count = Beam_In_Eye_Count + 1;

% Calculate where beam intersects the retina
Beam_In_Eye(:, 1, Beam_In_Eye_Count+1) = [Retina.Position(1); ...
                                           Retina.Position(1)];
Beam_In_Eye(:, 2, Beam_In_Eye_Count+1) = ...
    Beam_In_Eye(:, 2, Beam_In_Eye_Count) + ...
    (Retina.Position(1) - ...
    Beam_In_Eye(:, 1, Beam_In_Eye_Count)) .* ...
    tan(Beam_In_Eye(:, 3, Beam_In_Eye_Count));

Beam_In_Eye_Count = Beam_In_Eye_Count + 1;

% Begin trace of reflection of beam from the retina of
% the eye back to the detector of the optical system.
Beam_Return_Count = 1;
Percent_Diameter = 0.5;    %Estimate the percent diameter
                           %of the pupil that will result
                           %in an interception of the return
                           %beam with the detector.

% Initialize where reflected beam starts
Beam_Return(:, 1, Beam_Return_Count) = Retina.Position(1) * [1;1;1];
Beam_Return(:, 2, Beam_Return_Count) = sort( ...
    [Beam_In_Eye(:, 2, Beam_In_Eye_Count); ...
    mean(Beam_In_Eye(:, 2, Beam_In_Eye_Count))], ...
    'ascend');

% Estimate the maximum divergence angle necessary for reflection to
% intercept the detector.
Beam_Return(:, 3, Beam_Return_Count) = ...
    [atan((Eye.Position(2) + ...
    Percent_Diameter * 0.5 * Eye.Lens_Diameter - ...
    Beam_Return(1, 2, Beam_Return_Count))./ ...
    (-Eye.Position(1) + ...
    Beam_Return(1, 1, Beam_Return_Count))); ...
    atan((Eye.Position(2) - ...
    Beam_Return(2, 2, Beam_Return_Count))./ ...
    (-Eye.Position(1) + ...
    Beam_Return(2, 1, Beam_Return_Count)));
    atan((Eye.Position(2) - ...
    Percent_Diameter * 0.5 * Eye.Lens_Diameter - ...
    Beam_Return(3, 2, Beam_Return_Count))./ ...
    (-Eye.Position(1) + ...
    Beam_Return(3, 1, Beam_Return_Count))]);

```

```

Eye.Lens_Position(1) = 2*Retina.Position(1) - ...
                    Eye.Lens_Position(1) - Eye.Thickness;

% Trace rays through inner surface of the bi-convex lens of the eye
Beam_Return(:, :, Beam_Return_Count+1) = Lens_Surface(...
    Eye.Lens_Position, ...
    Eye.Lens_Diameter, ...
    0, ...
    -Eye.Surface_Radii(2), ...
    1/Eye.Refractive_Index, ...
    Eye.Normal, ...
    Beam_Return(:, :, Beam_Return_Count));

Beam_Return_Count = Beam_Return_Count + 1;
% Trace rays through outer ocular surface, exiting towards the source
% of the probe beam.
Beam_Return(:, :, Beam_Return_Count+1) = Lens_Surface(...
    Eye.Lens_Position, ...
    Eye.Lens_Diameter, ...
    Eye.Thickness, ...
    -Eye.Surface_Radii(1), ...
    Eye.Refractive_Index, ...
    Eye.Normal, ...
    Beam_Return(:, :, Beam_Return_Count));

Beam_Return_Count = Beam_Return_Count + 1;

%Label indecies for "mirrors" used in return of optical system.
Beam_Splitter = 1;
Beam_Redirect = 2;

XPosition = 2*Retina.Position(1) - Mirror(Beam_Splitter).Position(1);

Mirror_Limits = Mirror(Beam_Splitter).Position(2) + ...
    0.5*Mirror(Beam_Splitter).Width * ...
    cos(Mirror(Beam_Splitter).Normal) * [1 -1];

% Calculate intercept of return rays with beam splitter, and new real
% world angle vector
Beam_Return(:, 1, Beam_Return_Count+1) = ...
    (Beam_Return(:, 1, Beam_Return_Count)).* ...

```

```

        tan(Beam_Return(:,3,Beam_Return_Count)) + ...
        XPosition* ...
        tan(Mirror(Beam_Splitter).Normal) + ...
        Mirror(Beam_Splitter).Position(2) - ...
        Beam_Return(:,2,Beam_Return_Count))./ ...
        (tan(Beam_Return(:,3,Beam_Return_Count)) + ...
        tan(Mirror(Beam_Splitter).Normal));

Beam_Return(:,2,Beam_Return_Count+1) = ...
    tan(Beam_Return(:,3,Beam_Return_Count)).* ...
    (Beam_Return(:,1,Beam_Return_Count+1) - ...
    Beam_Return(:,1,Beam_Return_Count)) + ...
    Beam_Return(:,2,Beam_Return_Count);

Beam_Return(:,3,Beam_Return_Count+1) = ...
    -(Beam_Return(:,3,Beam_Return_Count) + ...
    2*Mirror(Beam_Splitter).Normal);

Beam_Return_Count = Beam_Return_Count + 1;

XPosition = 2*Retina.Position(1) - Mirror(Beam_Redirect).Position(1);

%Calculate intersection and real world angle vector of rays
%encountering the redirection mirror.
Beam_Return(:,1,Beam_Return_Count+1) = ...
    (Beam_Return(:,1,Beam_Return_Count)).* ...
    tan(Beam_Return(:,3,Beam_Return_Count)) - ...
    XPosition* ...
    tan(Mirror(Beam_Redirect).Normal) + ...
    Mirror(Beam_Redirect).Position(2) - ...
    Beam_Return(:,2,Beam_Return_Count))./ ...
    (tan(Beam_Return(:,3,Beam_Return_Count)) - ...
    tan(Mirror(Beam_Redirect).Normal));

Beam_Return(:,2,Beam_Return_Count+1) = ...
    tan(Beam_Return(:,3,Beam_Return_Count)).* ...
    (Beam_Return(:,1,Beam_Return_Count+1) - ...
    Beam_Return(:,1,Beam_Return_Count)) + ...
    Beam_Return(:,2,Beam_Return_Count);

Beam_Return(:,3,Beam_Return_Count+1) = ...
    2*Mirror(Beam_Redirect).Normal - ...
    Beam_Return(:,3,Beam_Return_Count);

```

```

Beam_Return_Count = Beam_Return_Count + 1;

% Trace rays through the input optical axis. Begins with the secondary
% lens of the Alvarez lens pair, through the focusing lens which
% focuses the return onto the detector.
for iCount = Secondary_In:Focusing

    XPosition = 2*Retina.Position(1) - Lens(iCount).Position(1) ...
                - Lens(iCount).Thickness;
    % Trace rays through intercept surface of the lens
    Beam_Return(:, :, Beam_Return_Count + 1) = Lens_Surface(...
        [XPosition Lens(iCount).Position(2:3)], ...
        Lens(iCount).Lens_Diameter, ...
        0, ...
        -Lens(iCount).Surface_Radii(2), ...
        1/Lens(iCount).Refractive_Index, ...
        Lens(iCount).Normal, ...
        Beam_Return(:, :, Beam_Return_Count));

    Beam_Return_Count = Beam_Return_Count + 1;

    % Trace rays through exit surface of the lens
    Beam_Return(:, :, Beam_Return_Count + 1) = Lens_Surface( ...
        [XPosition Lens(iCount).Position(2:3)], ...
        Lens(iCount).Lens_Diameter, ...
        Lens(iCount).Thickness, ...
        -Lens(iCount).Surface_Radii(1), ...
        Lens(iCount).Refractive_Index, ...
        Lens(iCount).Normal, ...
        Beam_Return(:, :, Beam_Return_Count));

    Beam_Return_Count = Beam_Return_Count + 1;

end

XPosition = 2*Retina.Position(1) - Detector.Position(1);

% Calculate ray positions at the distance (x value) of the detector
% from the focusing lens
Beam_Return(:, 1, Beam_Return_Count+1) = XPosition;
Beam_Return(:, 2, Beam_Return_Count+1) = ...
    tan(Beam_Return(:, 3, Beam_Return_Count)).* ...
    (XPosition - ...

```

```

        Beam_Return(:,1,Beam_Return_Count)) + ...
        Beam_Return(:,2,Beam_Return_Count);

Beam_Return_Count = Beam_Return_Count + 1;
% Calculate the limits of the active surface area of the detector in
% real world coordinates.
Detector_Max_Edge = Detector.Position(2) + ...
    0.5*Detector.Sensor_Diameter;
Detector_Min_Edge = Detector.Position(2) - ...
    0.5*Detector.Sensor_Diameter;
% Determine if any of the beam intercepts the detector.
if all(Beam_Return(:,2,end)>Detector_Max_Edge) | ...
    all(Beam_Return(:,2,end)<Detector_Min_Edge)
    %Beam does not intercept the detector
    Detector_Hit = 0;
    Detector_Return_Position = 0;

else
    %Return beam does intercept the detector
    Detector_Hit = 1;
    % Find the limits of the return beam in the y direction
    yMax = max(Beam_Return(:,2,end));
    yMin = min(Beam_Return(:,2,end));

    % If the beam exceeds the detector limits, then set the max
    % position (or min position) to the detector limit.
    if yMax>Detector_Max_Edge
        yMax = Detector_Max_Edge;
    end

    if yMin<Detector_Min_Edge
        yMin = Detector_Min_Edge;
    end

    % Calculate the average position of the beam on the detector.
    Detector_Return_Position = mean([yMax yMin]) - ...
        Detector.Position(2);
end

% Update the data of the graphical representations of the ray traces to
% correspond to the most current information.
for iCount = 1:length(myHandles.Beam_Return)
    set(myHandles.Beam_Return(iCount), 'XData', ...
        2*Retina.Position(1) - squeeze(Beam_Return(iCount,1,1:12))');
end

```

```

        set(myHandles.Beam_Return(iCount), 'YData', ...
            squeeze(Beam_Return(iCount,2,1:12))');
    end

    set(myHandles.Beam_Return, 'Visible', 'on')

    set(myHandles.Beam_On_Detector, 'Ydata', Detector_Return_Position);

    sys = Detector_Return_Position;
end

% Update graphical representation of primary lens with new position.
set(Lens(Primary_Out).Handle, 'ydata', myHandles.PrimaryGraphicData.Y + ...
    Lens(Primary_Out).Position(2));
set(Lens(Primary_In).Handle, 'ydata', myHandles.PrimaryGraphicData.Y + ...
    Lens(Primary_In).Position(2));

% Update graphical representation of system output beam
for iCount = 1:length(myHandles.Beam_Out)
    set(myHandles.Beam_Out(iCount), 'XData', ...
        squeeze(Beam_Out(iCount,1,:))');
    set(myHandles.Beam_Out(iCount), 'YData', ...
        squeeze(Beam_Out(iCount,2,:))');
end
% Flush the event queue, including all graphical events that need to be
% updated.
drawnow
% end mdlOutputs

```

APPENDIX B
C CODE FOR DSP

B.1 DSP Code

```
/*
 * File: two_channel_8000Hz_00.c
 *
 * Real-Time Workshop code generated for Simulink model two_channel_8000Hz_00.
 *
 * Model version                : 1.284
 * Real-Time Workshop file version : 6.3 (R14SP3) 26-Jul-2005
 * Real-Time Workshop file generated on : Sat Jul 01 22:06:47 2006
 * TLC version                  : 6.3 (Aug 5 2005)
 * C source code generated on    : Sat Jul 01 22:07:03 2006
 */

#include "two_channel_8000Hz_00.h"
#include "two_channel_8000Hz_00_private.h"

/* *****

Global Variables

***** */

int32_T Channel_Ratio_Output[4096];
int16_T Angular_Position_Output[4096];

int32_T lNormalizedPositionOutput[1024];
int32_T lDerivativeComponentOutput[1024];

// Buffers for boxcar filters
int32_T Boxcar32TapBuffer_Channel1_Real[32];
int32_T Boxcar32TapBuffer_Channel1_Imag[32];

int32_T Boxcar32TapBuffer_Channel2_Real[32];
int32_T Boxcar32TapBuffer_Channel2_Imag[32];

int32_T Boxcar64TapBuffer_NormalizePosition[128];

// Buffers for boxcar filter unit delays
int32_T lFiltered_Real_Channel1 = 0;
```



```

int32_T lFiltered_Imag_Channel1 = 0;

int32_T lFiltered_Real_Channel2 = 0;
int32_T lFiltered_Imag_Channel2 = 0;

int32_T lFiltered_NormalizedPosition = 0;

// Buffer for unit delay in derivative calculation
int32_T lLast_NormalizedPosition = 0;

int16_T iFiltered_AngularPosition = 0;

// Counter for input from cosine and sine lookup tables
int16_T CosineSineLUT_Counter = 0;
// Counters for indexes in boxcar filter buffers
int16_T iBoxcar32TapCounter = 0;
int16_T iBoxcar64TapCounter = 0;

int16_T myIndexCounter = 0;
int16_T myIterationCounter = 0;

/* Block signals (auto storage) */
BlockIO_two_channel_8000Hz_00 two_channel_8000Hz_00_B;

/* Block states (auto storage) */
D_Work_two_channel_8000Hz_00 two_channel_8000Hz_00_DWork;

/* Real-time model */
RT_MODEL_two_channel_8000Hz_00 two_channel_8000Hz_00_M;
RT_MODEL_two_channel_8000Hz_00 *two_channel_8000Hz_00_M =
    &two_channel_8000Hz_00_M;

/* Model step function */
void two_channel_8000Hz_00_step(void)
{
    /* *****
        Local Variables
        ***** */

    int16_T iSystemInput_Channel1; //ADC input for channel 1

```

```

int16_T iSystemInput_Channel2; //ADC input for channel 2
int16_T iSystemInput_Channel3; //ADC input for channel 3
int16_T iChannelDifference; //difference in
                                //amplitude b/w channels

int16_T iInverseLUTindex; //Index into inverse
                                //lookup table (LUT)
int16_T iInverseLookup; //Inverse value from LUT
int16_T iShifterLookup; //Bit shift required for inverse
                                //calc from LUT

int32_T lFilterEndElement; //Stores element in
                                //a boxcar filter buffer
                                //that is oldest value
                                //in the buffer

int32_T lSystemInputShifted_Channel1; //stores ADC input
int32_T lSystemInputShifted_Channel2; //after conversion
    //to 32 bit values

int32_T lCosine1000Hz; //Input value from Cosine LUT
int32_T lSine1000Hz; //Input value from Sine LUT

int32_T lMixed_Real; //Result of mixing input
                                //signal with Cosine
int32_T lMixed_Imag; //Result of mixing input
                                //signal with Sine

int32_T lSquared_Real; //Result of squaring mixed real component
int32_T lSquared_Imag; //Result of squaring mixed imaginary comp.

int32_T lMagnitude_Squared_Channel1; //Magnitude of signal in channel 1
int32_T lMagnitude_Squared_Channel2; //Magnitude of signal in channel 2

int32_T lChannelSum; //Sum of channel squared magnitudes

int32_T lNormalized_Position; //Position on detector normalized
                                //by total input magnitude
int32_T lDerivative_Component; //Store difference of current timestep
                                //detector position with that of the
                                //previous time step.

int32_T lAdjusted_Filtered_NormalizedPosition;

int32_T lMySystemOutput; //Store value to be exported to the

```

//Pulse Width Modulator (PWM)

```
/* *****  
  
                System Input  
  
***** */  
  
/* -----Analog to Digital Converter Input-----*/  
{  
    AdcRegs.ADCTRL2.bit.RST_SEQ1 = 0x1; // Sequencer reset  
    AdcRegs.ADCTRL2.bit.SOC_SEQ1 = 0x1; // Software start of conversion  
    asm("    nop" );  
    asm("    nop" );  
    asm("    nop" );  
    asm("    nop" );  
    while (AdcRegs.ADCST.bit.SEQ1_BSY==0x1) {} //Wait for Sequencer  
                                                //Busy bit to clear  
  
    //Shift system input values from 16 bit values to 12 bit vals  
    iSystemInput_Channel1 = (AdcRegs.ADCRESULT0) >> 4;  
    iSystemInput_Channel2 = (AdcRegs.ADCRESULT1) >> 4;  
    iSystemInput_Channel3 = (AdcRegs.ADCRESULT2) >> 4;  
}  
  
/* Convert to 32 bit format with 30 Fractional bits */  
lSystemInputShifted_Channel1 = (int32_T)iSystemInput_Channel1 << 18U;  
lSystemInputShifted_Channel2 = (int32_T)iSystemInput_Channel2 << 18U;  
  
///Shifted_System_Input_Channel1[myCounter] = lSystemInputShifted_Channel1;  
///Shifted_System_Input_Channel2[myCounter] = lSystemInputShifted_Channel2;  
  
/* Cosine Lookup Table*/  
lCosine1000Hz =  
    two_channel_8000Hz_00_P.Cosine_Values_SineTable[CosineSineLUT_Counter];  
//Cosine_LUT_Input[myCounter] = lCosine1000Hz;  
  
/* Sine Lookup Table */  
lSine1000Hz =  
    two_channel_8000Hz_00_P.Sine_Values_SineTable[CosineSineLUT_Counter];  
  
/* Cosine and Sine LUT counter - increment and wrap */
```

```

CosineSineLUT_Counter++;
CosineSineLUT_Counter = CosineSineLUT_Counter & 7;

/* Since the cosine and sine LUTs have a power of 2 number of
 *elements, they can be wrapped using bitand with n-1 where n
 *is the number of elements in the LUT. */

/* *****

CHANNEL 1

***** */

/* -----Real Component-----*/
/* MIXING Real Signal Component Channel 1*/
lMixed_Real = _IQ30mpy (lSystemInputShifted_Channel1, lCosine1000Hz);
//Mixer_Real_Output[myCounter] = lMixed_Real;

/* Boxcar Filter for Real Component in Channel 1*/
lFilterEndElement = Boxcar32TapBuffer_Channel1_Real[iBoxcar32TapCounter];

/*Filter Channel 1 Real with Rounding*/
lFiltered_Real_Channel1 += ((lMixed_Real - lFilterEndElement) >>5) +
  (((lMixed_Real - lFilterEndElement) & 16L) != (int32_T)0);

/* Rounding is necessary to prevent cumulative bit truncation leading
 *to a drift in the result of the filter. */

/* Squaring Real Component Channel 1*/
lSquared_Real = _IQ30mpy (lFiltered_Real_Channel1,
lFiltered_Real_Channel1);

/* -----Imaginary Component-----*/
/* Mixing Imaginary Signal Component Channel 1*/
lMixed_Imag = _IQ30mpy (lSystemInputShifted_Channel1, lSine1000Hz);

/* Boxcar Filter for Imaginary Component in Channel 1 */
lFilterEndElement = Boxcar32TapBuffer_Channel1_Imag[iBoxcar32TapCounter];

lFiltered_Imag_Channel1 += ((lMixed_Imag - lFilterEndElement) >> 5) +
  (((lMixed_Imag - lFilterEndElement) & 16L) != (int32_T)0);

/* Squaring Imaginary Component Channel 1 */

```

```

lSquared_Imag = _IQ30mpy (lFiltered_Imag_Channel1,
lFiltered_Imag_Channel1);

/* -----Magnitude of Components-----*/
/* Output is MAGNITUDE SQUARED for Channel 1 */
lMagnitude_Squared_Channel1 = (int32_T)((lSquared_Real + lSquared_Imag));

/* -----Update Filters and Delays-----*/
/* Incrementing Real Filter Channel 1 */
Boxcar32TapBuffer_Channel1_Real[iBoxcar32TapCounter] = lMixed_Real;

/* Incrementing Imaginary Filter Channel 1 */
Boxcar32TapBuffer_Channel1_Imag[iBoxcar32TapCounter] = lMixed_Imag;

/* *****

CHANNEL 2

***** */

/* -----Real Component-----*/
/* MIXING Real Signal Component Channel 2*/
lMixed_Real = _IQ30mpy (lSystemInputShifted_Channel2, lCosine1000Hz);

/* Boxcar Filter for Real Component in Channel 2*/
lFilterEndElement = Boxcar32TapBuffer_Channel2_Real[iBoxcar32TapCounter];

/*Filter Channel 2 Real with Rounding*/
lFiltered_Real_Channel2 += ((lMixed_Real - lFilterEndElement) >> 5) +
((lMixed_Real - lFilterEndElement) & 16L) != (int32_T)0);

/* Squaring Real Component Channel 2*/
lSquared_Real = _IQ30mpy (lFiltered_Real_Channel2,
lFiltered_Real_Channel2);

/* -----Imaginary Component-----*/
/* Mixing Imaginary Signal Component Channel 2*/
lMixed_Imag = _IQ30mpy (lSystemInputShifted_Channel2, lSine1000Hz);
//Mixer_Imag_Output[myCounter] = lMixed_Imag;

/* Boxcar Filter for Imaginary Component in Channel 2 */

```

```

lFilterEndElement = Boxcar32TapBuffer_Channel2_Imag[iBoxcar32TapCounter];

lFiltered_Imag_Channel2 += ((lMixed_Imag - lFilterEndElement) >> 5) +
  (((lMixed_Imag - lFilterEndElement) & 16L) != (int32_T)0);

/* Squaring Imaginary Component Channel 2 */
lSquared_Imag = _IQ30mpy (lFiltered_Imag_Channel2,
lFiltered_Imag_Channel2);

/* -----Magnitude of Components-----*/
/* Output is MAGNITUDE SQUARED for Channel 2 */
lMagnitude_Squared_Channel2 = (int32_T)((lSquared_Real + lSquared_Imag));

/* -----Update Filters and Delays-----*/
/* Incrementing Real Filter Channel 2 */
Boxcar32TapBuffer_Channel2_Real[iBoxcar32TapCounter] = lMixed_Real;

/* Incrementing Imaginary Filter Channel 2 */
Boxcar32TapBuffer_Channel2_Imag[iBoxcar32TapCounter] = lMixed_Imag;

/* *****

Signal Math

***** */
/* -----Difference b/w Channel Mags-----*/
iChannelDifference = (uint16_T)((lMagnitude_Squared_Channel1
- lMagnitude_Squared_Channel2) >> 12);

/* Actual bit shift right is 15, but need to left 3 bits for the inverse
*LUT results, so this is combined in one bit shift right of 12 */

/* -----Sum of Channel Mags-----*/
lChannelSum = lMagnitude_Squared_Channel1 + lMagnitude_Squared_Channel2;

/* Convert channel SUM to 12 bit number for inverse LUT index.
- includes rounding to nearest index value */
iInverseLUTindex = (uint16_T)((int32_T)((lChannelSum & 131072L) !=
(int32_T)0) + (lChannelSum >> 18));

```

```

/* -----Inverse Lookup Tables-----*/
//ensure the index value does not exceed max index of LUT
iInverseLUTindex = rt_MIN(iInverseLUTindex, 4095);
// Perform Lookup
iInverseLookup =
two_channel_8000Hz_00_P.InverseLookup_table[iInverseLUTindex];
iShifterLookup =
two_channel_8000Hz_00_P.ShifterLookup_table[iInverseLUTindex];

/* -----Calculate Normalized Position-----*/
lNormalized_Position = ((int32_T)iChannelDifference *
(int32_T)iInverseLookup) >> iShifterLookup;

/* -----Filter Normalized Position-----*/
lFilterEndElement =
Boxcar64TapBuffer_NormalizePosition[iBoxcar64TapCounter];

/*Filter with Rounding*/
lFiltered_NormalizedPosition +=
((lNormalized_Position - lFilterEndElement) >> 7) +
(((lNormalized_Position - lFilterEndElement) & 64L) != (int32_T)0);

/* Recording at a lower sample rate. Only recording when
myIterationCounter is 0*/

if(myIterationCounter==0){

//Storing position in circular buffer
Angular_Position_Output[myIndexCounter] = iSystemInput_Channel3;

//Updating circular buffer index
myIndexCounter++;
myIndexCounter = myIndexCounter & 4095;

}

/* -----Update Filters and Delays-----*/
/* Incrementing Normalized Position Filter */
Boxcar64TapBuffer_NormalizePosition[iBoxcar64TapCounter] =
lNormalized_Position;

/* *****

```

Controller

```

***** */

/* Calculating estimated time derivative of output position signal */
lDerivative_Component = lLast_NormalizedPosition -
lFiltered_NormalizedPosition;

/* Adjusting position signal for inherent bias. */
lAdjusted_Filtered_NormalizedPosition = lFiltered_NormalizedPosition + 18000;

/* Only apply filter if the position is a certain distance from 0 */
if ((lAdjusted_Filtered_NormalizedPosition > 8000) |
(lAdjusted_Filtered_NormalizedPosition < -8000)){

/* Calculate controller output */
lMySystemOutput = (6250 + (lAdjusted_Filtered_NormalizedPosition >> 5) +
(lDerivative_Component));

/* Making sure that the output does not exceed the limits of the PWM */
if(lMySystemOutput < 0){
  lMySystemOutput = 10;
}

if(lMySystemOutput > 12500){
  lMySystemOutput = 12490;
}

}else{
  /* If the position is close to 0, then apply 0 (bias) output */
  lMySystemOutput = 6250;
}

/* Store current position for derivative for the next time step */
lLast_NormalizedPosition = lFiltered_NormalizedPosition;

/* *****

System Output

***** */
/* Pulse Width Modulator (PWM) */
/* S-Function Block: <Root>/C28x PWM (c28xpwm) */
{

```



```

    EvaRegs.CMPR2 = (uint16_T)lMySystemOutput;
}

/* Increment and wrap filter buffer counters */
iBoxcar32TapCounter++;
iBoxcar32TapCounter = iBoxcar32TapCounter & 31;

iBoxcar64TapCounter++;
iBoxcar64TapCounter = iBoxcar64TapCounter & 127;

/* Since the filter buffers have a power of 2 number of
 *elements, bitand n-1 with the current counter value will
 *wrap the counter in a buffer with n elements */

/* Recording beam angular position every 16 samples */
myIterationCounter++;
myIterationCounter = myIterationCounter & 15;
}

/* *****

                                Model Initialization

***** */

void two_channel_8000Hz_00_initialize(boolean_T firstTime)
{
    int32_T lBufferInitialValue = 0;

    if (firstTime) {
        /* initialize error status */
        rtmSetErrorStatus(two_channel_8000Hz_00_M, (const char_T *)0);

        /* block I/O */
        (void) memset(((void *)
            &two_channel_8000Hz_00_B), 0, sizeof(BlockIO_two_channel_8000Hz_00));

        /* data type work */
        (void) memset((char_T *)
            &two_channel_8000Hz_00_DWork, 0, sizeof(D_Work_two_channel_8000Hz_00));
    }
}

```

```

/* initialize non-finites */
rt_InitInfAndNaN(sizeof(real_T));

InitAdc();

config_ADC_A (2U, 528U, 0U, 0U, 0U);

/* Signal Processing Blockset Sine Wave (sdspine2) - '<Root>/Cosine' - Start */
/* Full-cycle table lookup, restart at time zero */
//two_channel_8000Hz_00_DWork.Cosine_TableIdx = 0;

/* Signal Processing Blockset Sine Wave (sdspine2) - '<Root>/Sine' - Start */
/* Full-cycle table lookup, restart at time zero */
//two_channel_8000Hz_00_DWork.Sine_TableIdx = 0;

EALLOW;

GpioMuxRegs.GPAMUX.all = 0x00FF;    // EVA PWM 1-6 pins
config_PWM_A (12500.0,2,1,"INPUT_PORT",18500.0,
  0,"INPUT_PORT",18500.0,0,"INPUT_PORT",18500.0,1638,
  1, 0, 0, 4, 12, 0);
EDIS;
}

/* Initial Condition for 32 Tap Filter Buffer Channel 1 Real */
{
  int_T il;

  int32_T *dw_X = &Boxcar32TapBuffer_Channell_Real[0];

  for (il=0; il < 32; il++) {
    dw_X[il] = lBufferInitialValue;
  }
}

/* Initial Condition for 32 Tap Filter Buffer Channel 1 Imag */
{
  int_T il;

  int32_T *dw_X = &Boxcar32TapBuffer_Channell_Imag[0];

  for (il=0; il < 32; il++) {
    dw_X[il] = lBufferInitialValue;
  }
}

```

```

    }
}

/* Initial Condition for 32 Tap Filter Buffer Channel 2 Real */
{
    int_T il;

    int32_T *dw_X = &Boxcar32TapBuffer_Channel2_Real[0];

    for (il=0; il < 32; il++) {
        dw_X[il] = lBufferInitialValue;
    }
}

/* Initial Condition for 32 Tap Filter Buffer Channel 2 Imag */
{
    int_T il;

    int32_T *dw_X = &Boxcar32TapBuffer_Channel2_Imag[0];

    for (il=0; il < 32; il++) {
        dw_X[il] = lBufferInitialValue;
    }
}

/* Initial Condition for 64 Tap Filter Buffer Normalized Position */
{
    int_T il;

    int32_T *dw_X = &Boxcar64TapBuffer_NormalizePosition[0];

    for (il=0; il < 64; il++) {
        dw_X[il] = lBufferInitialValue;
    }
}

{
    int_T il;

    int16_T *dw_X = &Boxcar64TapBuffer_AngularPosition[0];
}

```

```

    for (i1=0; i1 < 64; i1++) {
        dw_X[i1] = (int16_T)lBufferInitialValue;
    }
}
}

```

B.2 Lookup Table Formulation and Results

%INVERSE_12BIT_LUT - builds a 12 bit lookup table that outputs 16 bit values. The consists of two arrays, one that maximizes the amount of sensitivity for a particular value inverse, and a bit shift amount to adjust the value to the proper magnitude.

```

% Initialize array sizes with room for 16 bit
% input values with values of 0. For signed 16 bit integers the max
% value is 2^15 = 32768
LUT_shifter = zeros(1,32768);
LUT_inverse = zeros(1,32768);

% Loop through all the elements of the arrays
for I = 1:32767

    Idiv = I - mod(I,8) + 7/2;

    % Determine if the current value of "Idiv" is a power of 2
    if floor(log2(Idiv))==log2(Idiv)
        % If so, adjust the shifter result by subtracting 1
        LUT_shifter(I) = log2(Idiv) - 1;
    else
        % Otherwise round towards minus infinity
        LUT_shifter(I) = floor(log2(Idiv));
    end
    % Calculate the inverse value at the given index
    LUT_inverse(I) = round(32768*2^LUT_shifter(I)/Idiv );

end

% Convert the 16 bit LUT to a 12 bit LUT by downsampling and changing data
% type to INT16
LUT_inv_12bit      = int16(downsample(LUT_inverse, 8));
LUT_shifter_12bit  = int16(downsample(LUT_shifter, 8));

```

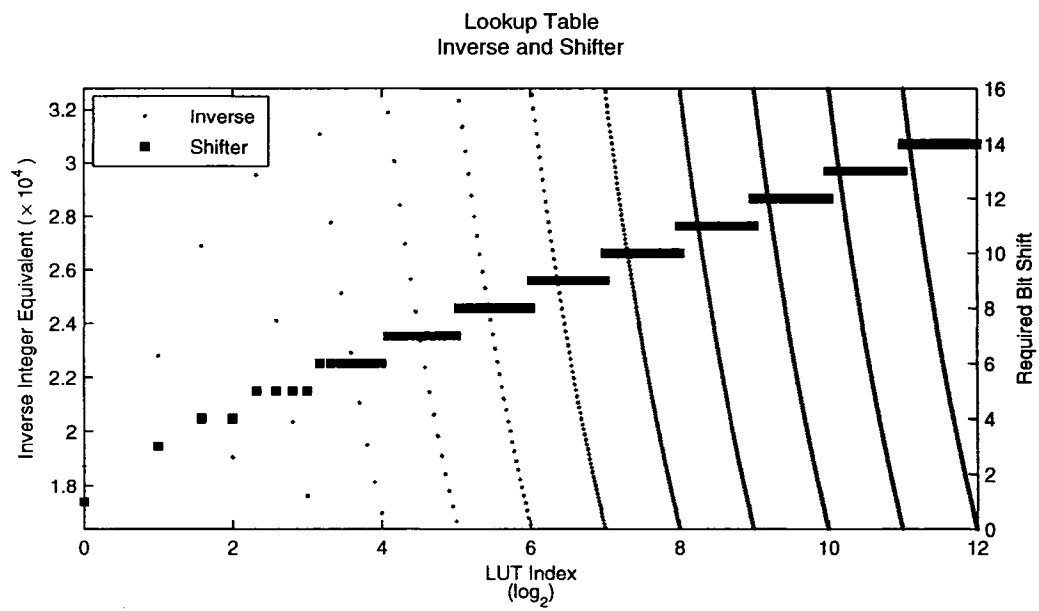


Figure B.1: Inverse Lookup Table Plot - Displays the integer value and necessary bit shift for each index of the lookup table. To perform a division, a 16 bit number is multiplied by the integer inverse value, and then a right shift of the associated number of bits as described by the bit shift table is performed on the product.

APPENDIX C
ANALOG CIRCUITRY

C.1 Signal Conditioning Schematic

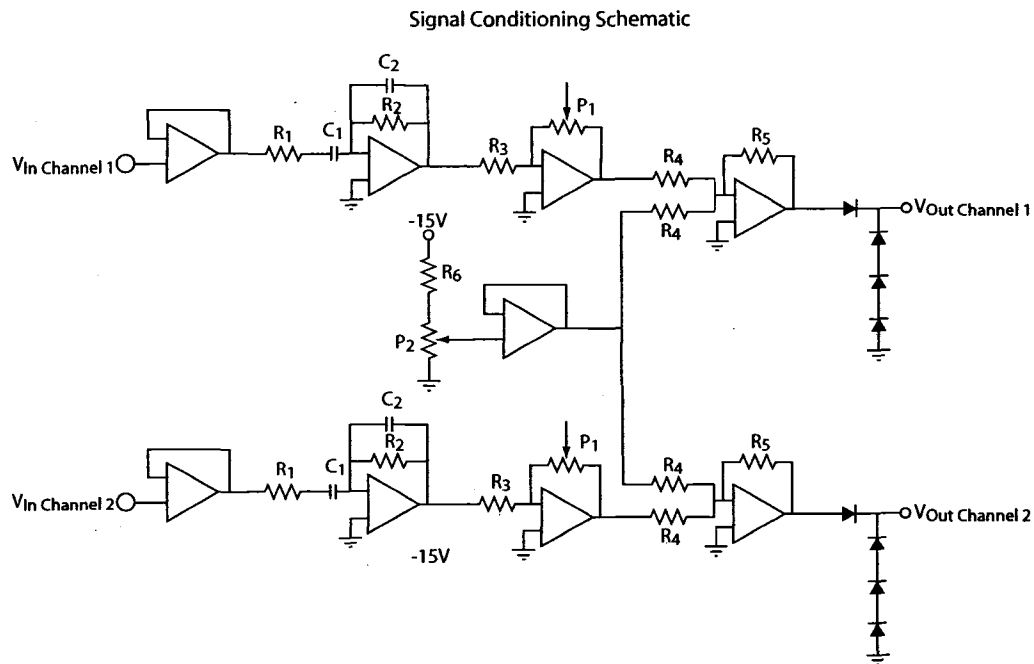


Figure C.1: Signal Conditioning Circuit Schematic

C.2 H-Bridge Schematic

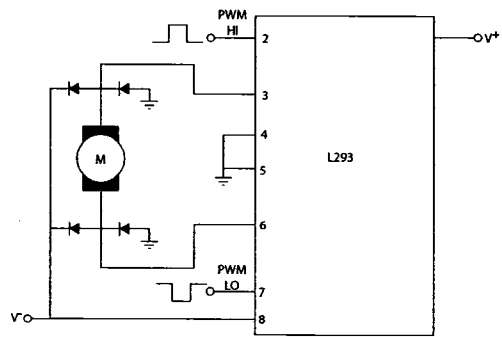


Figure C.2: H-Bridge Schematic

C.3 Eye Tracking Validation Experiment Schematic

Tracking Experiment Signal Conditioning Schematic

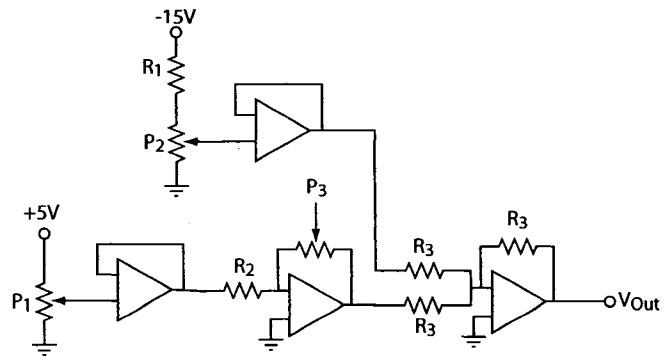


Figure C.3: Eye Tracking Validation Circuit Schematic

APPENDIX D

ANALOG SIGNAL PROCESSING

D.1 Analog Signal Processing Schematic

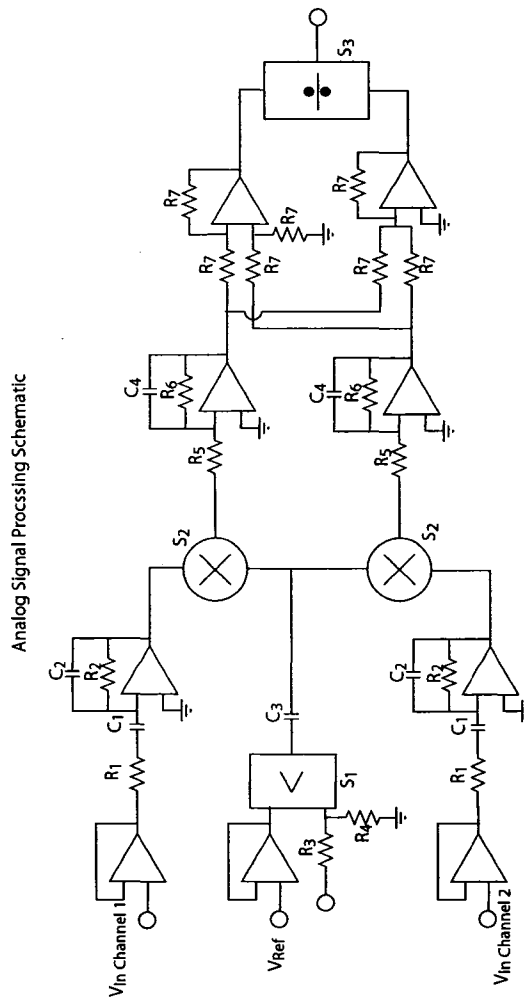


Figure D.1: Analog Signal Processing Circuit Schematic